ECAP-2017-001

Characterizing a Wavelength Shifter Coated Silicon Photomultiplier at Cryogenic Temperatures using Scintillation Light in Gaseous Xenon

Master's Thesis

for the attainment of the academic degree
Master of Science (M. Sc.)

submitted by

Patrick Hufschmidt

January 9, 2017

performed at
Erlangen Centre for Astroparticle Physics
Friedrich-Alexander-Universität Erlangen-Nürnberg
under the supervision of PD Dr. T. Michel and Prof. Dr. G. Anton

ERLANGEN CENTRE FOR ASTROPARTICLE PHYSICS

FRIEDRICH-ALEXANDER UNIVERSITÄT ERLANGEN-NÜRNBERG
NATURWISSENSCHAFTLICHE FAKULTÄT

Contents

1 Introduction

Antoine Henry Becquerel marked a new era of physics in 1896 when he discovered the radioactivity. Together with *Marie Curie* and *Pierre Curie* he was awarded with the nobel prize for this achievement [1]. This groundbreaking leap towards modern particle physics was followed by a variety of discoveries in this newly established field of science. Besides new interaction mechanisms and models that describe the new found subatomic world, new kinds of particles became the focus of research. One of these fundamental cornerstones is the *neutrino*. It was first mentioned by *Wolfgang Pauli* in December 1930, who referred to it as "neutron". The term neutrino was later introduced by *Enrico Fermi*. Pauli proposed the neutrino as spin 1/2-particle that takes part in the β-decay, thus explaining the continuous energy spectrum of the electron [2]. However, it was not until 1956 when *Clyde L. Cowan* and *Frederick Reines* first verified the existence of the neutrino using nuclear reactions [3]. Since this discovery, great progress in researching the neutrino's properties was made. Successful experimental approaches to investigate the neutrino flavors or properties concerning the neutrino mass were done. The latter one recently drew a lot of attention, when *Takaaki Kajita* and *Arthur B. McDonald* were awarded with the nobel prize in 2015 *"for the discovery of neutrino oscillations, which shows that neutrinos have mass"* [4]. Although neutrino physics has made major progress since Pauli's neutrino hypothesis, many questions remain unanswered. The unknown order of the neutrino masses (neutrino mass hierarchy), for instance, is currently under investigation in a variety of experiments like ICECUBE and Super-Kamiokande. Another unknown property of the neutrino is its Majorana nature, meaning that it is not known whether the neutrino is its own anti-particle or not.

To investigate the Majorana nature of the neutrino, physicists search for the neutrinoless double beta decay, whose existence would proof the neutrino to be its own anti-particle. The future nEXO experiment is a ton-scale low-background experiment built to search for this rare particle decay using ^{136}Xe. It is designed to increase the energy resolution drastically compared to current experiments. An important part of nEXO, as well as of many other double beta experiments, is the detection of light. As a new approach and in contrast to previous experiments, nEXO will make use of Silicon Photomultipliers (SiPM) for light detection.

SiPMs are semiconductor based light detectors. They can be produced with a very high radio purity, which is essential for nEXO since the expected event rate is extremely low. These detectors are usually not capable of detecting VUV-light. One possibility to overcome this issue is to apply a wavelength shifting material to the detector surface, enabling the SiPM to be sensitive to vacuum ultra violate (VUV) light. To realize the aim for the improved energy resolution of the nEXO experiment, the utilized SiPMs need to fulfill certain requirements. Several collaborators in the nEXO-collaboration currently investigate different SiPMs to examine proper candidates. To contribute to the search for a suitable device, the EXO-200/nEXO - work group Erlangen collaborates with the company KETEK to develop a SiPM that satisfies the requirements of the nEXO experiment.

In this thesis, the theoretical background and physical motivation for the neutrinoless double beta decay is outlined. The operation principle of a SiPM and a wavelength shifter is explained. A cryogenic test setup was built to examine a wavelength shifter coated SiPM from KETEK. This setup was investigated with respect to the temperatures the nEXO experiment is cooled down to. The characterization measurements of the SiPM are the central object of this thesis. It is examined with respect to the required limits. The results are discussed and compared to other devices investigated by other collaborators.

2 Theoretical Background and Physical Motivation

This chapter provides an overview of the theoretical concepts forming the basis of neutrino accompanied double beta decay ($\beta\beta$-decay) and neutrinoless double beta decay ($0\nu\beta\beta$-decay). Consequences on current physics in case of the existence of the $0\nu\beta\beta$-decay are discussed and the basic ansatz for an experimental approach is introduced.

2.1 Neutrino Mass Hierarchy

Neutrinos are massive, weakly interacting and electrically neutral leptons that occur in 3 different flavors: $\nu_{(\mathrm{e})}, \nu_{(\mu)}, \nu_{(\tau)}$. The observation of neutrino oscillations lead to the assumption that the neutrino flavor eigenstates $|\nu_e\rangle, |\nu_\mu\rangle, |\nu_\tau\rangle$ are not equal to their neutrino mass eigenstates $|\nu_1\rangle, |\nu_2\rangle, |\nu_3\rangle$. The flavor eigenstates are a linear combination of the mass eigenstates. They can be expressed in terms of a mixing matrix [5]:

$$|\nu_\alpha\rangle = \sum_{i=1}^{3} U_{\alpha i} |\nu_i\rangle \quad , \tag{2.1}$$

where U_{mn} is the so called *PMNS*-mixing matrix of the form [6]:

$$U_{mn} = \begin{pmatrix} c_{12}c_{13} & s_{12}c_{13} & s_{13}e^{-i\delta} \\ -s_{12}c_{23} - c_{12}s_{23}s_{13}e^{i\delta} & c_{12}c_{23} - s_{12}s_{23}s_{13}e^{i\delta} & s_{23}c_{13} \\ s_{12}s_{23} - c_{12}c_{23}s_{13}e^{i\delta} & -c_{12}s_{23} - s_{12}c_{23}s_{13}e^{i\delta} & c_{23}c_{13} \end{pmatrix} \tag{2.2}$$

with $c_{ij} = \cos(\Theta_{ij})$ and $s_{ij} = \sin(\Theta_{ij})$, where Θ_{ij} is a so called mixing angle. Θ_{ij} scales the contribution of the individual mass eigenstates to the flavor eigenstates. δ is a charge parity violating phase of which the value is not yet known [6]. This expression leaves the neutrinos with the possibility of changing their flavors with a certain probability $P(\nu_\alpha \to \nu_\beta; E, L)$, where E is the neutrino energy and L the covered propagation length since the last interaction [6]. This mechanism explains the lack of solar electron neutrinos observed by the first neutrino telescopes [7].

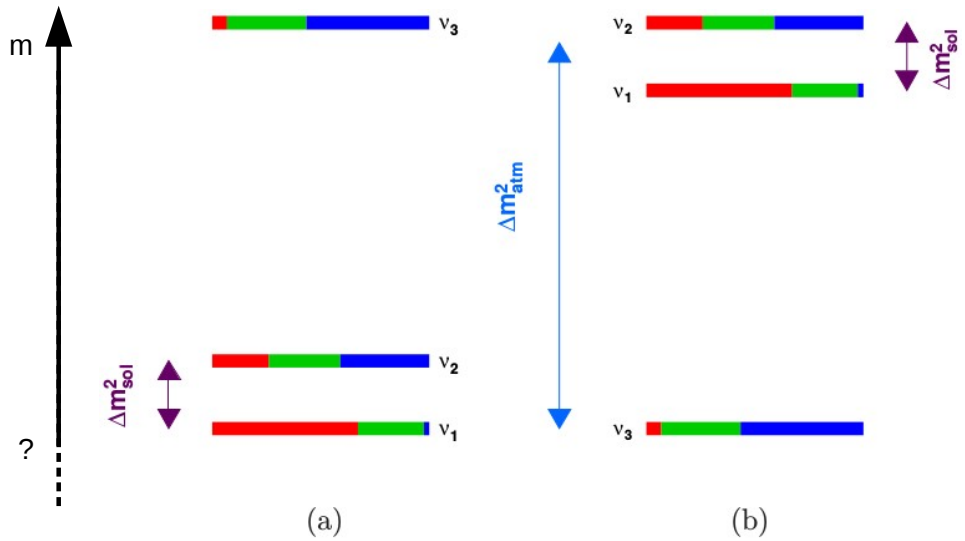

Figure 2.1: Possible arrangements of the neutrino masses. (a) Normal hierarchy, (b) inverted hierarchy. The colored areas show the contributions of the individual flavor eigenstates. This image was taken from [9].

By inverting the PMNS-mixing matrix one can express the mass eigenstates as a sum of flavor eigenstates:

$$|\nu_i\rangle = \sum_{i=1}^{3} \mathrm{U}_{\alpha i}^{*} \, |\nu_\alpha\rangle \quad . \tag{2.3}$$

From oscillations of solar neutrinos, the difference $\Delta m^2_{\mathrm{sol}} = m_2^2 - m_1^2$ of the neutrino masses of the eigenstates $|\nu_2\rangle$ and $|\nu_1\rangle$ is known to be $\Delta m^2_{\mathrm{sol}} = (7.54\,^{+0.26}_{-0.22}) \cdot 10^{-5}\,\mathrm{eV}^2$. From oscillations of atmospheric neutrinos, the absolute difference $|\Delta m^2_{\mathrm{atm}}| = |m_2^2 - m_3^2|$ of the neutrino masses of the eigenstates $|\nu_2\rangle$ and $|\nu_3\rangle$ is known to be $|\Delta m^2_{\mathrm{atm}}| = (2.45 \pm 0.06) \cdot 10^{-3}\,\mathrm{eV}^2$ for $m_3 > m_2$ and $|\Delta m^2_{\mathrm{atm}}| = (2.38 \pm 0.06) \cdot 10^{-3}\,\mathrm{eV}^2$ for $m_2 > m_3$ [6]. The unknown sign of $|\Delta m^2_{\mathrm{atm}}|$ leaves two possibilities of arranging the masses. The order $m_1 < m_2 < m_3$ is called *normal hierarchy* and the order $m_3 < m_1 < m_2$ is called *inverted hierarchy*. Fig. 2.1 shows these arrangements schematically. The colors denote the contribution of the individual flavor eigenstates. The different hierarchies make a difference in the total sum of all neutrino masses. From other neutrino experiments values or constraints on different linear combinations of neutrino masses are known [8]. Therefore, limits in which the different hierarchies possibly occur can be obtained (see sec. 2.4).

2.2 Double Beta Decay

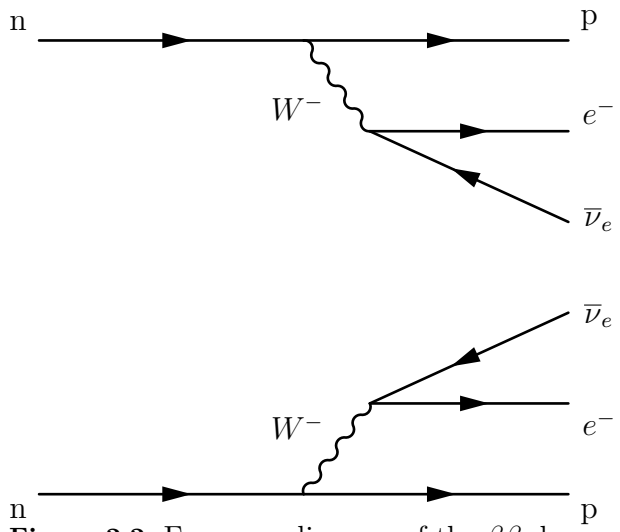

Figure 2.2: Feynman diagram of the $\beta\beta$-decay.

The $\beta\beta$-decay is a very rare weak particle decay where the initial nucleus with atomic number Z transits under the emission of two electrons and two anti neutrinos into a daughter nucleus with increased atomic number of $\Delta Z = 2$ [10]:

$$(Z, A) \rightarrow (Z + 2, A) + 2\,e^- + 2\,\bar{\nu}_\mathrm{e} \quad . \tag{2.4}$$

The reaction takes place via two simultaneous β-decays and is consistent with the standard model (SM) [11]. Fig. 2.2 shows the Feynman diagram for the $\beta\beta$-decay. This decay is only possible, if the daughter nucleus $(Z + 2)$ resides in an energetically lower state than the initial one (Z). Additionally, the energy state of the intermediate nucleus $(Z + 1)$ needs to be higher than the initial one [9]. The binding energies of the nuclei is described in good approximation by the *Weizsäcker Mass Formula* [12]:

$$M(A,Z) = NM_n + ZM_p + Zm_e - a_v A + a_s A^{2/3} + a_c \frac{Z^2}{A^{1/3}} + a_a \frac{(N-Z)^2}{4A} + \frac{\delta}{A^{1/2}} \tag{2.5}$$

It contains a pairing term that is dependent on whether or not Z and the neutron number N are odd or even numbers:

$$\delta = \begin{cases} -11.2\,\mathrm{MeV}/c^2 & \text{for even } N \text{ and even } Z \\ 0 & \text{for odd } A \\ +11.2\,\mathrm{MeV}/c^2 & \text{for odd } N \text{ and odd } Z \end{cases}$$

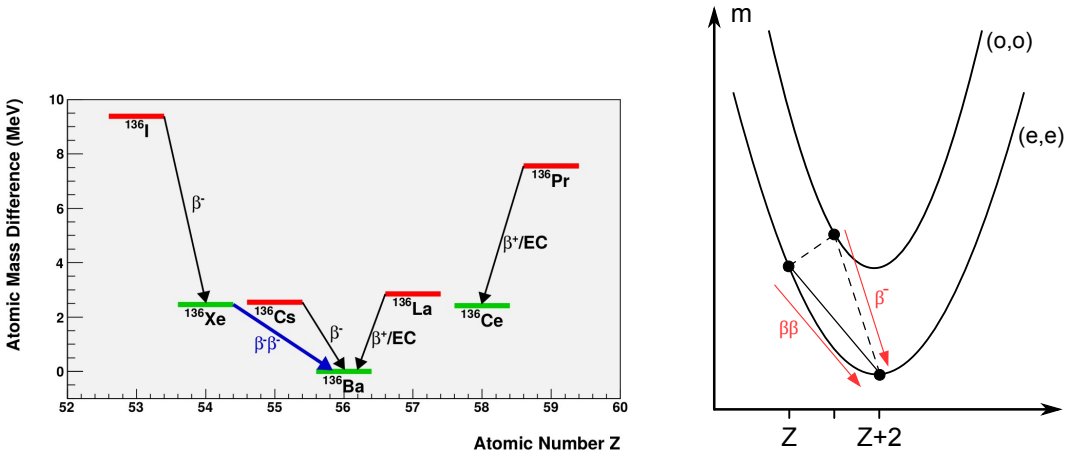

(a) (b)

Figure 2.3: (a) Isotopes with atomic mass $A = 136$. The atomic number Z is plotted against the atomic mass difference with respect to the mass of ^{136}Ba. The red marked nuclei have an atomic number / mass that is (odd , odd) and the green marked (even , even). The arrows β^-, β^+, $\beta^-\beta^-$ indicate the transition between the isotopes accompanied by the emission of an electron, positron and two electrons. EC indicates an electron capture. This image was taken from [9]. (b) Mass parabolas for a given atomic number A. Nuclei with lower energy E are more stable. The red arrow indicate the transitions whereat only transitions leading to a lower energy state are allowed. This image was redrawn from [13].

Nuclei with even N and even Z (further referred to as (even , even)) tend to have a larger binding energy than nuclei with the same A but with odd N and odd Z (further referred to as (odd , odd)). This difference in energy and nuclear mass can be visualized in form of two so called *Weizsäcker Mass Parabolas* (see fig. 2.3(b)) where a lower mass corresponds to a higher binding energy. The upper parabola is formed by (odd , odd) and the lower one by (even , even) nuclei. Some nuclei with given A , Z that do not reside in the lowest possible energy state for this A are not capable of undergoing a single β-decay. The daughter nucleus would end up in an energetically higher state. However, these nuclei may satisfy the constraints mentioned above leaving them with the possibility of undergoing a $\beta\beta$-decay [11]. An example for the ^{136}Xe nuclei is shown schematically in fig. 2.3(a).

35 nuclei are currently known to be able to undergo $\beta\beta$-decays. The first estimated half-life of the $\beta\beta$-decay measured geochemically for ^{130}Te was observed in 1950 by Ingram and Reynolds [14]. Since the first discovery of the $\beta\beta$-decay, various other nuclei were proven to be able to undergo this transition. The most recent discovery happened in 2011. The $\beta\beta$-decay of ^{136}Xe has been observed by the EXO-200 experiment for the first time. Tab. 2.1 shows a selection of nuclei, which have

Table 2.1: Current values for the half-life of $\beta\beta$-decay and the half-life limit of $0\nu\beta\beta$-decay for various isotopes.

Isotope	$T_{1/2}^{2\nu}$ [yrs]	$T_{1/2}^{0\nu}$ [yrs]
^{136}Xe	$(2.165 \pm 0.016^{\text{stat}} \pm 0.059^{\text{syst}}) \cdot 10^{21}$ [15]	$> 1.07 \cdot 10^{26}$ [16]
^{76}Ge	$(1.926^{+0.12}_{-0.08}) \cdot 10^{21}$ [17]	$> 2.1 \cdot 10^{25}$ [17]
^{100}Mo	$(6.93 \pm 0.04) \cdot 10^{18}$ [18]	$> 1.1 \cdot 10^{24}$ [18]

already been found undergoing the $\beta\beta$-decay and their experimentally estimated half-life $T_{1/2}^{2\nu}$. The $\beta\beta$-decay, as well as the neutrinoless decay mode, represent a second order weak interaction process. Their rates are proportional to G_{F}^2, where G_{F} is the Fermi constant. This constant denotes a measure for the interaction strength of weak processes. The long half-life implies a low decay rate.

2.3 Neutrinoless Double Beta Decay

The $0\nu\beta\beta$-decay is a hypothetical modification of the $\beta\beta$-decay where the initial nucleus undergoes the same transition but without the emission of neutrinos [19]:

$$(Z, A) \rightarrow (Z + 2, A) + 2e^- \quad . \tag{2.6}$$

The $0\nu\beta\beta$ is, unlike the ν-accompanied decay mode, forbidden by the SM. Fig. 2.4 shows the Feynman diagram for the $0\nu\beta\beta$-decay. The neutrino emitted at vertex 1 is being absorbed at vertex 2. The conditions for this to happen are explained

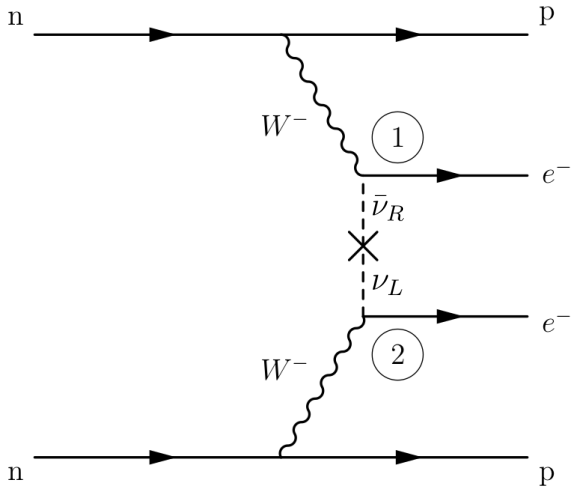

Figure 2.4: Feynman diagram of the $0\nu\beta\beta$-decay. The encircled numbers denote the vertices between the W^- bosons and the neutrinos.

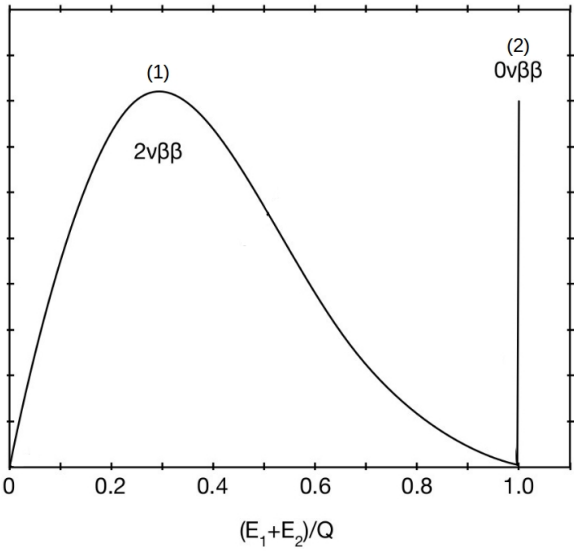

Figure 2.5: Energy spectrum of both emitted electrons in (1) a $\beta\beta$-decay and (2) a $0\nu\beta\beta$-decay. The energy is given with respect to the Q-value. The broad spectrum in (1) arises from the partition of the decay energy to the electrons and the neutrinos. In case of (2) the electrons receive the whole decay energy. This image was redrawn from [11].

below.

The total decay energy Q corresponds to the mass difference of the initial and the daughter nucleus [19]. Due to the big difference in mass between the daughter nucleus and the electrons, the recoil on the daughter nucleus is negligible so that the energy is fully distributed over the leptons. The kinetic energy of both electrons form a broad spectrum for the neutrino accompanied decay mode (see (1) in fig. 2.5), since the neutrinos receive part of the decay energy. In case of the $0\nu\beta\beta$-decay, the electrons get all of the decay energy. Therefore, the energy distribution of the electrons forms a sharp peak at the Q-value (see fig. 2.5(2)). The half-life of the $0\nu\beta\beta$-decay is even larger than the one of the $\beta\beta$-decay. For the exchange of two light Majorana neutrinos being the dominant decay channel of the $0\nu\beta\beta$-decay, the half-life can be expressed as [11]:

$$\left(T_{1/2}^{0\nu}\right)^{-1} = G^{0\nu} \left|M^{0\nu}\right|^2 \left(\frac{m_{\beta\beta}}{m_\mathrm{e}}\right)^2 \quad , \tag{2.7}$$

where $T_{1/2}^{0\nu}$ is the half-life of the $0\nu\beta\beta$-decay, $G^{0\nu}$ a phase space factor dependent on Z and N, $M^{0\nu}$ the model dependent nuclear matrix element that can only be approximated by complex calculations and m_e the electron mass.

The so called effective Majorana neutrino mass $m_{\beta\beta}$ can be written as a linear combination of the neutrino masses [20]:

$$m_{\beta\beta} = \left| \sum_{i=1}^{3} V_{\alpha i}^2 \, m_i \right| \quad , \tag{2.8}$$

where $V_{\alpha i}$ is the PMNS matrix (see equ. 2.1) multiplied with two additional CP violating Majorana phases α_1 and α_2:

$$V_{\alpha i} = U_{\alpha i} \times \mathrm{diag}\left(1, e^{i\frac{\alpha_{21}}{2}}, e^{i\frac{\alpha_{31}}{2}}\right) \quad . \tag{2.9}$$

Three conditions need to be fulfilled so the $0\nu\beta\beta$-decay may exist:

- The neutrino needs to be a massive particle. This is not given in the SM. However, neutrino oscillation experiments confirmed, that neutrinos do have a non zero mass [4].
- The neutrino needs to be a Majorana particle $\nu \equiv \bar{\nu} \equiv \nu_{\mathrm{M}}$. The SM claims that the neutrino is a Dirac particle (a particle that is different from its anti-particle). This assumption is based on observations only. There is no fermion that possesses the potential of being a Majorana particle except the neutrino, since it is the only electrically neutral lepton. Therefore, it cannot be distinguished per se from its anti-particle.
- There needs to be a process adapting the helicity between the vertices 1 and 2 in fig. 2.4. There are various hypothetical mechanisms explaining this transition. The two most common are explained below.

1) Since a massive particle with helicity $H = +1$ in the reference frame A always propagates with $v < c$, there is a reference frame B moving with $v_{\mathrm{B}} > v$ in A. The direction of the particle's momentum in B is reversed to the direction in A. The spin configuration, however, stays the same. With the helicity:

$$\mathrm{H}_A = \vec{\sigma}\vec{p} \quad , \tag{2.10}$$

one finds the helicity in B opposite to the one in A:

$$H_{\mathrm{B}} = \vec{\sigma}(-\vec{p}) = -H_{\mathrm{A}} \quad . \tag{2.11}$$

For massless particles a reference frame B with $v_B > v$ does not exist. According to [5], the probability W that the neutrino ends up with a reversed helicity at vertex 2 is:

$$W = \frac{1}{2}\left(1 - \frac{v}{c}\right) \approx \left(\frac{m_\nu}{2\,E_\nu}\right) \quad , \tag{2.12}$$

which is highly suppressed due to the small neutrino mass.

2) The so called V-A Theory was invented to explain parity violation in the *Wu*-experiment. It implies a left-handed charged coupling to the weak force only. A process in which the weak force couples to a right-handed charged current has not been observed yet. Nevertheless, there is a possibility that the right-handed neutrino emitted at vertex 1 does not need to change its helicity. The probability for this interaction is proportional to the coupling constant η with $|\eta| << 1$ [5, 9].

Besides the reaction outlined in equ. 2.6, there are three further lepton number violating processes that are closely related to the $0\nu\beta\beta$-decay [9]:

$$0\nu\beta^+\beta^+ : (Z\,,\,A) \rightarrow (Z-2\,,\,A) + 2\,\mathrm{e}^+ \quad , \tag{2.13}$$

$$\mathrm{EC}0\nu\beta^+ : \mathrm{e}^- + (Z\,,\,A) \rightarrow (Z-2\,,\,A) + e^+ \quad , \tag{2.14}$$

$$0\nu\mathrm{ECEC} : 2\,\mathrm{e}^- + (Z\,,\,A) \rightarrow (Z-2\,,\,A) \quad , \tag{2.15}$$

where $0\nu\beta^+\beta^+$ denotes the double positron emission, $\mathrm{EC}0\nu\beta^+$ the single positron emission plus single electron capture (EC) and 0νECEC the double electron capture [9].

2.4 Importance of the Neutrinoless Double Beta Decay for Physics

The existence of the $0\nu\beta\beta$-decay would imply a violation of the lepton number conservation by a factor of 2 (see fig. 2.6). The fact that the lepton number is violated by the creation of two electrons supports the theory that leptons took part in leptogenesis that might explain the matter-antimatter asymmetry after the big bang. In addition, the neutrino would be the first Majorana particle [11]. The effective Majorana neutrino mass $m_{\beta\beta}$ is, according to equ. 2.8, directly linked to the neutrino oscillation phenomenology. It depends on the absolute mass scale and can therefore provide information about the mass hierarchy (see sec. 2.1) [11]. Fig. 2.6 shows $m_{\beta\beta}$ in dependence on the lightest neutrino mass m_{light}. The colored bands correspond to the possible hierarchies (green = inverted hierarchy, red = normal hierarchy). The width of the bands result from uncertainties on the neutrino

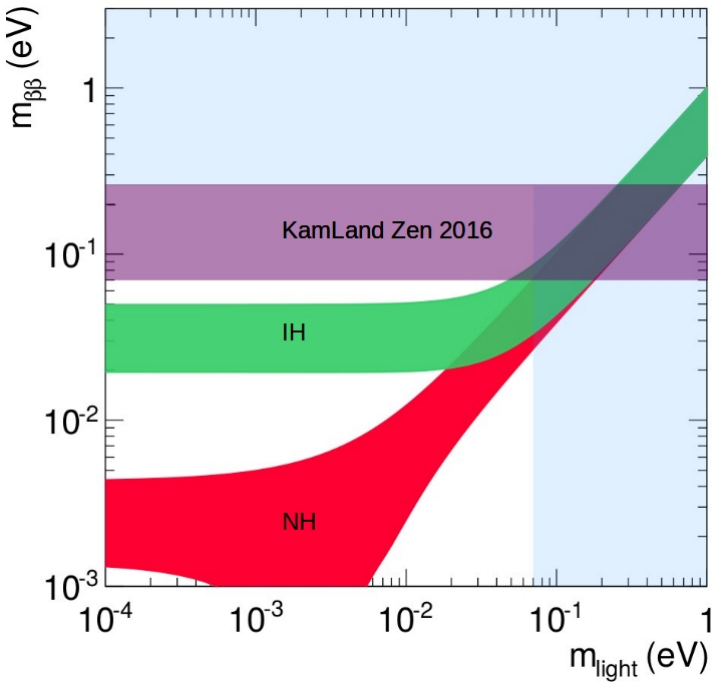

Figure 2.6: Lightest neutrino mass in dependence on the effective Majorana neutrino mass. The green band indicates the area where the inverted neutrino mass hierarchy is probably to be found. The red band shows the same for the normal neutrino mass hierarchy. The width of the bands results from uncertainties on the neutrino mixing parameters. The light blue areas indicate current limits on m_{light} and $m_{\beta\beta}$. This image was redrawn from [11]. The purple area indicates the currently best limit on $m_{\beta\beta}$ measured by KamLAND-Zen [16].

mixing parameters. The vertical light blue area represents an upper limit on the lightest neutrino mass from cosmological measurements ($m_{\text{light}} > 0.07\,\text{eV}$) [11]. The horizontal light blue area corresponds to upper limits on $m_{\beta\beta}$ coming from $0\nu\beta\beta$ experiments, whereas the purple band shows the current lowest limit from KamLAND-Zen ($m_{\beta\beta} < 60\,\text{meV} - 161\,\text{meV}$) [16]. With experiments that are more sensitive to $m_{\beta\beta}$, the constraints could drop under the degenerated hierarchy region. Therefore, the inverted hierarchy could be excluded even if the exact value for $m_{\beta\beta}$ is not known.

2.5 Measurement Principle

All $0\nu\beta\beta$ experiments are based on calorimetry of the two electrons created in the $\beta\beta$-decay and $0\nu\beta\beta$-decay. Fig. 2.5 shows the distribution of the sum of both electron energies for the $\beta\beta$-decay (1) and the $0\nu\beta\beta$-decay (2). If this transition exists, both distributions would occur although the spectrum of the neutrino

accompanied decay would be dominant. To build an adequate detector system, an estimation of the expected event rate needs to be done. The number of $0\nu\beta\beta$ events that are expected within an acquisition time t can be expressed as [9]:

$$N_{0\nu\beta\beta} = \log(2)\frac{M_{\beta\beta} \cdot N_{\mathrm{A}}}{W_{\beta\beta}} \cdot \varepsilon \cdot \frac{t}{T_{1/2}^{0\nu\beta\beta}} \quad , \tag{2.16}$$

where $N^{0\nu}$ is the number of detected events, $M_{\beta\beta}$ the mass of the $\beta\beta$ emitting isotope, N_A the *Avogadro*-constant, $W_{\beta\beta}$ the molar mass of the isotope, ε the detector efficiency, $T_{1/2}^{0\nu}$ the half-life of the $0\nu\beta\beta$-decay and t the observation time. If we assume an effective Majorana neutrino mass of 50 meV, which corresponds to a half-life of $T_{1/2}^{0\nu\beta\beta} \approx (10^{26} - 10^{27})$ yrs, a perfect detector ($\varepsilon = 1$) and a macroscopic detector mass of 100 kg, the expected event rate would be one event per year [11]. Even under perfect conditions, a detector of a realistic size would produce a very low amount of data. Considering a real detector ($\varepsilon < 1$) the adaptable data rate drops even further. A good background reduction and high energy resolution is required in order to separate $0\nu\beta\beta$ events from background signatures in the region of interest (ROI) and from $\beta\beta$ events. To obtain a suitable detector, the choice of the isotope is very important. On the one hand background reduction and energy resolution need to be optimized. On the other hand, a scalability of a suitable detector mass needs to be enabled, since the detector can only be maintained for a limited time. In addition, due to background limitations, the energy resolution η improves with [9]:

$$\eta \propto \sqrt[4]{M_{\beta\beta} \cdot t} \quad . \tag{2.17}$$

These constraints result in a few criteria for the choice of the isotope [21]:

- The Q-value should be as high as possible to have a minimum of radioactive background in the ROI. High Q-values also correspond to high phase space factors. Therefore, according to equ. 2.7, isotopes with high Q-values tend to have lower half-lifes and are favored due to higher event rates [9].

- The investigated isotope needs to be enriched for almost all $0\nu\beta\beta$-experiments. Therefore, the natural abundance should be as high as possible.

- The isotope needs to be compatible with a certain detection technique where the source can be separated from the detector material or can also be used as such.

These criteria result in an assembly of nuclei that are more frequently used as decay sources in experiments. Some examples with their Q-values and natural abundances χ are shown in tab. 2.2. There are basically three ways to acquire the energy information of the two created electrons:

- Temperature measurement by a bolometric detector.
- Photon readout of the scintillation light via classical light detection systems like photomultiplier tubes (PMT) or silicon photomultipliers (SiPM).
- Charge read out of secondary electrons produced in scattering processes of the primary electrons with the detector material.

Table 2.2 shows the measurement principle for a selection of experiments. Experiments like KamLAND-Zen use only light information coming from scintillation material. GERDA and MAJORANA use only charge information coming from Germanium diode detectors. CUORE uses the temperature information to measure the electron energy. EXO-200 uses the energy information coming from scintillation light in Xe as well as the one gathered by a charge read out (see sec. 2.5.1). The usage of both signals increases the energy resolution.

In the following, setup and detection principle of two experiments, the successful EXO-200 (**E**nriched **X**enon **O**bservatory) experiment and the future nEXO experiment, which benefits from experience gained by EXO-200, are discussed in detail.

Table 2.2: Selection of often used $\beta\beta$ isotopes, their natural abundances χ, Q-value and measurement principle to acquire the electron energy information.

Nuclei	χ [%]	Q-value [keV]	Experiments	Measurement
^{130}Te	34.08 [21]	2528 [22]	CUORE [22]	Bolometric
^{136}Xe	8.9 [23]	2458 [24]	EXO-200 [23]	LXe TPC
			KamLAND-ZEN [25]	Scintillation
^{76}Ge	7.8 [26]	2039 [23]	GERDA [26]	Ge diodes
			MAJORANA D. [27]	Ge diodes
^{48}Ca	0.187 [21, 23]	4263 [21]	CANDLES [28]	Scintillation

2.5.1 The EXO-200 Experiment

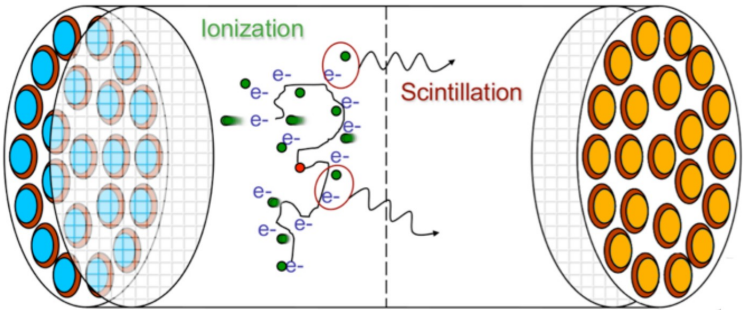

Figure 2.7: Two sided single phase EXO-200 TPC. APDs at the top and bottom side of the cylinder serve as scintillation light detectors. Wire grids (U- and V-wires) mounted in front of the APDs serve as charge collectors. An electric field is applied between the cathode (dashed line) in the middle of the TPC and the U-wires at both side of the cylinder. This image was taken from [29].

The EXO-200 experiment was designed to search for the $\beta\beta$-decay of the ^{136}Xe nucleus with a single phase liquid xenon detector and, at the same time, to test new detection technologies for future larger experiments [30]. The experiment is located at the WIPP (Waste Isolation Pilot Plant) in New Mexico in a depth of 655 m (1500 m.w.e.) to be shielded from cosmic and atmospheric radiation. A total of 477.60 ± 0.01 live days of data were collected between September 2011 and September 2013 [24]. In November 2011, the EXO-200 collaboration published results of the first direct observation of the $\beta\beta$-decay of the ^{136}Xe nucleus [31]. The experiment operates with about 175 kg of liquid xenon that is enriched to 80.6 % in ^{136}Xe. The detector is a cylindrical, two sided time projection chamber (TPC) with a length of 44 cm and a diameter of each 40 cm. Avalanche photodiodes (APDs) are placed at the top and the bottom side of the cylinder to detect xenon scintillation light. A pair of crossed wire planes (so called U- and V-wires) are strained in front of the APDs. These wire planes read out the ionization signal. An electric field of about 8 kV is applied between a cathode wire grid in the middle of the detector and the U-wires at the top and the bottom side of the cylinder. Copper field shaping rings that grade the electric field are arranged concentric around the cylinder axis. The whole TPC is placed in a vacuum insulated cryostat filled with HFE (hydrofluoroether). The HFE provides both shielding and thermal uniformity [30].

Fig. 2.7 shows a scheme of the detection principle of the EXO-200 TPC. The electrons that are created in a $\beta\beta$-decay ionize xenon atoms and cause the xenon to scintillate (see sec. 3.3). The scintillation light is detected by the APDs. The electrons that are released from the xenon atoms due to ionization are drifted

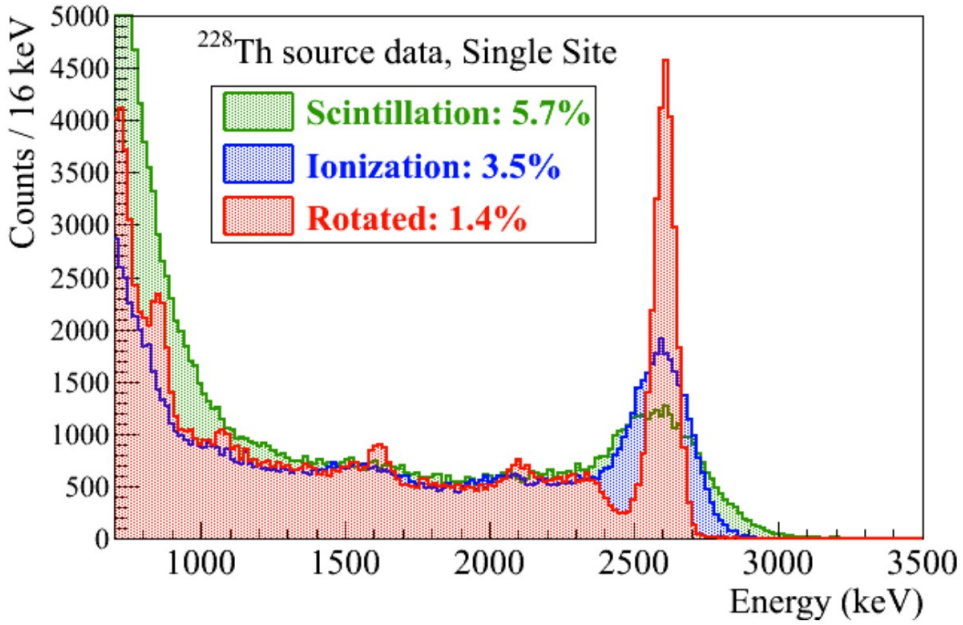

Figure 2.8: Calibration measurement with energy information from scintillation light (green) and charge readout (blue). The combined signals yield a more precise energy resolution (red). The calibration was performed with ^{208}Tl, which is part of the ^{228}Th decay chain. The energy of the γ signature of ^{208}Tl is 2510 keV, which is very close to the Q-value of ^{136}Xe with 2458 keV. This image was taken from [29].

along the electric field lines towards the U- and V-wires where the charge carrier's signal is read out. The amount of light as well as the number of collected charges is proportional to the energy of the electrons created in the decay. This way, the energy information about the initial electrons can be gathered with two different signals. Fig. 2.8 shows the measured energy distributions for the ionization signal (blue), the scintillation signal (green) and the combined signals (red). This measurement was done with a ^{228}Th calibration source that has a distinct γ-signature at 2510 keV. The combined energy resolution from the charge signal (3.5 %) and the scintillation signal (5.7 %) yield the current energy resolution of 1.4 % in the ROI [15, 30, 32].

The EXO-200 experiment has provided the most precise measurement of the $\beta\beta$-decay half-life of the ^{136}Xe nucleus to be $(2.165 \pm 0.016^{\text{stat}} \pm 0.059^{\text{syst}}) \cdot 10^{21}$ yrs. Although the EXO-200 experiment has proven that a TPC provides a functional detection principle for the $0\nu\beta\beta$-decay, the exposure with possible $0\nu\beta\beta$ signals is too small to acquire sufficient data to search for the $0\nu\beta\beta$-decay in a realistic time. A much larger detector mass and, therefore, a much larger exposure with possible $0\nu\beta\beta$ signals is required to set new limits on the half-life of the $0\nu\beta\beta$-decay.

2.5.2 The nEXO Experiment

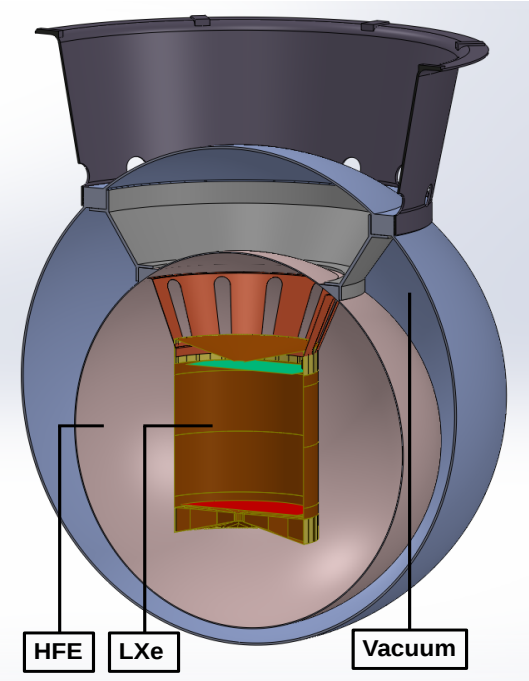

Figure 2.9: nEXO experimental setup. The TPC that contains the liquid xenon is placed in a tank filled with HFE. This tank is vacuum insulated. This image was taken from [33].

The future nEXO experiment is designed to search for the $0\nu\beta\beta$-decay of the ^{136}Xe nucleus with a single phase liquid xenon TPC. It will probably be placed in the Creighton mine in Canada, 2000 m under ground (6000 m.w.e.). It is planed to take data for at least five years [29]. It operates with about five tons of liquid xenon that is enriched to >90 % in ^{136}Xe. The detector is a cylindrical TPC that is about 130 cm in length and 130 cm in diameter (see fig. 2.10). SiPMs that detect xenon scintillation light are mounted to the barrel of the cylinder. Charge readout tiles that read out the ionization signal are mounted to the top side of the TPC. An electric field of about 60 kV is applied between a cathode at the bottom side of the cylinder and an anode behind the charge readout tiles. Copper field shaping rings that grade the electric field are arranged in front of the SiPMs. The whole TPC is placed in a vacuum insulated cryostat that is filled with HFE (see fig. 2.9). This cryostat is placed in a 13 m diameter water tank where PMTs are mounted to the inside surface. The water provides shielding from radioactive background and is, together with the PMTs, used as muon veto [33].

The detection principle of the nEXO detector is similar to the EXO-200 detector. The nEXO experiment is designed to reach an energy resolution of $\frac{\Delta E}{E} < 1\,\%$ at the Q-value (2458 keV) [35]. It is expected that nEXO is able to shift the current limit on the $0\nu\beta\beta$ half-life of ^{136}Xe to $T^{0\nu}_{1/2} > 10^{28}$ yrs and the limit on $m_{\beta\beta}$ down to 5 meV - 18 meV [33, 36]. Therefore, nEXO is expected to cover the full range of the inverted hierarchy after five years of measurement time. Fig. 2.11 shows the effective Majorana neutrino mass $m_{\beta\beta}$ in dependence on the lightest neutrino mass m_{light} for the normal hierarchy (red) and the inverted hierarchy (blue). The upper horizontal light blue band denotes the limit on $m_{\beta\beta}$ that was set

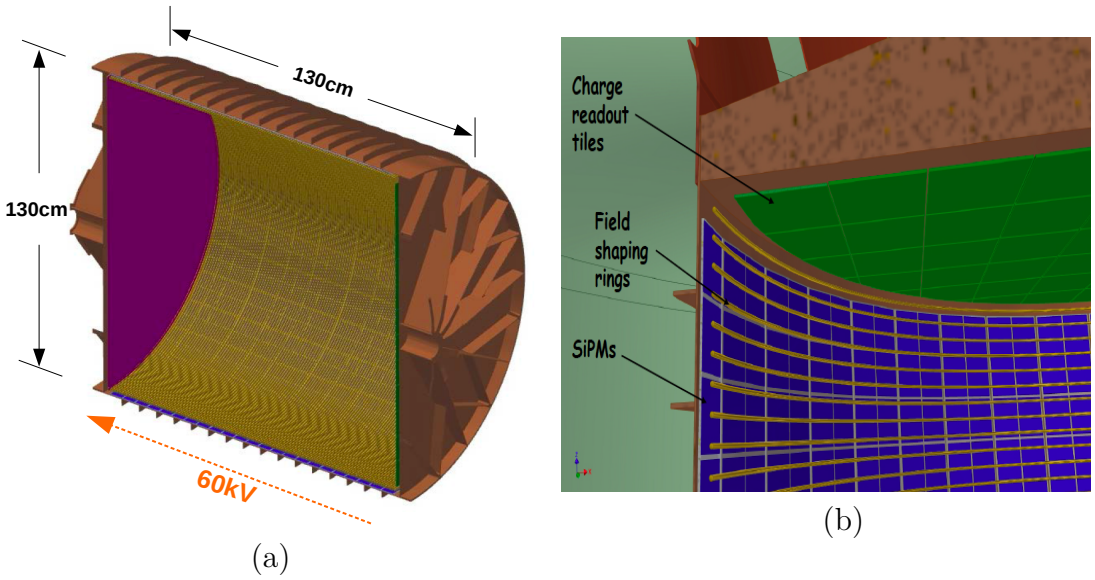

Figure 2.10: (a) Cross section of the nEXO TPC. The cylinder is 130 cm long and 130 cm in diameter. An electric potential of 60 kV is applied from the top to the bottom side. (b) Close up of the top side of the TPC. Charge readout tiles on the top side and SiPMs on the barrel collect the energy information from the charge signal and the scintillation light respectively. Field shaping rings that are mounted concentric to the barrel align the electric field [33].

by EXO-200 in 2014. The pink band denotes the predicted limit on $m_{\beta\beta}$ that is expected to be set by EXO-200 with data from current measurements (Phase-II). The lower blue band denotes the predicted limit that is expected to be set by nEXO within five years of data taking. The required energy resolution at the Q-value is very important to set new limits on $T^{0\nu}_{1/2}$ and $m_{\beta\beta}$. Since the nEXO experiment is still under research and development (R&D), improvements on the photon detection, charge collection and the TPC design are currently done in order to achieve the 1 % energy resolution. Especially SiPMs are investigated with respect to the requirements (see sec. 3.2.5) of the nEXO experiment. By the time this thesis is written, no suitable SiPM that meets these requirements was found.

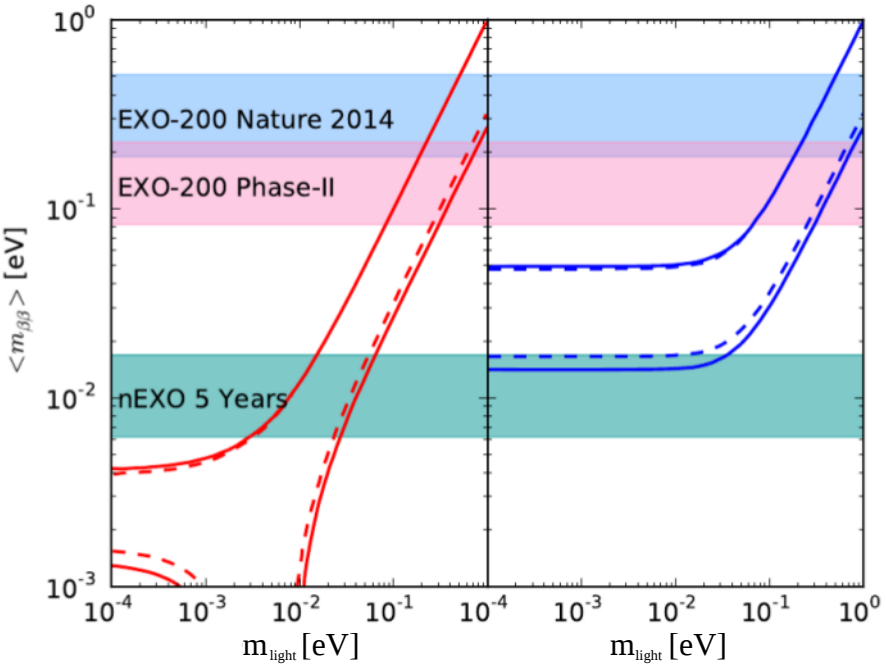

Figure 2.11: Effective Majorana neutrino mass in dependence on the lightest neutrino mass for the normal hierarchy (red) and the inverted hierarchy (blue). The horizontal bands denote the limits on $m_{\beta\beta}$ by EXO-200 and what nEXO is expected to achieve within five years of data taking. This image was taken from [37].

3 Light Detection

This chapter provides an overview of the setup and operation principle of the detector systems that were used in the experiments in this thesis. Characteristic properties of these devices that are investigated later are outlined. Light production in xenon via scintillation is explained. The working principle of a wavelength shifting material is introduced.

3.1 Photomultiplier Tube

A photomultiplier tube (PMT) is a photon detection device that is capable of measuring very low amounts of light. The light signal is converted into an electric current that can be read out. PMTs represent an established technology that is often used in nuclear and particle physics experiments [38].

3.1.1 Setup and Detection Principle

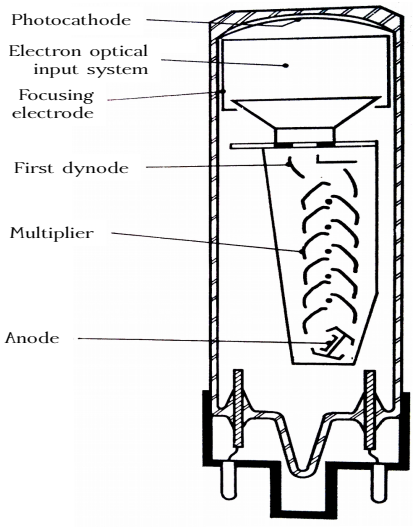

Figure 3.1: Scheme of the setup of a PMT with dynode electron multiplication system. This image was taken from [38].

Fig. 3.1 shows a scheme of the setup of a common PMT with a dynode amplification system. It consists of a photosensitive cathode, an electron focusing system, a dynode system for amplification and an anode that is connected to the signal readout electronic. The whole device is set up in an evacuated glass tube. An electric potential, which is usually in the oder of a few kV, is applied between the cathode, the dynodes and the anode. The potential rises at every dynode and the anode with respect to the photocathode [38]. When a photon impinges onto the photocathode, an electron may be emitted from the cathode material via photoelectric effect. The electron focusing system leads the photoelectron to the dynode system.

The photoelectron is accelerated to the first dynode due to the electric potential. The dynodes consist of a material that can easily emit further electrons if an initial electron impinges onto a dynode. The secondary electrons that are emitted by the first dynode are accelerated to the second dynode where further electrons are emitted and so forth. This implies a multiplication of the photoelectron until the electron cascade emitted by the last dynode is accelerated towards the anode where it can be read out as a current signal [38]. There are various modifications of the dynode system. The PMT that was used in the experiments in this thesis (see fig. 3.2) is of the so called metal channel type. The dynodes in this fabrication type consist of thin metal layers that can be arranged very close to each other. Rise and fall time of a signal from this PMT type are usually shorter than from signals of other fabrication types. Additionally, PMTs of this fabrication type can be built very small and compact [39].

Figure 3.2: Image of a Hamamatsu R8520-406 that was used in the experiments. This image was taken from [39].

3.1.2 Characteristic Properties

Quantum Efficiency

The electron multiplication that takes place in the dynode system usually is in the order of $10^5 - 10^6$. The measured current is proportional to the number of photoelectrons, which is proportional to the number of incident photons. The equation [38, 40]:

$$E_{e^-} = h\nu - \Phi \tag{3.1}$$

describes the energy transfer from the incident photon to the emitted photoelectron, where E_{e^-} is the kinetic energy of the electron, ν the frequency of the incoming photon, h the Planck constant and Φ the work function. Since Φ describes the minimum energy that needs to be applied to separate the electron from the material only photons with a certain energy $h\nu^*$ can perform the photoelectric effect. Hereby, ν^* is the minimum frequency a photon needs to have.

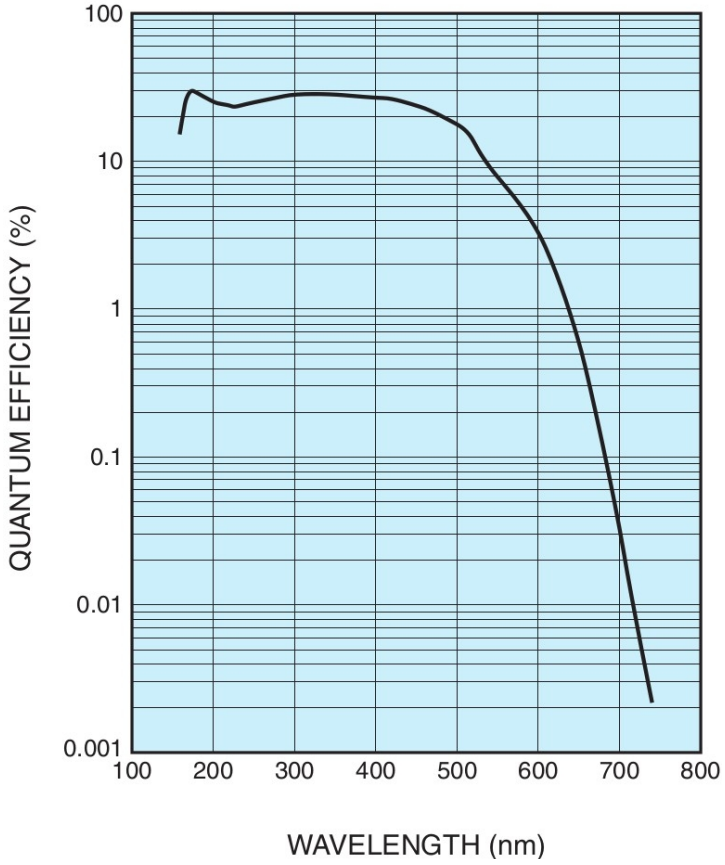

Figure 3.3: QE on the photocathode for a Hamamatsu R8520-406 with bialkali cathode material. This image was taken from [39].

The quantum efficiency QE is defined as [38]:

$$QE = \frac{N_{\mathrm{e}^-}}{N_\gamma(\lambda)} \quad , \tag{3.2}$$

where N_γ is the number of incident photons and N_{e^-} the number of electrons that are released from the photocathode. QE depends on the wavelength λ of the incident photon. Fig. 3.3 shows QE of a Hamamatsu R8520-406, the PMT that was used in the experiments in this thesis. The spectrum of QE varies with the photocathode material. The limits on the wavelength where a photon can still release an electron from the cathode material are in a range from 150 nm to 1600 nm. The PMT used in the experiments in this thesis has a bialkali photocathode with the highest value of QE at a wavelength of 420 nm. QE is between 15 % and 32 % in the region of vacuum ultra violet (VUV) light.

Gain

The gain denotes the amplification factor by which the initial photoelectron is multiplied in the dynode system. It depends on the number of dynodes n and a material dependent emission factor δ. This emission factor is a function of the interstage voltage U_d between the dynodes. For one stage δ can be written as [38]:

$$\delta = K \cdot U_\mathrm{d} \quad , \tag{3.3}$$

where K is a material dependent proportionality factor. This multiplication takes place at every dynode. The multiplication factor between the photocathode and the last dynode is defined as: [38]:

$$G = \delta^n = (\mathrm{K} \cdot U_\mathrm{d})^n \quad . \tag{3.4}$$

This expression denotes the gain G of the PMT.

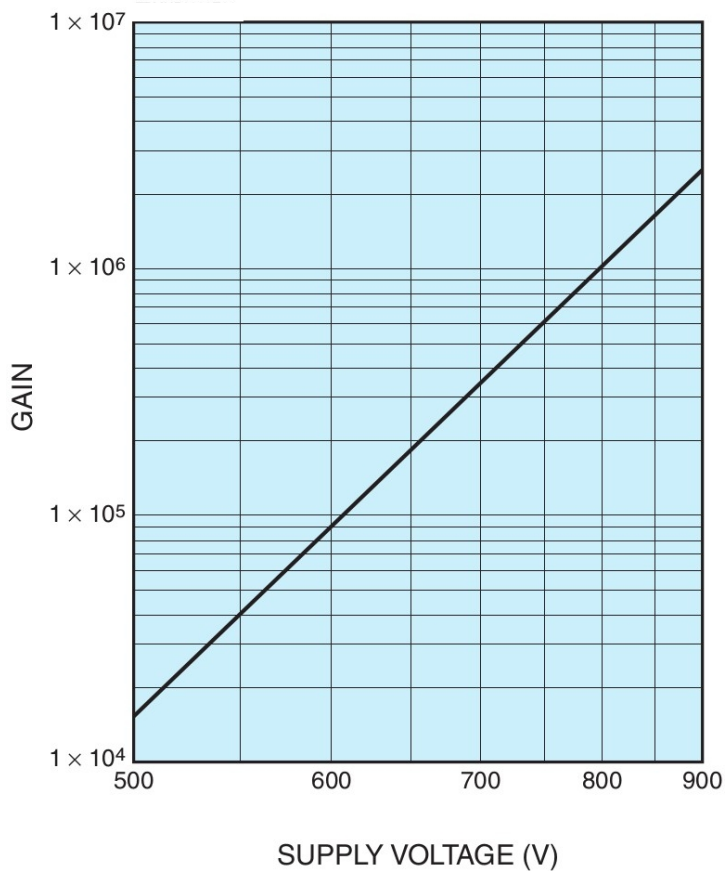

Figure 3.4: Gain in dependence on the supply voltage U_signal for a Hamamatsu R8520-406 with bialkali cathode material. This image was taken from [39].

Fig. 3.4 shows the gain of the used PMT in dependence on the supply voltage U_{signal}. The gain and, therefore, the number of charges that are read out as a signal rises exponentially with U_{signal}. This also increases the number of signals that were not induced by an incident photon but by randomly emitted electrons at the photocathode or the dynodes. These so called dark count signals occur more frequently with higher gain. The number of dark count signals per time interval is called dark rate. The dark rate is temperature dependent. A higher thermal energy of the electrons in the photocathode and dynode material decreases the binding energy of the electron to the material. This makes it more likely, that an electron is randomly released from the material. The dark rate of the used PMT is about 1 kHz at room temperature and about a few Hz at −100 °C. Since the expected signal rate in the experiments is about 4 kHz, the dark rate can be neglected.

3.2 Silicon Photomultiplier

A silicon photomultiplier (SiPM) is a semiconductor based photon detection device that is capable of detecting single photons. It consists of 100 to 90000 pixels that are connected in parallel. Each pixel works as an APD that is operated in Geiger mode above a certain threshold voltage called *breakdown voltage* U_{break}. This is the level, above which the diode can be electrically conducting and incident photons can produce current signals [35, 41].

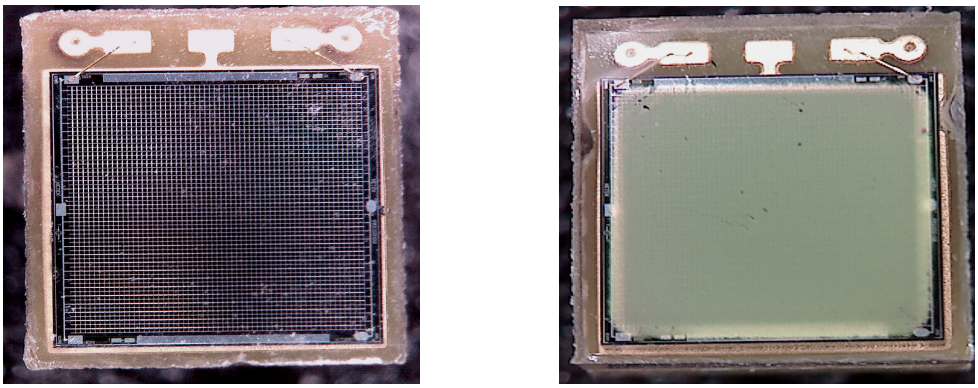

(a) (b)

Figure 3.5: (a) Magnified image of a KETEK PM3350 SiPM without wavelength shifter coating. The actual semiconductor material is encased in epoxy. (b) Magnified image of the PM3350 SiPM with wavelength shifter coating that was used in the experiments in this thesis. The wavelength shifter covers the entrance window in form of a thin green film.

Fig. 3.5(b) shows a magnified image of a KETEK PM3350 SiPM, which is coated with a wavelength shifter and that was used in the experiments in this thesis. It is encased in epoxy that is not transparent for VUV light. The wavelength shifter covers the entrance window in form of a 1 µm thin layer [42]. Fig. 3.5(a) shows a magnified image of an uncoated KETEK PM3350 SiPM. The pixel structure and the wire bonds (golden wires at the top left and top right of the pixel matrix) for the supply voltage are visible.

3.2.1 Setup and Detection Principle

Doping a semiconductor that consists of atoms with a certain number m of valence electrons means integrating impurity atoms with a different number j of valence electrons into the material. The material is called n-doped / p-doped if an electron donor ($m + i$ valence electrons) / acceptor ($m - i$ valence electrons) is introduced. The additional valence electrons coming from the impurity atoms in an n-doped semiconductor have a lower binding energy than the ones from the semiconductor material. Therefore, the density of quasi free electrons increases. Vice versa, since the impurity atoms in a p-doped semiconductor have a lower number of valence electrons and, therefore, a higher affinity to accept electrons, the density of electron holes (e-h) increases. The electrical properties of the semiconductor vary not only by the kind of the introduced impurity atoms, but also by their number. A highly p-doped semiconductor is referred to as p^+ material, a moderately p-doped semiconductor as p material and a low p-doped semiconductor as p^- material. This denomination is analogous for n-doped semiconductors. The concentration of impurity atoms lies between 10^{-8} for p^- / n^-- doped and 10^{-4} for p^+ / n^+- doped materials [40].

Fig. 3.6 (a) shows a scheme of a possible topological structure of a SiPM. The bottom layer (orange) consists of a p^+-doped material, the layer above (dark blue) consists of a p^--doped material, followed by a p-doped layer (light blue). The entrance window of every pixel (red) consists of an n^+-doped material. Every entrance window is coated with an anti-reflective layer in order to reduce losses due to photon reflection. The pixels are separated by metal filled trenches to prevent crosstalk (see sec. 3.2.4). So called quenching resistors and contacts for the applied bias voltage are mounted to the top side of the SiPM, separating each entrance window. Every pixel is connected in series with a quenching resistor R_{Q}. The pixels are all connected in parallel to each other. A bias voltage U_{bias} is applied to the pixels. Fig. 3.6(b) shows an equivalent circuit of this model [41].

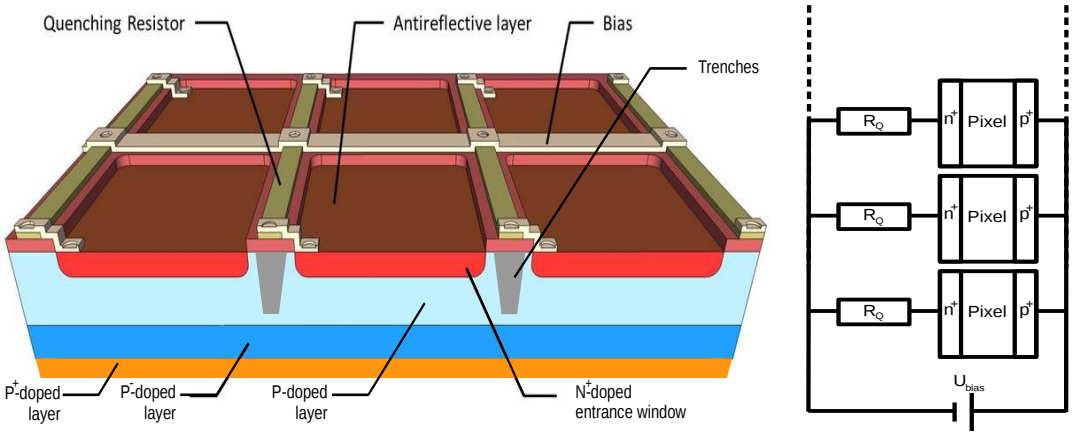

Figure 3.6: (a) Scheme of a possible topological structure of a SiPM [41, 43]. This image was modified and redrawn from [43]. (b) Equivalent circuit of the pixels with the quenching resistors.

3.2.2 Static Case

Fig. 3.7 shows a scheme of the charge distribution in a pixel. The quasi free electrons from the n^+ side drift towards the p^+ side and recombine with the holes and vice versa. This forms a potential and creates a depletion region between both layers. The intrinsic p^--doped layer forms the region where photon absorption mainly takes place. The p-doped and the n^+-doped layer form a p-n^+ junction. This causes the potential to rise between those layers. The applied bias voltage intensifies this effect. In the case of silicon (valence of 4) as semiconductor material, impurity atoms with a valence of 5 are introduced in p-doped layers and impurity atoms with a valence of 3 in n-doped layers [44].

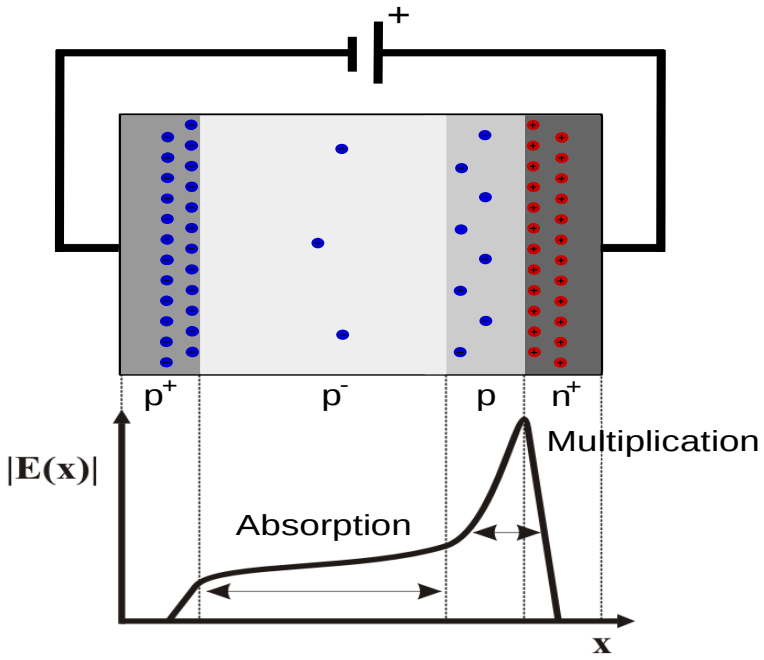

Figure 3.7: Static charge distribution in a single pixel. Blue dots represent negative charges, red dots represent electron holes. An electric field is applied between the p^+ doped side and the n^+ doped side. In between the p^+ layer and the p layer resides the p^- layer where absorption is most likely to happen. The electric potential rises towards the interface of the p and n^+ layer. This image was redrawn from [45].

3.2.3 Dynamic Case

The intrinsic p^--doped layer (100 µm - 1 mm) is several orders of magnitude thicker than the other ones (10 nm - 100 nm). The thickness of the intrinsic layer is chosen to be in the range of the absorption length of the photons with the wavelength to be primarily detected. Therefore, it is most likely for a photon to be absorbed in the intrinsic layer. Fig. 3.8 shows the principle of the electron multiplication process in a pixel when a photon is absorbed. If the photon energy E_γ is high enough, the inner photo effect can happen. The photon is absorbed by an atom, which is ionized. An electron, the so called photoelectron, is excited from the valence band to the conduction band leaving a hole in the valence band. This way, an e-h pair is created. Due to the electric field, the photoelectron is drifted towards the n^+-doped layer and the hole in the other direction. The electric field strength increases towards the p-n^+ junction. Therefore, the photoelectron acquires enough energy to create further secondary e-h pairs. The electrons from these processes create e-h pairs as well. This mechanism causes a charge avalanche in the pixel [44].

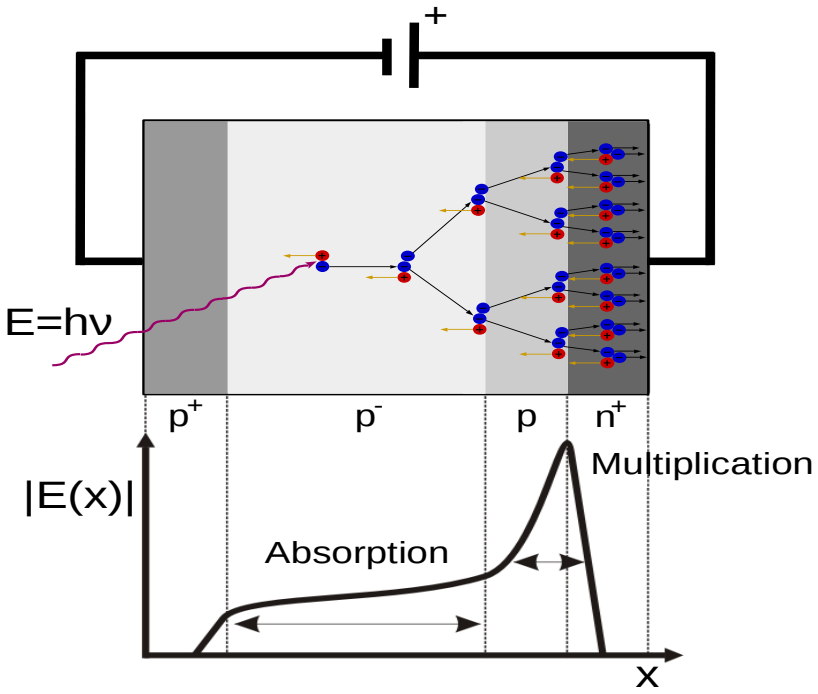

Figure 3.8: Principle of the electron multiplication process in a pixel when a photon creates an e-h pair in the intrinsic layer. Negative charges (blue) are drifted towards the n^+ doped layer, electron holes (red) are drifted in the other direction. Further e-h pairs can be created causing a charge avalanche in the pixel. This avalanche can be measured as a charge signal. This image was redrawn from [46].

The mean number of secondary electrons in the charge avalanche per photoelectron determines the gain G of the SiPM. It is proportional to the overvoltage $U_{\text{over}} = |U_{\text{bias}} - U_{\text{break}}|$ and the pixel capacitance C_{D} [47]:

$$G = \frac{C_{\text{D}} \cdot U_{\text{over}}}{e} \quad , \tag{3.5}$$

where e is the elementary charge. If the applied bias voltage U_{bias} is lower than the breakdown voltage U_{break} electron multiplication cannot occur.

The SiPM forms a photo diode. Each pixel can be described with an equivalent circuit shown in fig. 3.9(a). A capacitor C_{D} and a resistor R_{D} that represent the diode capacitance and resistance are connected in parallel. The potential U_{break} is poled in opposite direction to the potential U_{bias}. The switch S is a substitute for an incoming photon that produces an avalanche. As long as S is open, the SiPM behaves as it is described in the static case. There is no current but a potential U_{D} across the diode equal to U_{bias}. C_{D} is charged with U_{bias} [41]. If an avalanche

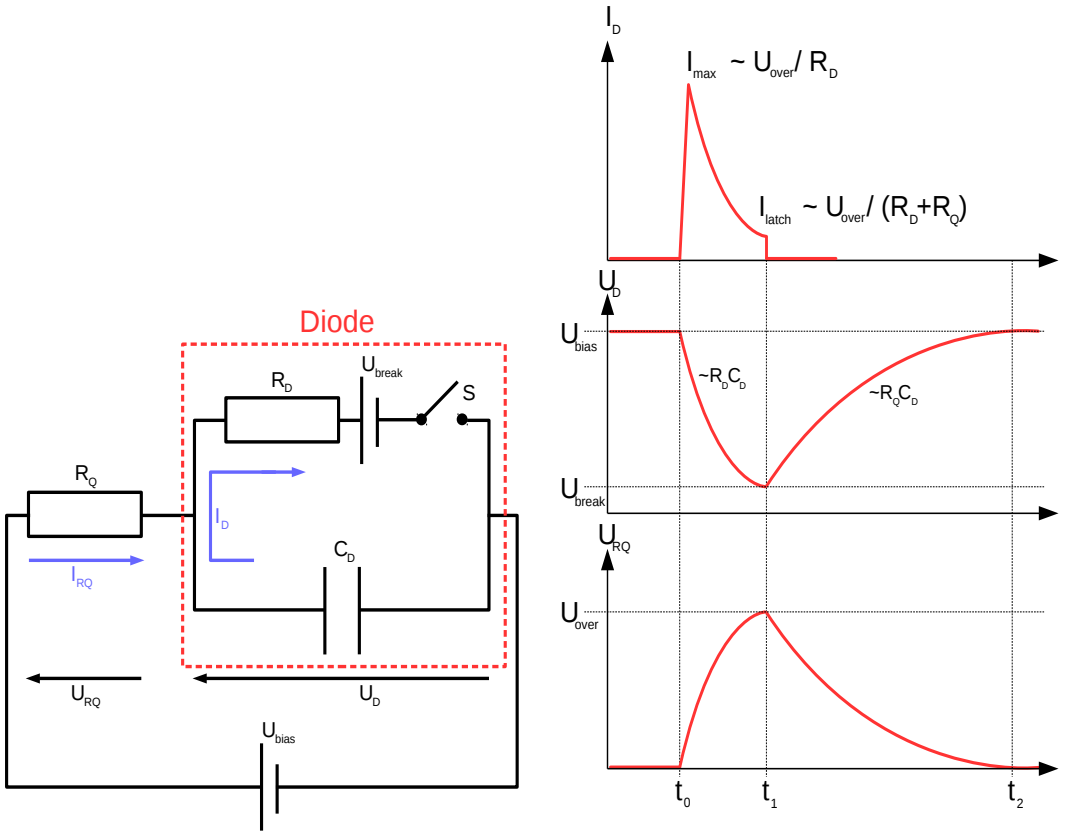

Figure 3.9: (a) Equivalent circuit for an ideal pixel (red dashed line). The pixel is connected in line with the bias voltage U_{bias} and the quenching resistor R_{Q}. (b) Time evolution of the current I_{D} in the pixel (top), the potential U_{D} across the pixel (middle) and the potential U_{RQ} across the quenching resistor (bottom). These images were redrawn from [41].

is induced in the pixel, the state of the pixel can be modeled adding the voltage source U_{break} to the circuit by closing S. Fig. 3.9(b) shows the time evolution of the current I_{D} in the diode, the potential across the quenching resistor U_{RQ} and U_{D} for this model. If the switch S is closed by the time t_0, the capacitor discharges almost only over R_{D} since $R_{\text{D}} << R_{\text{Q}}$. The time evolution of the discharge of C_{D} can be described by the time constant of the capacitor $\tau_{\text{D}} = R_{\text{D}}\text{C}_{\text{D}}$. During the discharge, no further signal can be detected in the pixel. The time $\tau_{\text{dead}} = t_1 - t_0$ is therefore called the dead time of the pixel. The current in the diode rises instantly up to $I_{\text{max}} \approx \frac{U_{\text{over}}}{R_{\text{D}}}$ and then drops due to the discharge of C_{D}. The current I_{RQ} in the external circuit (quenching resistor in series with diode) rises converging to the asymptotic value $I_{\text{latch}} \approx \frac{U_{\text{over}}}{R_{\text{D}}+R_{\text{Q}}}$. This causes the potential U_{RQ} to rise. Since $U_{\text{D}} + U_{\text{RQ}} = U_{\text{bias}}$ has to be fulfilled, the potential U_{D} drops and tends to U_{break} asymptotically. Small statistical fluctuations in U_{D} can cause the potential

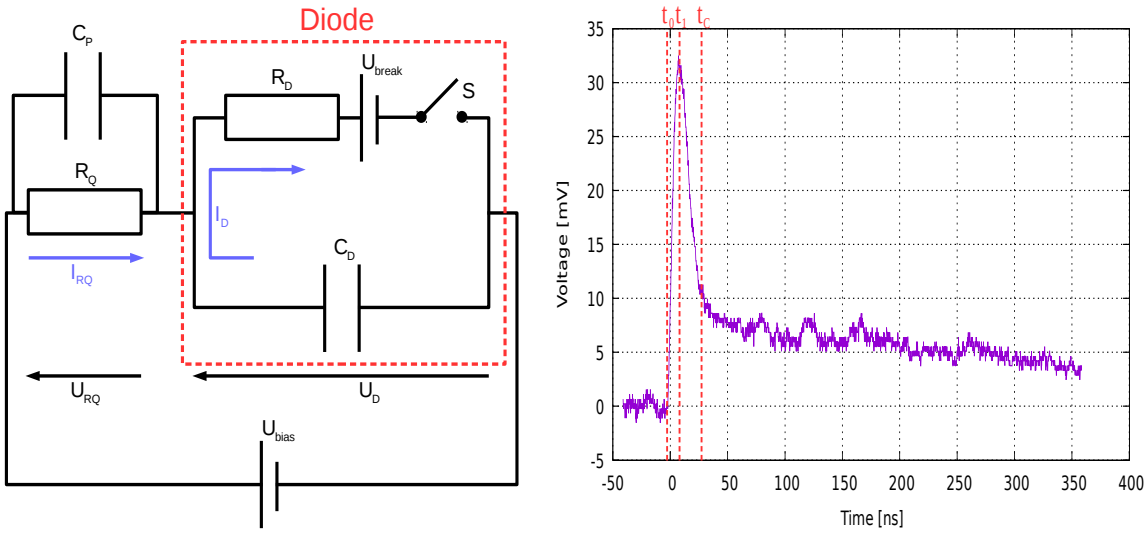

(a) (b)

Figure 3.10: (a) Equivalent circuit for a realistic pixel. Additionally to the circuit of an ideal pixel (see fig. 3.9) a parasitic capacitance C_P connected in parallel to the quenching resistor occurs. This image was redrawn from [41]. (b) Typical pulse signal of the investigated SiPM.

in the diode to drop below U_break. Since U_break is the minimum voltage that is required to induce an exponential charge multiplication in a pixel, the avalanche is stopped if $U_\mathrm{D} < U_\mathrm{break}$. As the current in the external circuit subsides with the time constant $\tau = R_\mathrm{Q} C_\mathrm{D}$, the quenching resistor determines the time, by which the avalanche is stopped. If R_Q is chosen too small, the current in the diode would damage the pixel [41].

The current I_RQ can be measured via an external resistor that is connected in series with the diode. The potential across this resistor is proportional to I_RQ and can be visualized on an oscilloscope. Fig. 3.10(b) shows a voltage signal of a SiPM recorded with an oscilloscope. Such a data set is further referred to as waveform. The x-axis outlines the time and the y-axis the signal voltage. At the time t_0 the signal starts to rise until it reaches its maximum value at the time t_1. The shape of the pulse after the maximum indicates an exponential reduction with two different time constants. A shorter one dominating from t_1 to t_C and a much larger one from t_C until the signal has completely subsided. These two edges indicate two different discharge processes. The larger one arises from the pixel capacitance C_D. The shorter one can be explained by adding a parasitic capacitance C_P in parallel to the quenching resistor. C_P arises from the fact that the poly-silicon quenching resistor lays on top of the junction area. Fig. 3.10(a) shows the equivalent circuit for a pixel with an additional parasitic capacitance connected in parallel to the quenching

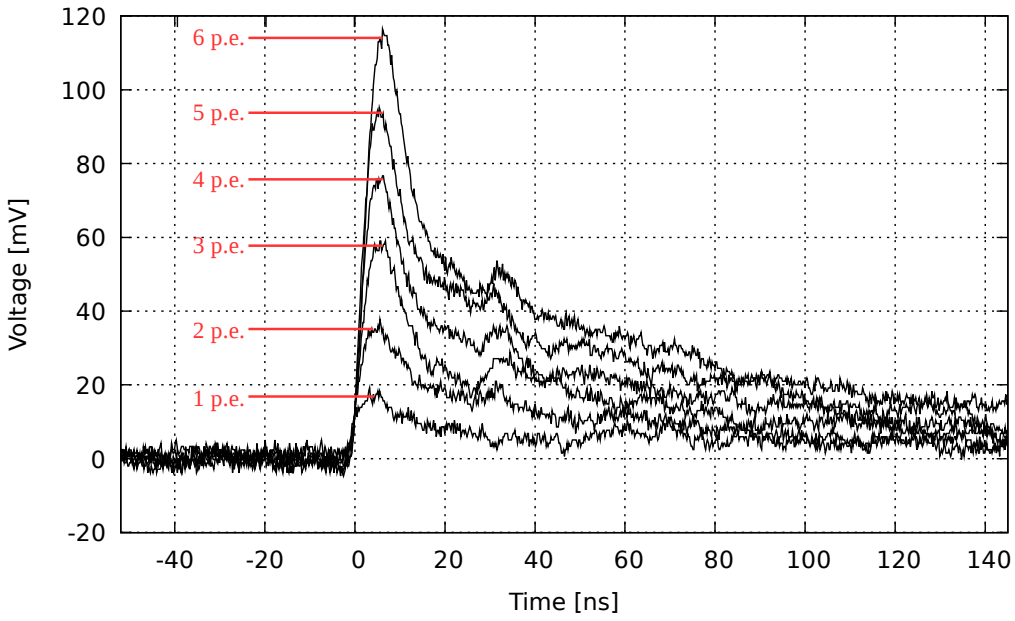

Figure 3.11: Discrete pulse signals from a SiPM. Each pulse arises from a quantified number of triggered avalanches.

resistor [41]. Typical times of the falling edges are in the region of 10 ns - 20 ns for the fast falling edge and about a μs until the slow edge has completely subsided.

Each pixel is only capable of yielding the information whether or not an avalanche has been induced. The current signal from the SiPM is linearly dependent on the number of pixels that induced an avalanche at the same time. This number is further referred to as photoelectron equivalent (p.e.). This leads to a discretization of the current signal of the SiPM. Therefore, the height of the pulse signals is discretized as well. Fig. 3.11 shows an example of this discretization for six pulse signals with different p.e. .

3.2.4 Characteristic Properties

Dark Count Rate

The dark count rate denotes the number of pulse signals per time that are recorded in the absence of any incident light. Those signals are induced by thermally generated charge carriers that are accelerated by the electric field and cause an avalanche in the depletion region. This signal is similar to the one caused by a photoelectron. It can, therefore, not be distinguished whether the initial charge carrier was generated thermally or induced by an incident photon.

This dark noise is a dominant background in every experiment where it is necessary to detect little amounts of light. Dark noise reduction can therefore make a significant difference on the accuracy of the measurement.

The probability for an electron to produce a dark noise signal is proportional to the number of lattice atoms in the semiconductor and, therefore, to the size of the pixel. Reducing the effective pixel area leads to a reduced dark count rate. On the other hand, with smaller pixels more top layer elements (like quenching resistors or trenches) that are not part of the sensitive area need to be installed thus, reducing the geometrical efficiency. Thermal movement of lattice atoms and electrons declines with temperature. Cooling the material makes it less likely for an electron to be released from the semiconductor material and induce an avalanche. Therefore, the dark count rate declines with lower temperatures [41]. Fig. 3.12(b) shows the dark count rate in dependence on the temperature for the KETEK PM3350 and an overvoltage of 20 % of the breakdown voltage. Typical dark count rates at room temperature are in order of a few 100 $\frac{\text{kHz}}{\text{mm}^2}$, whereas it drops to a few $\frac{\text{Hz}}{\text{mm}^2}$ at about $-100\,^{\circ}\text{C}$ [48]. The mean energy the electrons need to be released from the semiconductor material decreases with a higher electric field that is applied to the diode. Therefore, the probability for an electron to induce an avalanche increases with the overvoltage U_{over}. Fig. 3.12(a) shows the dark count rate in dependence on the overvoltage relative to the breakdown voltage for the KETEK PM3350.

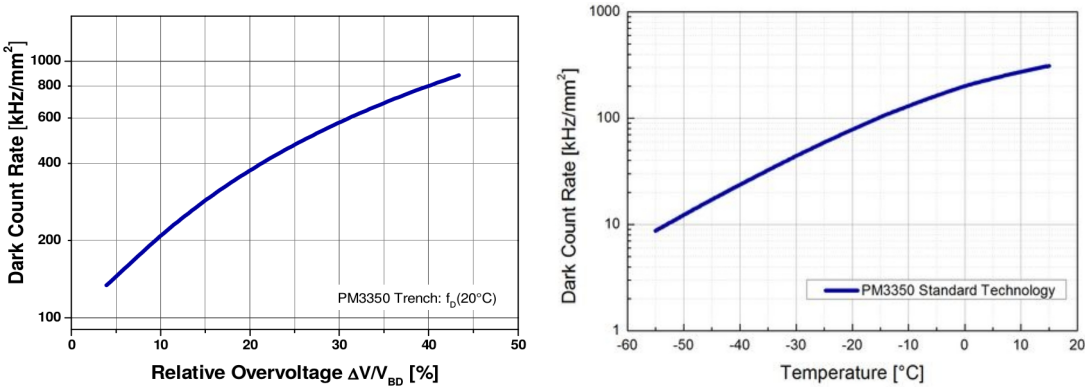

(a) (b)

Figure 3.12: (a) Dark count rate in dependence on the overvoltage for the KETEK PM3350 with trench technology [48]. (b) Dark count rate in dependence on the temperature for the KETEK PM3350 for an overvoltage of 20 % of the breakdown voltage. These images were taken from [49].

Crosstalk

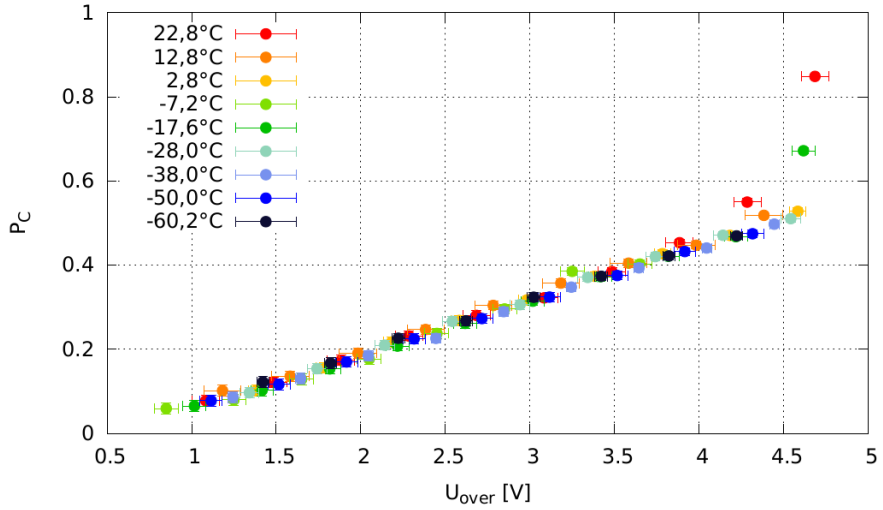

Figure 3.13: CT probability in dependence on the overvoltage for various temperatures. The data shows a linear dependence. The temperature does not seem to affect the CT probability. These measurements were done with a KETEK PM3375 SiPM [50].

Besides dark noise, crosstalk (CT) is also an intrinsic phenomenon that can cause pixels to generate signals without having detected an external photon. It is very unlikely that dark noise occurs in two pixels at the same time. The avalanche induced in one pixel, however, can trigger other pixels causing further avalanches. Since this is an intrinsic process, it happens in such a small time interval that the current signals coming from the primary and secondary triggered pixels occur at nearly the same time. This leads to pulse signals with p.e. higher one. Like dark noise, the probability that CT occurs is dependent on U_{over}. But unlike dark noise, CT is not temperature dependent. Fig. 3.13 shows several measurements for the probability that CT induced signals occur in dependence on the overvoltage for different temperatures. The CT probability does not vary with the temperature. These measurements were done by Judith Schneider as part of the EXO/nEXO - work group Erlangen [50].

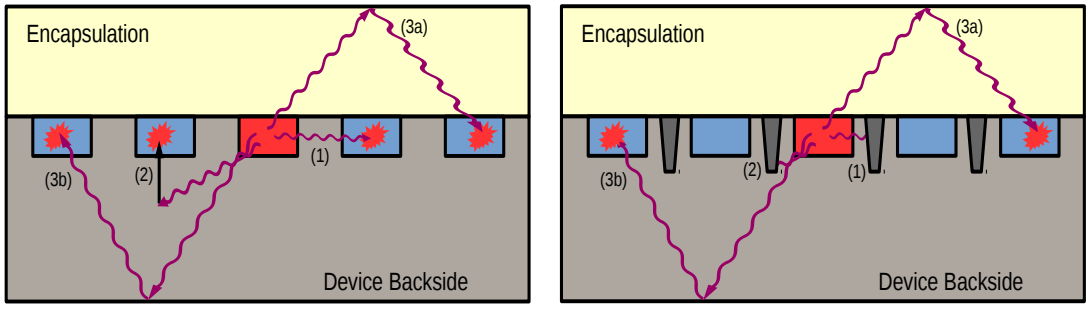

(a) (b)

Figure 3.14: Scheme of the main mechanisms causing CT in SiPMs without (a) and with (b) trench technology. IR photons can propagate into another pixel and cause further avalanches. This can happen either directly (1), or indirectly via reflection at the encapsulation (3a) or the device's backside (3b). Additionally, a charge carrier can be released in the intrinsic material (2) and drift into another pixel causing an avalanche. Mechanism (1),(2) and (3b) can be prevented by trenches. These images were redrawn from [51].

Fig. 3.14(a) shows a scheme of the dominant three processes causing so called optical crosstalk. If a pixel is triggered by either dark noise or an incoming photon, electrons in the avalanche can induce the emission of IR photons. Those IR photons can propagate through the semiconductor material into other pixels, releasing electrons and causing additional avalanches. This can happen in different ways (see fig. 3.14) [49]:

- The IR photon propagates directly into another pixel and releases an electron (1).
- The IR photon is reflected by e.g. the interface of the encapsulation on the SiPM and releases an electron in another pixel (3a).
- The IR photon is reflected by the device‘s backside and propagates into another pixel where it releases an electron (3b).

In addition, an IR photon can also release an electron in the intrinsic material. Due to the applied bias voltage, this electron can drift towards a proximate pixel causing an avalanche (see (2) in fig. 3.14(a)). CT can be reduced by the trench technology (fig. 3.14(b)). Trenches are barriers of highly absorbing materials, as for example tungsten between the pixels. Those barriers make it less likely that an IR photon propagates into other pixels and induces further avalanches. This way, the mechanisms (1), (2) and (3b) shown fig. 3.14 can be reduced.

After-Pulsing

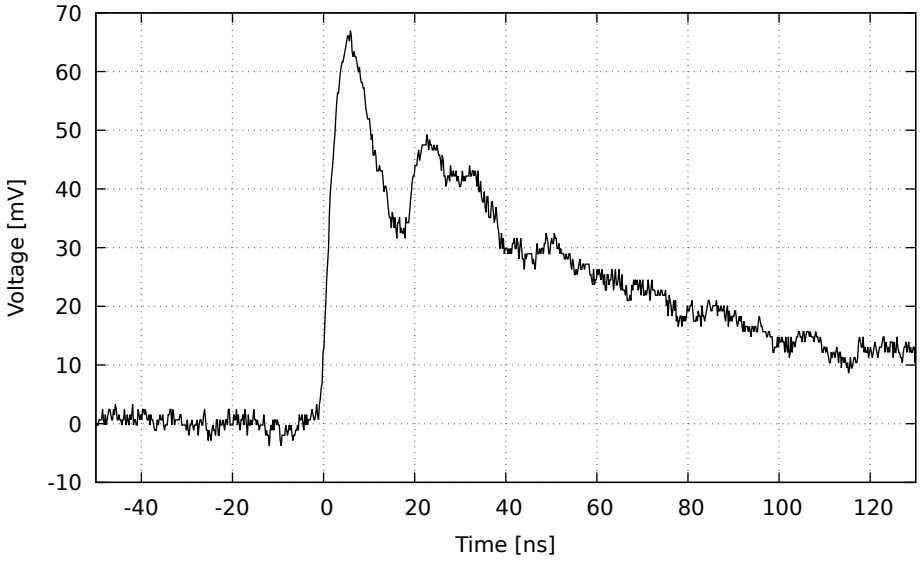

Figure 3.15: After-pulse signal that occurred about 20 ns after the initial pulse.

After an avalanche was induced in a pixel, a charge carrier can be trapped at an impurity atom in the semiconductor material. In this state, the trapped charge can be bound for a few ns and is subsequently released. This released charge can trigger a further avalanche in the pixel [52]. Since this usually happens a short time after the pixel was triggered in the first place, the capacitor formed by the pixel is not completely recharged yet. At this time, the electric field in the pixel is not as high as it is when the capacitor is fully charged. The charge that is released from the impurity atom causes less secondary charges in an avalanche and the overall charge signal is smaller [41]. Fig 3.15 shows an initial pulse signal followed by a smaller one. This second pulse is probably induced by after-pulsing. The after-pulses can also occur significantly later than the initial one. If the capacitor is fully recharged by then, it is not possible to distinguish an after-pulse signal from an initially triggered pulse. Therefore, it is very difficult to determine the contribution of after-pulsing to the number of measured signals.

After-pulsing basically depends on two parameters: On the one hand the applied bias voltage, since the number of charges in an avalanche is dependent on the applied electric field in the pixel. The probability for a charge carrier to be trapped at an impurity atom increases with the number of charges in an avalanche. On the other hand, it is dependent on the temperature. Lower temperatures lead to longer lifetimes of the bound state since thermal movement of the atoms in the semiconductor material influences the stability of the bound state.

Since an after-pulse signal cannot be distinguished from a signal that was induced by an external photon, low temperatures and low overvoltages can contribute to reduce after-pulsing.

Photon Detection Efficiency

The photon detection efficiency (PDE) is the ratio between the number of detected photons and the number of photons that impinged onto the detector. The PDE is defined as [53]:

$$PDE = QE(\lambda) \cdot P_{\text{trig}} \cdot \varepsilon_{\text{geo}} \quad , \tag{3.6}$$

where $QE(\lambda)$ is the quantum efficiency that depends on the wavelength λ of the incoming photon, P_{trig} the trigger probability and ε_{geo} the geometrical efficiency. QE is a measure for the probability that a photon creates an e-h pair and, therefore, a free photoelectron in the pixel. The probability for this to happen is wavelength dependent. Photon reflection at the surface of the SiPM is the most suppressing factor. To maximize the amount of light penetrating the top layer, an anti-reflective coating (ARC) is applied. This ARC is typically not transparent for VUV-light. QE of SiPMs with ARC is therefore close to zero in the VUV region. QE also rises with the temperature. The charge carriers in the pixel have a lower binding energy due to thermal movement and are, therefore, more likely to be released from the material. The geometrical efficiency is the ratio between

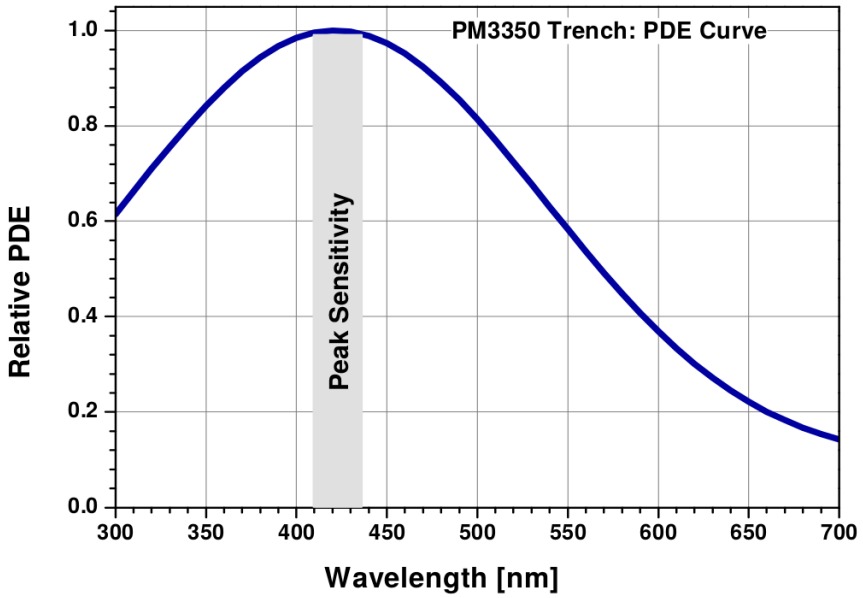

Figure 3.16: Relative PDE of the Ketek PM3350 SiPM with trench technology in dependence on the wavelength. The peak sensitivity is at about 420 nm. This Image was taken from [51].

the effective pixel area A_{pixel} and the area A_{SiPM} of the SiPM. A photon can only be detected, if it impinges onto the surface of a pixel. The bias electrodes and quenching resistors are mounted between the pixels. Both components acquire space on the surface and decrease the available area for A_{pixel}. Not every electron that is released from the semiconductor material reaches the high field region. It can also recombine with an e-h before it induces an avalanche. The probability that a photoelectron creates an avalanche in a pixel is called trigger probability. A higher electric field makes it more likely that a signal is induced. $P_{trig}(U_{over})$ is, therefore, dependent on the overvoltage [53].

Fig. 3.16 shows the PDE relative to its highest value for the KETEK PM3350 SiPM. The SiPM has a maximum PDE of $> 40\,\%$ at a wavelength of about 420 nm [51].

3.2.5 Required Limits for the nEXO Experiment

The SiPMs that will be used in the nEXO experiment are chosen by limits on some characteristics. The requirements need to be fulfilled to achieve the aim for an energy resolution of 1 % at the Q-value of 2.458 MeV. In the following, some of the main requirements are listed [35]:

- It is planed to collect 10 % of the scintillation photons produced in the liquid xenon. According to simulations, this is achievable if the utilized SiPMs have a PDE of at least 15 % at a wavelength of 175 nm-178 nm.
- The number of correlated avalanches, caused by CT and after-pulses, needs to be lower than 20 % at the voltage of operation.
- Dark noise needs to be lower than $50\,\frac{\mathrm{Hz}}{\mathrm{mm}^2}$ at a temperature of $-100\,^{\circ}\mathrm{C}$.
- The SiPM material needs to have a radio purity of about $10\,\frac{\mu\mathrm{Bq}}{\mathrm{kg}}$.
- To decrease the number of required feedthroughs, an individual SiPM needs to have a size of at least $1 \times 1\,\mathrm{cm}^2$.

3.3 Xenon as Detector Material

In the nEXO experiment xenon is used as decay source as well as detector material. Depositing energy in xenon yields a scintillation light signal as well as an ionization signal. Those two pieces of information are used to calculate the amount of energy that is deposited by the two decay electrons in xenon. Fig. 3.17 lists the relevant processes that lead to the scintillation and ionization signal.

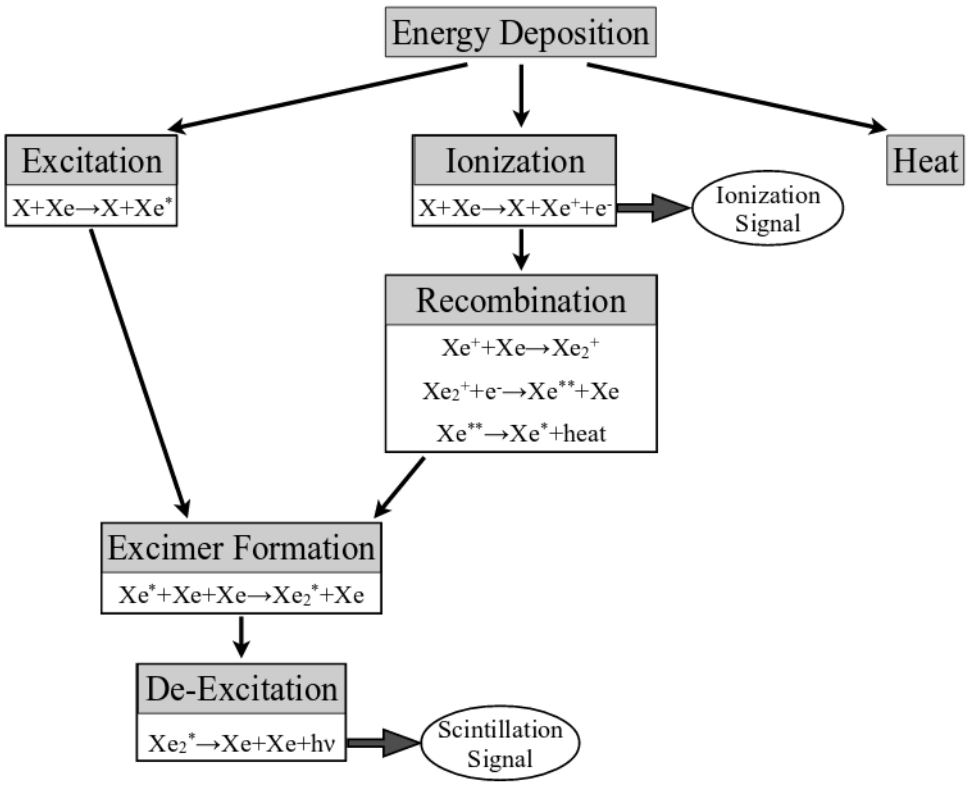

Figure 3.17: Diagram of the different processes that lead to an ionization and a scintillation signal if an incident particle X propagates through the xenon. This image was taken from [54].

An ionizing particle X, as e.g. an α-particle, can deposit energy in xenon in three ways [55]:

- By excitation of a single xenon atom Xe^* that leads to the formation of an excited diatomic molecule (excimer) Xe_2^*, which then decays to a de-excited atom and a scintillation photon. This cascade process happens through collisions of the xenon atoms and molecules with each other:

$$\begin{aligned} \alpha + \mathrm{Xe} &\rightarrow \alpha + \mathrm{Xe}^* \\ \mathrm{Xe}^* + \mathrm{Xe} + \mathrm{Xe} &\rightarrow \mathrm{Xe} + \mathrm{Xe}_2^* \\ \mathrm{Xe}_2^* &\rightarrow \mathrm{Xe} + \mathrm{Xe} + h\nu \end{aligned}$$

- By ionization of a single xenon atom. An electric field can be applied between an anode and a cathode in the xenon. The free electrons drift towards the anode and can be read out as a charge signal. The ionized Xe^+ atom can form an ionized diatomic molecule (dimer) Xe_2^+ together with a neutral xenon atom. This dimer may recombine with an electron producing a neutral xenon atom and an excited xenon atom Xe^{**}.

The Xe^{**} may partially de-excite depositing heat in the xenon and leaving an excited xenon atom that can take part in the excimer formation process again:

$$\begin{aligned} \alpha + Xe &\rightarrow \alpha + e^- + Xe^+ \\ Xe^+ + Xe &\rightarrow Xe_2^+ \\ Xe_2^+ + e^- &\rightarrow Xe + Xe^{**} \\ Xe^{**} &\rightarrow Xe^* + \text{heat} \end{aligned}$$

- By depositing thermal energy.

The scintillation yield as well as the wavelength of the emitted light is essential for the choice of the detector. Fig. 3.18 shows the scintillation light spectrum of gaseous Xe relative to its highest value. The spectrum ranges from about 160 nm to 190 nm and has its peak value at a wavelength of about $\lambda_{max} = 175$ nm.

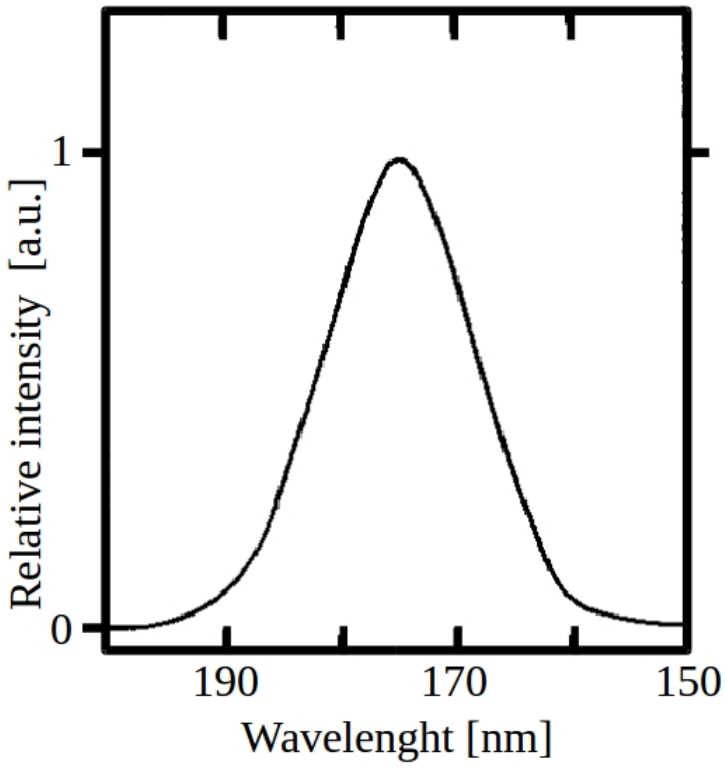

Figure 3.18: Scintillation light spectrum of gaseous xenon relative to its highest value. The maximum value is at about 175 nm. This image was taken from [56].

3.4 Operation principle of a Wavelength Shifter

The uncoated version of the detector used in the experiments in this thesis is not sensitive to xenon scintillation light. Fig. 3.16 shows the wavelength dependent relative PDE. The spectral response ranges from a wavelength of 300 nm to 800 nm. Neither absolute nor relative values of this SiPMs PDE are known for wavelengths of scintillation light coming from xenon. In addition, the SiPM is encapsulated in epoxy that is transparent for visible light. It is however unlikely that this synthetic material is transparent for VUV light. To overcome this problem, the SiPM used for this thesis is coated with 1-Naphthalenecarboxaldehyde, 2-hydroxy-[(2-hydroxy-1-naphthalenyl)methylene]hydrazone(9CI) (further referred to as *Lumogen*®) [42], a wavelength shifter that converges VUV light into light in the visible region. The SiPM was coated by *EURECA Messtechnik GMBH* [58]. Fig. 3.19 shows the Jablonski energy level diagram for an organic wavelength shifter. A photon is absorbed by an electron from the ground state S_0. This electron is excited to one of the vibrational levels of the first excited state S_1. The electron de-excites to the lowest vibrational level of S_1. This de-excitation usually happens under the emission of an IR photon or by deposition of thermal energy in the material. The electron de-excites further to one of the vibrational levels of S_0 under the emission of a fluorescence photon [57].

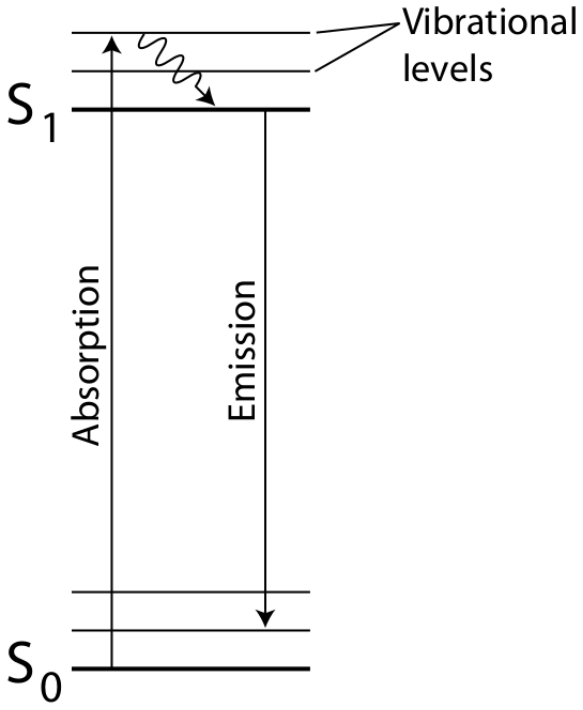

Figure 3.19: Energy levels and the corresponding processes during absorption and emission for an organic wavelength shifter. This image was taken from [57].

Fig. 3.20 shows the emission spectrum of *Lumogen*®. The local maxima at about 520 nm and 570 nm arise from the photon energy that is dependent on the potential of the different vibrational levels of the ground state S_0 with respect the energy level S_1. Values for relative or absolute emission below a wavelength of 300 nm are not known. The emission spectrum, however, has its highest efficiency in a wavelength interval between 500 nm and 600 nm where the PDE of the used SiPM is about 24% to 32%. The conversion cross section of *Lumogen*® at VUV wavelengths can be derived from the relative spectrum and the measured photon fluence on the SiPM (see sec. 6.8).

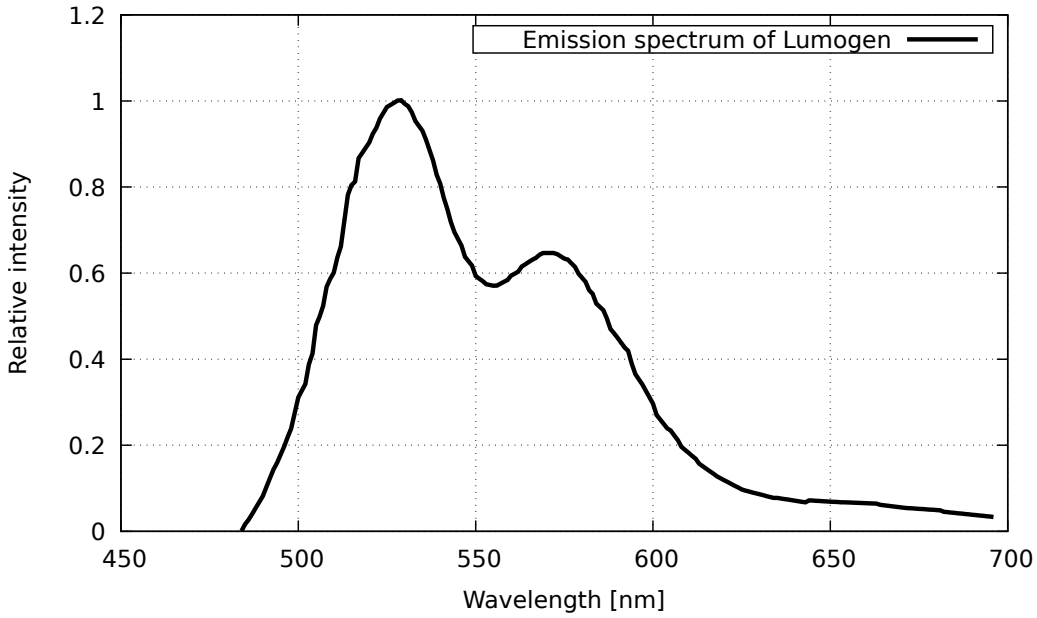

Figure 3.20: Fluorescence emission spectrum of *Lumogen*® relative to its highest value. The local maxima arise from the different vibrational levels in the energy level S_0. This image was replotted from [42].

4 The Experimental Setup

This chapter introduces the experimental setup that was used for the measurements in this thesis. Hardware and operation principle are introduced. The methods used to stabilize and control the temperature are explained. The data acquiring system, the readout electronics of the detectors and the utilized devices are presented. The measuring procedure is outlined.

4.1 Setup

4.1.1 The Cryostat

Fig. 4.1 shows a scheme (left) and a CAD 3/4-cross section view (right) of the cryostat containing the SiPM test setup (further referred to as xenon cell, see sec. 4.1.3). The xenon cell is placed in the inner vessel (3) that is connected to a gas inlet system via a steel pipe (1). Wiring for the electronics is also lead through this pipe. The inner vessel (IV) is thermally connected to a copper rod (4) that functions as cooling finger. The heat regulation system is attached to the rod (see sec. 4.2). The Gas supply system, the IV and the copper rod are placed in the outer vessel (2) that is evacuated for thermal insulation. The copper rod is thermally connected to the bottom of the outer vessel (OV). The bottom is thermally connected to an aluminum rod (5) from the outside. This aluminum rod is placed in a dewar filled with liquid nitrogen (LN), thus cooling the IV. All thermal junctions are realized via a thin layer of indium to increase the contact surface. Additionally, the IV was wrapped in IR reflecting foil to reduce heat contribution from thermal radiation.

A shielded feedthrough is used to lead the signals of both devices out of the IV. Two separate feedthroughs are used for the supply voltages. The temperature sensors as well as the supply voltage for the signal amplification of the SiPM are lead through a multi-pin feedthrough.

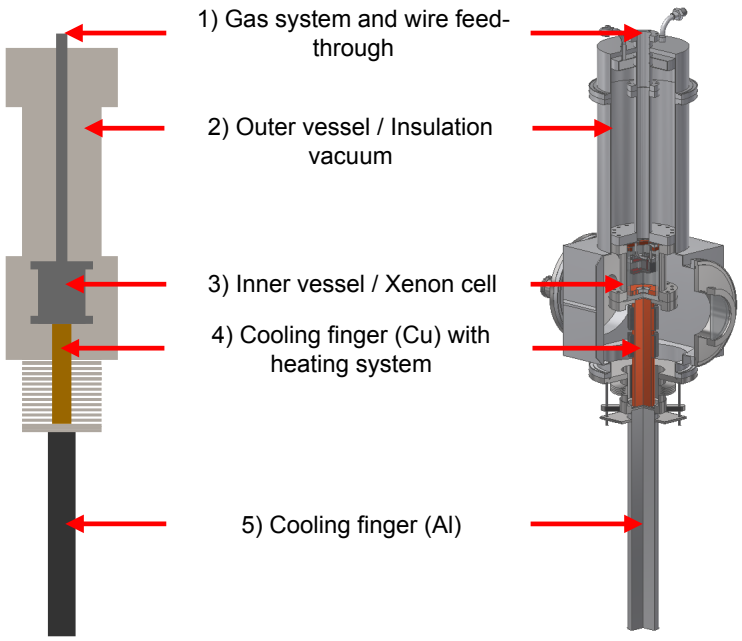

Figure 4.1: Cryostat that contains the SiPM test setup (xenon cell). Gas inlet and electronics (1) are fed through a steel pipe into an inner vessel (3) that contains the xenon cell. An evacuated outer vessel (2) thermally insulates the inner vessel. The inner vessel is cooled via a cooling finger, a copper rod (4) on the inside of the outer vessel and an aluminum rod (5) that is placed in a dewar with liquid nitrogen on the outside of the outer vessel.

4.1.2 Gas Inlet and Vacuum System

The vacuum and gas inlet system consists of two separate and uncoupled tubings. The first one only serves the purpose of evacuating the OV, thus thermally insulating the inner vessel (IV). The second one is used to evacuate the IV and fill it with xenon gas. Fig. 4.2 shows a scheme of both systems. The tube system for the OV (gray) consists of a rotary vane pump P_0 that is connected to the OV, a valve V_0 between the pump and the OV and an analogous pressure gauge M_0. An electric feedthrough is integrated on the top side of the OV (B) to connect a temperature sensor and the heat control system to the temperature regulation system. To prevent the deposition of moisture onto cold surfaces, the OV was evacuated before the system was cooled down. During the experiments the insulation vacuum was stable around 10^{-3} mbar.

The tube system for the IV (see fig. 4.2 black) consists of a vacuum system on the one side and a gas inlet system on the other. The vacuum system consists of a pre-pump P_1 and a turbomolecular pump P_2 that are both connected in series with the IV via a valve V_1. Both pumps are pivoted without oil to keep the

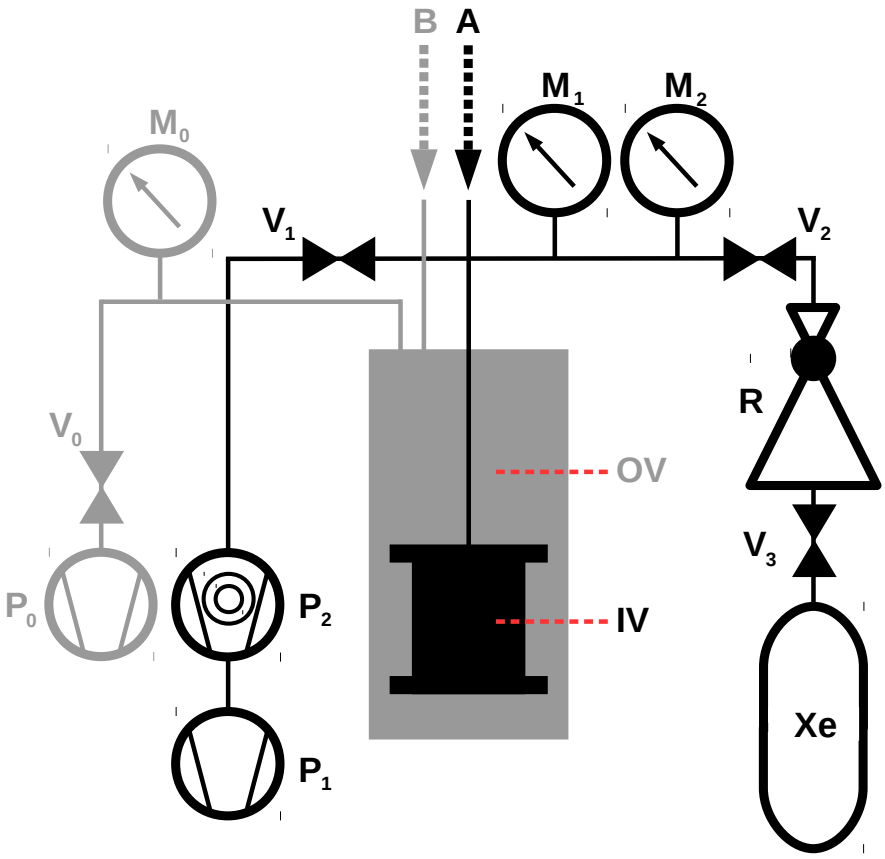

Figure 4.2: Scheme of the vacuum insulation system for the OV (gray) and the vacuum and gas inlet system for the IV (black).

IV clean. The pressure in the IV is measured by an analogous M_1 and a digital filament M_2 pressure gauge. The gas inlet system consists of a xenon gas bottle that is connected to a pressure regulator R via a valve V_3. The pressure regulator is connected to the IV via a valve V_2. All tubings are being led through the topside of the OV (A) including an access to wire electronics inside the xenon cell.

The IV is evacuated before it is filled with xenon. Until the xenon is led into the IV, the pressure is measured with the filament pressure gauge. With V_1 opened and V_2 closed the pre-pump P_1 evacuates the IV through the pump P_2. The turbomolecular pump is switched on after the pressure in the IV has fallen below 10^{-2} mbar. This procedure is necessary to prevent the turbomolecular pump from being damaged. Both pumps evacuate the IV to a pressure of about 10^{-6} mbar. The low pressure is necessary to ensure the purity of the xenon gas. The required pressure can roughly be estimated assuming an ideal gas. The particle density at a pressure of 1.1 bar is calculated via the ideal gas equation to be about $2.72 \cdot 10^{22}\,\mathrm{l}^{-1}$. The xenon gas is of 99.996 % purity and contains, therefore, about 0.004 % atoms

and molecules other than xenon. The density of impurity particles is, therefore, $1.09 \cdot 10^{18}\,\mathrm{l}^{-1}$. Based on this number, the minimum pressure to ensure a lower density of impurity particles can be calculated via the ideal gas equation to be about $4 \cdot 10^{-2}\,\mathrm{mbar}$.

After the desired pressure in the IV is reached, V_1 is closed and V_3 is opened. The pressure regulator is adjusted to limit the pressure in the IV to 1.1 bar. After that, V_2 is opened to fill the IV with xenon gas. From this time on, the pressure is measured with the analogous pressure gauge, since the filament pressure sensor is not capable of measuring xenon gas at higher pressures than about 1 mbar. The system is cooled down after the IV is filled with xenon gas. This way, a sudden rise in temperature, caused by a malfunction of the heating system or a low LN level, cannot lead to an uncontrolled rise of the pressure, since the gas is filled in the IV at room temperature.

4.1.3 Xenon Cell

Fig. 4.3 shows a scheme (left) of a CAD 1/2-cross section view of the xenon cell and an associated picture of the detectors (right). The xenon cell consists of a copper cup (7) that is screwed to the bottom of the IV to ensure thermal

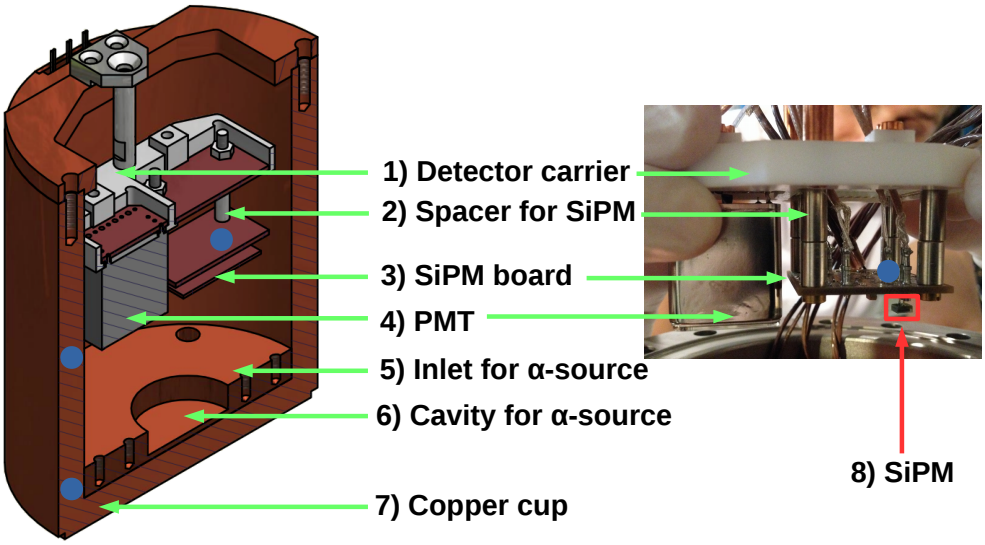

Figure 4.3: CAD 1/2-cross section view of the xenon cell (left) and a picture of the carrier (1) holding the detectors in place (right). The SiPM readout board (3) is elevated so that the SiPM (8) is on an equivalent height with the PMT (4) using spacer (2). The whole setup is placed in a copper cup (7) to distribute the temperature homogeneously in the cell. A copper inlet (5) with a cavity (6) is screwed to the bottom to hold an α-source in place. Blue dots mark positions where temperature sensors are placed.

conduction. An inlet for an α-source (5) is screwed to the bottom of the copper cup. The α-source is placed in a cavity (6) centered at the bottom. The α-source itself is embedded in an aluminum socket. The detectors are mounted to a carrier (1) made of polytetrafluoroethylene (PTFE) that faces from the top side into the copper cup. The PMT (4) as well as the SiPM board (3) are mounted to PTFE carrier. Spacers (2) between the SiPM board and the PTFE carrier align the detector surfaces to the same level above the α-source. The blue dots mark positions where a temperature sensor is placed. Since an indium layer between the copper cup and the IV impurifies the xenon, the copper cup is directly screwed to the bottom of the IV for thermal conduction. The carrier, the cables and most of the amplification and readout electronics consist of materials that cannot impurify the xenon. Those materials were chosen with respect to two criteria: On the one hand, the materials should not dissolve in gaseous xenon. On the other hand, no material should evaporate under low pressure. All components that were implemented in the xenon cell were cleaned with ultra pure ethanol before the whole setup was assembled.

4.1.4 Charge Readout Electronics

Both devices are mounted in the xenon cell together with charge readout boards. Due to the high capacitance of long cables and the rather small signal coming from the SiPM, the signal needs to be amplified before it is measured with the oscilloscope. The unamplified signal would acquire so much noise that a later amplification would degrade the signal-to-noise ratio significantly. Fig. 4.4 shows the circuit of the readout board that is used to amplify the signal of the SiPM. It contains several analog high-pass and low-pass filters to cancel out noise and prevent disturbing signals to interfere with the signal coming from the SiPM. These filters are not discussed in detail. In the following, only the basic parts and the operation principle of the circuit board are explained.

The red dashed line encircles the part of the circuit where the bias voltage is applied to the anode of the SiPM. The SiPM is terminated with $50\,\Omega$ to ground. The cathode is connected to the first of two operational amplifiers (OP) (blue dashed line, left). It amplifies the signal and works as an active low-pass filter. The amplified signal is transmitted to the second OP (blue dashed line, right), where the signal is amplified and filtered a second time. The OPs both need -5 V (black dashed line downside) and +5 V (black dashed line upside) as supply voltage. The output signal has a $50\,\Omega$ termination in parallel (green dashed line).

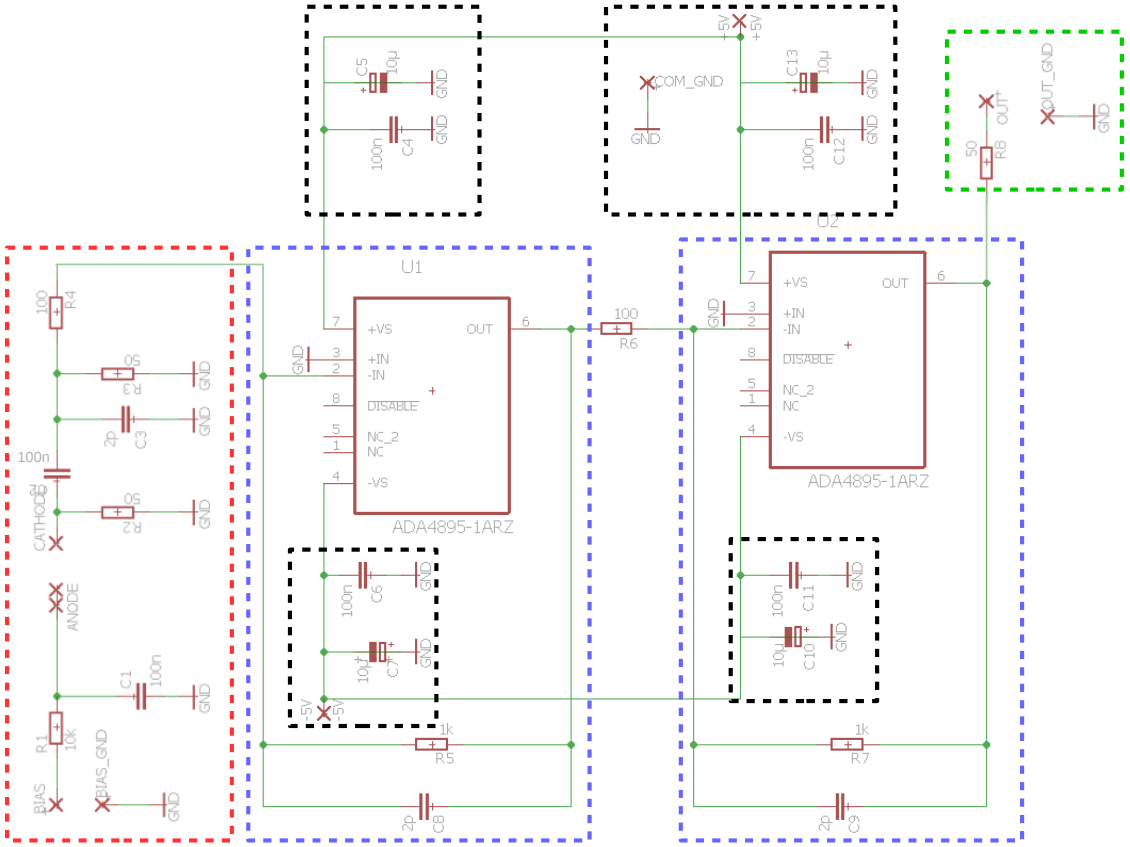

Figure 4.4: Readout circuit of the used SiPM. The bias voltage is applied between ground and the anode of the SiPM (red encircled). The SiPMs cathode is connected to the input of the first OP (blue encircled left). The signal is further amplified a second time by the second OP (blue encircled right). The OPs are supplied with +5 V (black encircled upside) and −5 V (black encircled downside). The output signal (green encircled) is terminated with a 50 Ω resistor. This circuit was design by Ako Jamil as part of the EXO/nEXO - work group Erlangen.

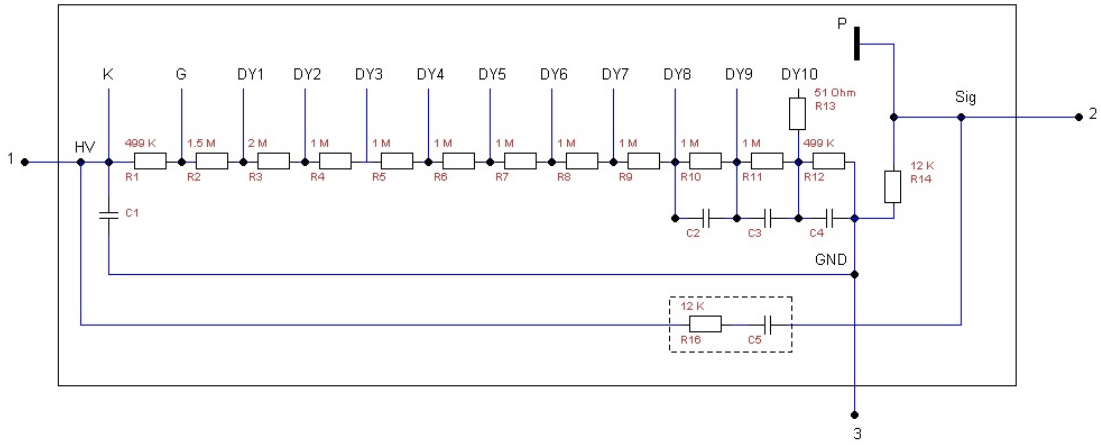

Figure 4.5: Circuit of the PMT readout board. Cathode (K), electron focusing grid (G), dynodes (DY) and anode (P) are connected via a voltage divider. The numbers denote the pin contacts for the HV input (1), the connection to ground (3) and the signal output (2).

The readout electronics of the PMT does not contain amplification. The charge signal from the PMT is directly transmitted to the oscilloscope. Fig. 4.5 shows the circuit of the PMT readout board. It consists basically of a voltage divider, that distributes the voltages over photocathode (k), the dynodes (DY), the electron focusing system (G) and anode (P) as it is described in the data sheet [39]. The numbers denote the pin contacts on the board for the high voltage (HV) input (1), the connection to ground (3) and the signal (Sig) output (2).

4.2 Temperature Regulation System

The aluminum cooling finger is placed in a dewar filled with LN. The xenon cell is thermally conducted to the aluminum cooling finger via the copper rod in the OV. The heating system that is used to regulate the temperature is attached to the copper rod. Fig. 4.6(right) shows an image of the top side of the copper rod. The heating system consists of 2 times 8 ohmic resistors connected in parallel to each other and wrapped around the copper rod. The total resistance of the upper resistor circuit R_1 (blue box) is 30 Ω and the one of the lower circuit R_2 (red box) is 15 Ω. While operating, a voltage $U_1 = 40\,\mathrm{V}$ is applied to R_1 and a voltage $U_2 = 20\,\mathrm{V}$ to R_2 generating a heating power of $P_1 = 53\,\mathrm{W}$ and $P_2 = 27\,\mathrm{W}$. A temperature sensor (white circle) is attached to the copper rod. The sensor is wrapped in an indium shell and pressed into a cavity in the rod to ensure thermal conduction. The temperature signal is read out by an analog-to-digital converter via a PC. The measured temperature value at the copper rod is compared to a nominal one. If the measured value is lower than the nominal one, a 5 V DC signal is given out via a digital-to-analog converter (DAC) to a circuit that switches on the heating system. This circuit is shown in Fig. 4.6 (left). An open switch S denotes no incoming signal. In this case, the measured temperature value is higher than the nominal one. If the measured temperature drops under the nominal one, the switch is closed and a voltage $U_s = 5\,\mathrm{V}$ is applied to the circuit. The maximum current provided by the used DAC box is 10 mA.

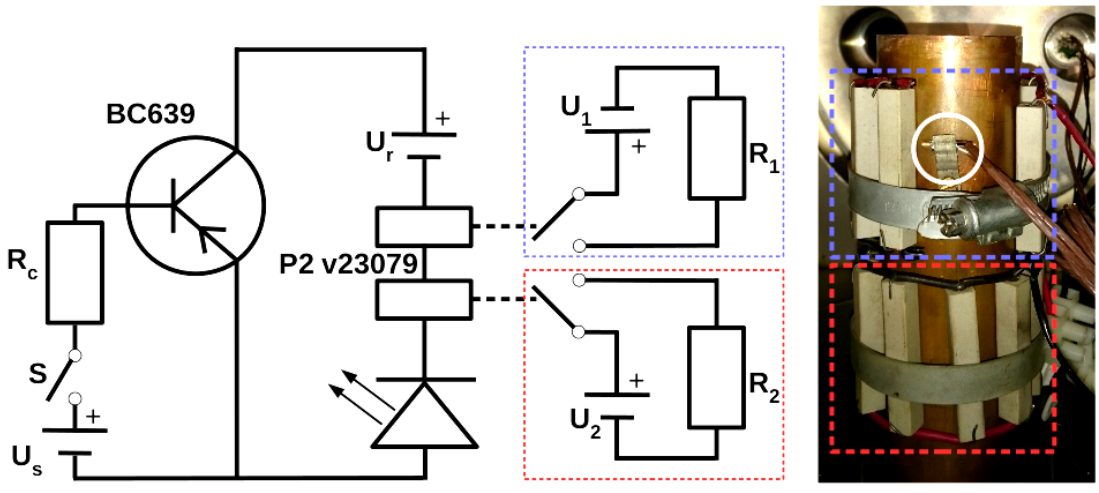

Figure 4.6: Temperature control circuit (left). Image of the heating system (right). The heating system consists of 2 times 8 resistors that are connected in parallel to each other. The supply voltages are triggered by the temperature control circuit. The temperature is measured at the copper rod (white circle). The temperature information is read out by a PC that triggers the switch S in the temperature control circuit.

The available relay cannot be triggered with this low current. Therefore, a transistor switch consisting of a *BC639* transistor and a resistor R_c to limit the current in the transistor is implemented. If S is closed, the transistor connects an additional voltage source U_r in series to the relay. A blue LED is connected in series with the relay to give a physical signal if the relay is closed. Both resistor circuits of the heating system are triggered by the relay giving rise to the temperature at the copper rod.

Due to the 1-bit logic of the control system, an oscillation caused by thermal hysteresis occurs. Fig. 4.7 shows a test measurement of both resistor circuits. The nominal temperature value was set to $T_{nom} = -109\,C^\circ$. Until $t_1 \approx 11.5\,min$ only the less powerful resistor circuit R_2 was connected (U_1 was manually set to zero). From t_1 to $t_2 \approx 43\,min$ both resistor circuits were connected and from t_2 on only resistor circuit R_1. As expected, the mean value of the oscillating temperature rises with the power of the heating system. The frequency of the oscillation is about 60 s. The mean peak-to-peak amplitude is about $0.5\,C^\circ$ where the maximum difference between the measured and the nominal temperature value is about $0.4\,C^\circ$. This measurement was done with an evacuated IV and without copper cup. The additional mass of the copper cup has a major impact on the frequency of the oscillation but not on the amplitude.

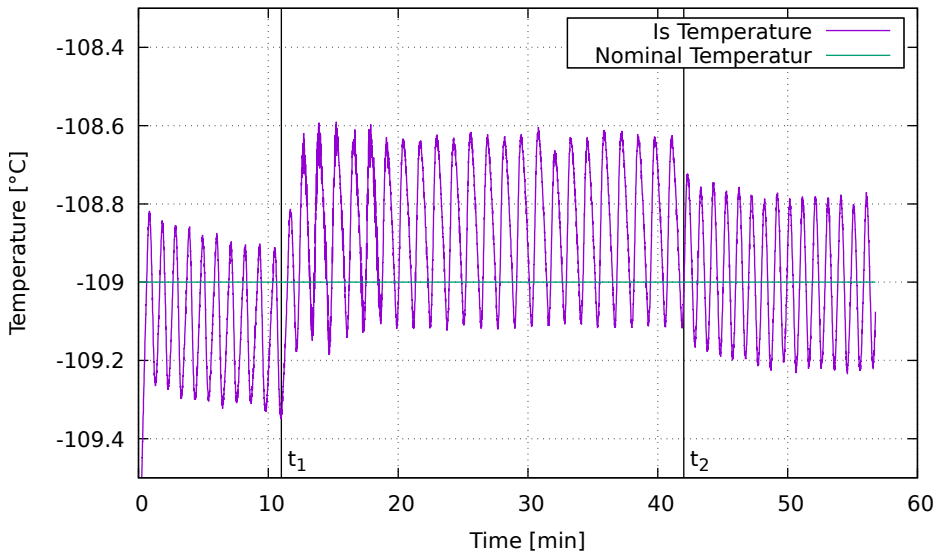

Figure 4.7: Temperature measured at the copper rod. Until the time t_1 only the resistor circuit R_2 is used to regulate the temperature, until t_2 both R_1 and R_2 are used and from that on, only R_1. The oscillation around the nominal temperature value arises from the 1-bit control logic.

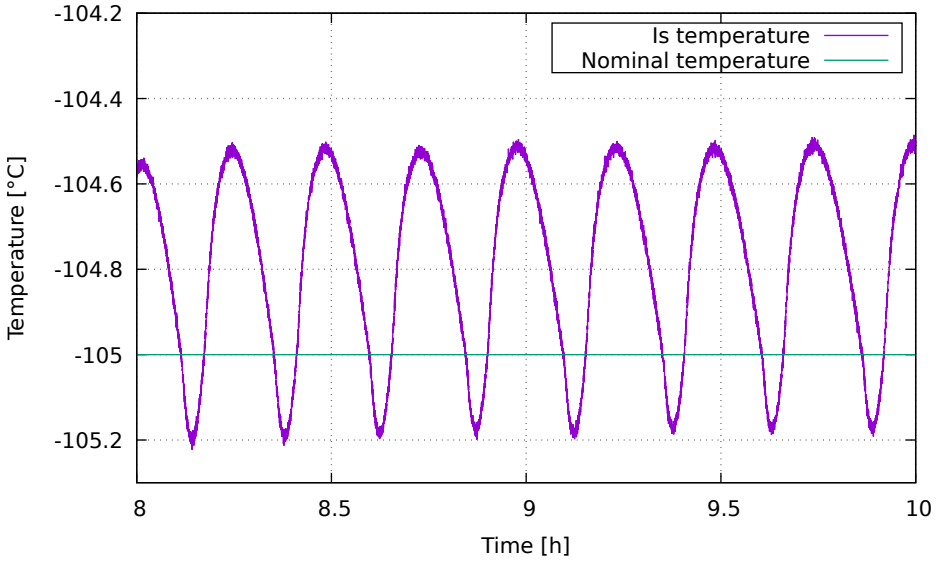

Figure 4.8: Temperature measured at the copper rod with the copper cup placed inside the IV under a helium atmosphere of 1.4 bar. The oscillation arises from the 1-bit logic of the temperature regulation system.

Fig. 4.8 shows a temperature measurement including the copper cup and a helium atmosphere at a pressure of 1.4 bar. The nominal temperature value was set to −105 °C. The LN dewar was constantly refilled during this measurement in order to prevent temperature deviations due to varying a LN level. Both resistor circuits of the heating system were active. The oscillation frequency is about 15 times larger than without the copper cup. The bigger mass serves as thermal reservoir causing a higher hysteresis and, therefore, a lower frequency in the temperature oscillation. This frequency, as well as the amplitude of the temperature oscillation, depends on the absolute temperature of the system. The cooling power at the copper rod rises with higher temperatures. Therefore, the effective heating power decreases. The cooling power at the copper rod could not be estimated with sufficient accuracy, since it is dependent on the filling state of the LN dewar and the gas pressure in the xenon cell. With an evacuated xenon cell and a fully filled dewar, the temperature converges at about $-80\,\mathrm{C}^\circ$ with both heating systems constantly running. At this point, the cooling power P_{cool} is equal to the heating power $P_{\mathrm{heat}} = P_1 + P_2 = 80\,\mathrm{W}$. As seen in fig. 4.3 temperature sensors are placed in the xenon cell. Fig. 4.9 shows the time evolution of the temperature that was measured at the bottom (blue) and the middle (green) of the xenon cell, as well as on the SiPM readout board (purple) and at the copper rod (yellow). By the time t_{h}, the nominal value for the temperature was set to $T_{\mathrm{nom}} = -105\,\mathrm{C}^\circ$. The temperature of the copper rod rises instantly, whereas the other temperatures keep falling for about 6 min due to the thermal hysteresis of the system.

After that, the temperatures rise until they saturate at higher values. This measurement was taken with the copper cup placed inside and the xenon cell filled with gaseous helium at a pressure of 1.4 bar. The helium atmosphere filled the IV and the steel pipe that reaches to the gas inlet system. This causes thermal convection between the xenon cell and the topside of the cryostat. That and the mass of the copper cup lead to thermal inertia causing the temperature at the SiPM readout board to adapt very slowly. The temperature at the SiPM readout board saturated after 4 - 6 hours. The difference between the temperature at the copper rod and the temperature in the xenon cell can be explained by the thermal contribution coming from the steel pipe and the helium gas. The helium atmosphere and the IV that is cooled from the bottom side warms up towards the topside of the cryostat. The heat contribution from the helium gas mainly causes the difference in temperature between the SiPM readout board and the copper cup.

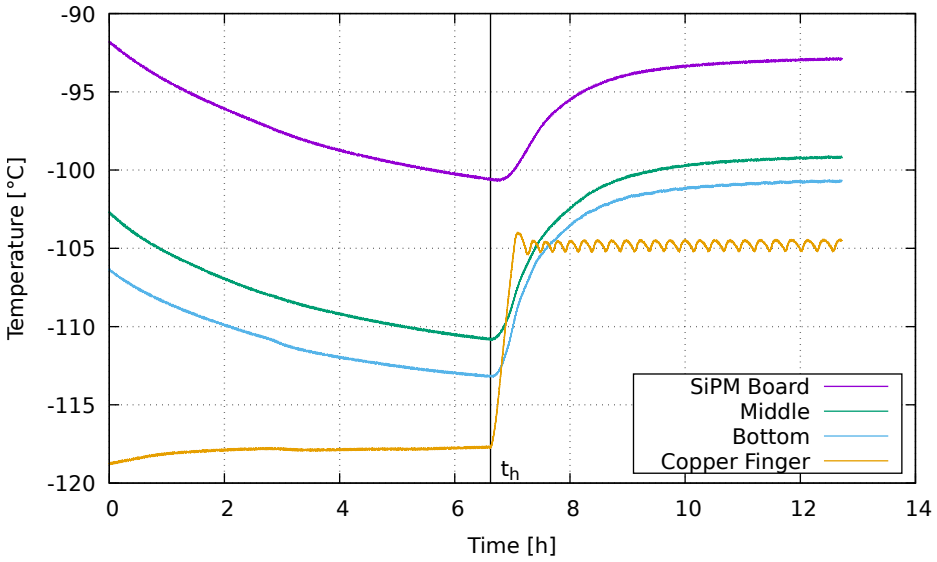

Figure 4.9: Measured temperature distributed in the setup. The temperatures are measured (from top to bottom): At the SiPM readout board, at middle height of the copper cup, at the bottom of the copper cup, at the copper bolt. t_h denotes the time when the heating system is switched on.

4.3 Utilized Devices

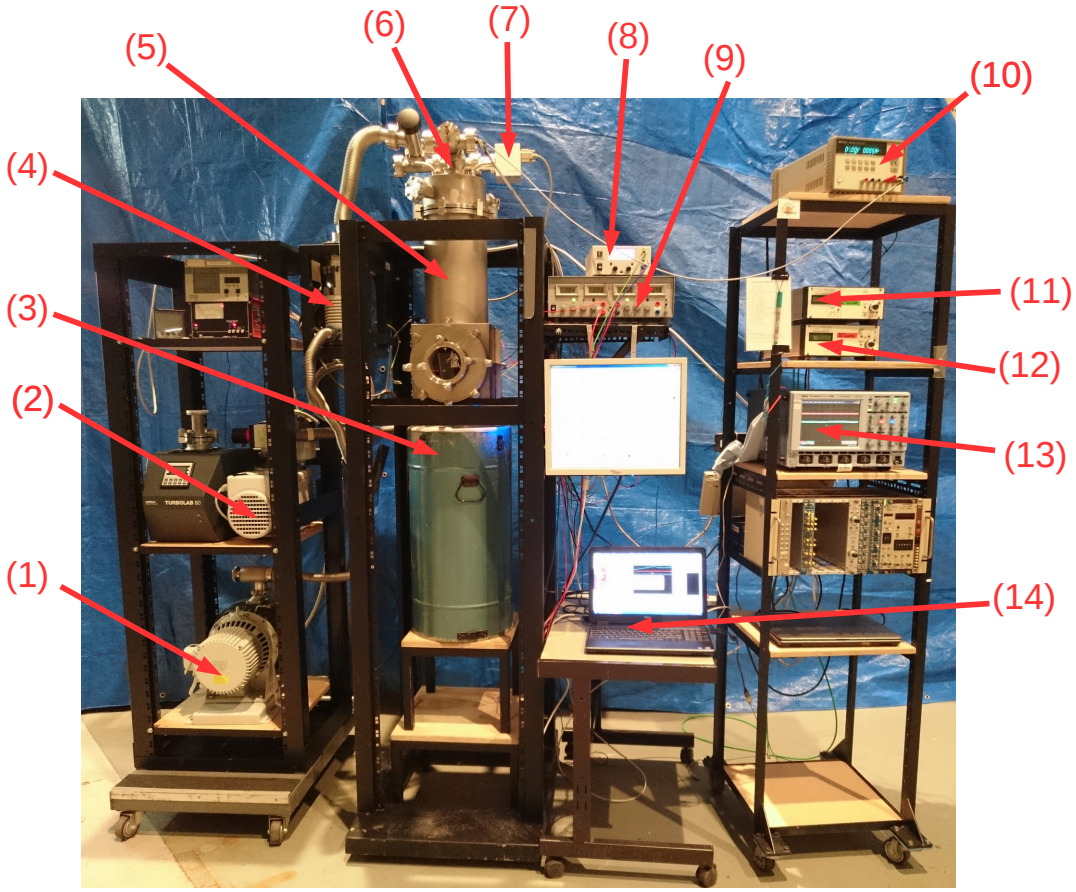

Figure 4.10: Experimental setup: Rotary vane pump as pre-pump (1) and a turbomolecular pump (4) for the IV. Pump for insulation vacuum (2) in the OV (5). Liquid nitrogen dewar (3). Gas inlet, vacuum connection and electric feedthrough (6). Filament pressure gauge (7). Power supply for resistor circuit R_2 (8) of the heating system. Power supply for the relay and resistor circuit R_1 (9) of the heating system. Power supply for the OPs (10). Power supply for the bias voltage of the SiPM (11). High voltage power supply for the PMT (12). Oscilloscope (13). Measuring PC (14).

Fig. 4.10 shows an image of the whole setup. The pre-pump (1) is an oil-free rotary vane pump *EDWARDS GVSP30 Scroll Pump* [59] that is used in combination with a *Pfeiffer TPH180* [60] turbomolecular pump (4) for the vacuum in the IV. The pump (2) for the insulation vacuum (connected to a *Leybold-Heraeus Combitron CM 330* pressure gauge) in the OV (5) is a *EDWARDS RV8* [59]. The OV is held in place over a dewar (3) filled with LN. Gas inlet, vacuum connection (connected to a *AFRISO EN 837-1* analogous pressure gauge [61]) and electric feedthrough (6) are mounted on the topside of the OV. A *VACOM ATMION ATC 40 CLE* filament pressure gauge [62] (7) is attached to the gas inlet system. A *EA-PS 2084-03B* [63] (8) is used as power supply for the resistor circuit R_2 of

the heating system. A *Voltcraft PS 2403 Pro* (9) [64] is used to supply the resistor circuit R_1 and the relay of the heat control system. An *Agilent E3661A* [65] is used to supply the OPs. The power supplies for the bias voltage of the SiPM and the PMT (11/12) both are a *iseg SHQ 122M* [66]. The oscilloscope (13) that is used to acquire data is a *LeCroy WaveRunner 6100A* [67]. The heat control system is regulated via the program *NI LabView 2014* [68] via a measuring PC (14). The PC is connected to two DAC cards, a *Meilhaus RedLab ME-RL-TEMP 1130801E7* to acquire the temperature information and a *Meilhaus 168FFF5* [69] (both not seen on the image). The utilized temperature sensors are *LakeShore PT-100* [70].

4.4 Measuring Process

The primary light source is scintillation light from gaseous xenon produced by α-particles. The radioactive α-source is centered in the cavity on the bottom of the xenon cell. Fig. 4.11(a) shows a measurement of the energy spectrum of the used α-particle source. It is a mixed supplement consisting of 12 % ^{244}Cm , 48 % ^{241}Am and 40 % ^{239}Pu. Those isotopes emit α-particles with a kinetic energy of about 5.1 MeV to 5.8 MeV. The detectors are placed above the radioactive source facing downwards (see sec. 4.1.3). The α-particles lose energy while propagating through the xenon and produce scintillation light. The mean range depends on the energy of the particle. Since the kinetic energy of the α-particles is negligible compared to their masses, the mean range can be approximated using the *Bethe-Bloch* formula of the form [71]:

$$\frac{\mathrm{d}\,E}{\mathrm{d}\,x} = \frac{\rho\,K\,Z}{A\,\beta^2}\left(\ln\left(\frac{2\,m\,c^2\,\beta^2\,\gamma^2}{I} - \beta^2\right)\right) \quad , \tag{4.1}$$

where $\mathrm{d}\,E$ is the energy loss of the α-particle over the distance $\mathrm{d}\,x$, ρ the density of the xenon, Z the atomic number and A the atomic mass of the medium, $\gamma = \frac{E}{M\,c^2}$ the Lorentz factor and $\beta = 1 - \left(\frac{M\,c^2}{E}\right)^2$. K is a constant with the numerical value $K = 0.307\,\frac{\mathrm{MeV\,cm^2}}{\mathrm{g}}$ and I the mean excitation potential of the electrons of the xenon. For an atomic number $Z > 20$, I can be approximated via $I = 10\,Z\,\mathrm{eV}$ [71].

To approximate the range iteratively with respect to the energy loss, the parameters β and γ are calculated individually for each energy. The iteration steps are chosen so that the energy loss of the α-particles is assumed to be constant over a distance of 1 µm. This way, the mean range of the α-particles is approximated to be $\approx 1.7\,\mathrm{cm}$. Since scintillation light is produced all along the track of an α-particle, the origin of the scintillation light cannot be described as a point

source. If the particle propagates towards one detector, the photon fluence on the other detector will be lower. Therefore, a sufficient statistic necessary to be able to assume an equalized light distribution in the xenon cell during one measurement.

Fig. 4.11 shows a simulation of the path of 500 α-particles emitted by the radioactive source. The yellows dots indicate the iteration steps of the simulation for the α-particles. The mean range of the α-particles extracted from the simulation is approximately 2 cm [72]. The purple lines denote the socket for the α-source. The SiPM and the PMT are arranged on the top side. The red lines indicate the outside surface and the gray lines indicate the inside surface of the copper cup. The simulation shows that the α-particles are distributed equally over all solid angles. Therefore, it can be assumed that the scintillation light in the xenon cell is equally distributed as well for a sufficient statistic.

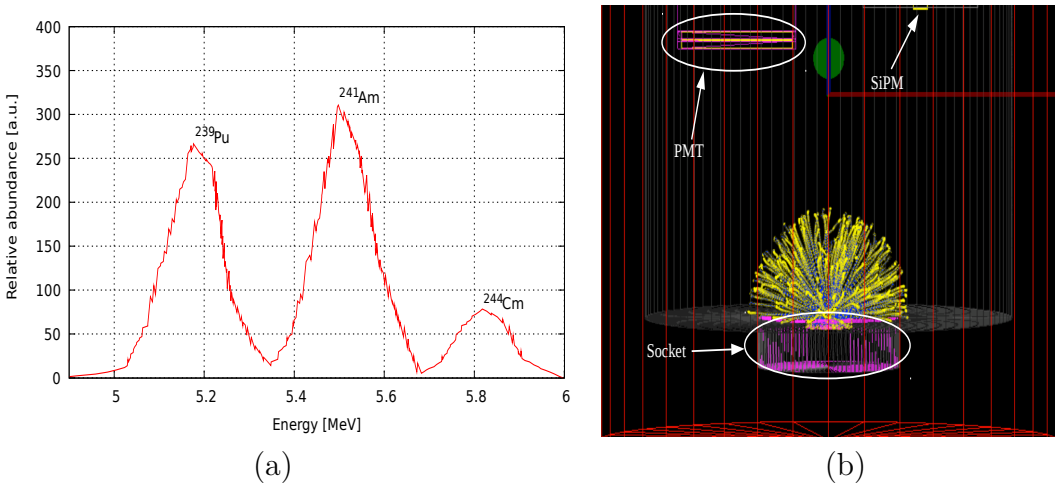

Figure 4.11: (a) Energy spectrum of the used α-particle source. It consists mainly of ^{239}Pu, ^{241}Am and ^{244}Cm. These measurements were done by Jürgen Hößl as part of the EXO/nEXO - work group Erlangen. (b) Simulated track of 500 α-particles emitted by the source in the copper cup.

5 Data Analysis

This chapter explains the basic analytic techniques that are used to obtain information about characteristic properties of the SiPM and the PMT. Methods of noise reduction are introduced. Data acquisition was done with a *LeCroy WaveRunner 6100A* oscilloscope [67]. The initial negative pulses are inverted in the analysis. In the following, the absolute values of U_{bias}, U_{break} and U_{over} are used. The analysis is performed with a *C++* and *gnuplot* [73] based program.

5.1 Pulse Height Spectrum

An important analytic tool is the pulse height spectrum (PHS). Characteristics that are necessary to calculate the breakdown voltage, the CT probability and the number of CT induced p.e. can be derived from it.

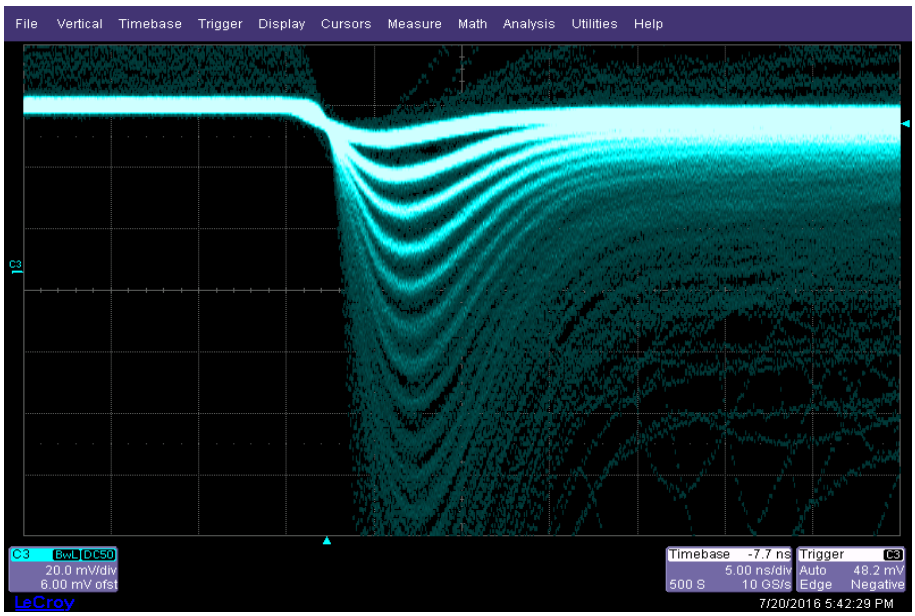

Figure 5.1: Oscilloscope screen during a measurement in the absence of light of the used SiPM. About 100,000 waveforms are pictured at the same time. Lighter areas indicate a higher density of data points. The discretized structure arises from the discrete number of avalanches that can be measured as a signal. Eleven p.e. can be resolved in this image.

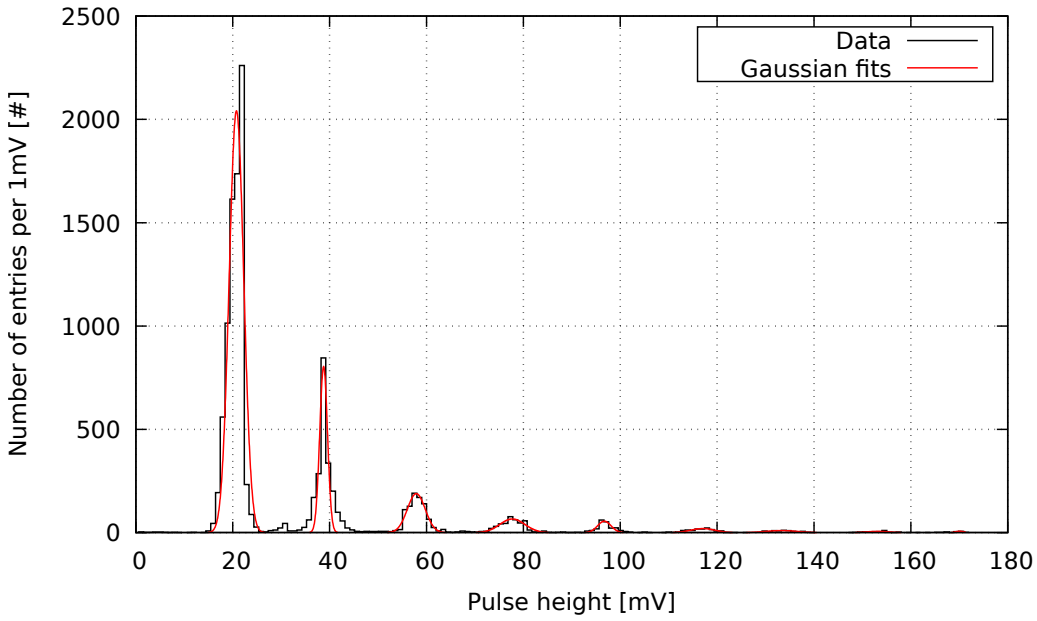

Figure 5.2: Pulse height spectrum resulting from 12,000 waveforms of a measurement that was taken in the absence of light. The applied bias voltage is 32 V at a temperature of −21°C. Each peak arises from pulses that correspond to a discrete number of p.e..

Fig. 5.1 shows an image of the screen of an oscilloscope. About 100,000 waveforms are displayed at the same time. Bright areas denote a high density of data points, dark areas a low one. The discretization of the individual pulses leads to the formation of the discrete structure. Each individual pulse arises from a certain number of p.e.. The measurement was recorded in the absence of light. Therefore, the pulses originate from dark count events. In order to find the mean value of the height of the pulses with a certain number of p.e., the maximum value within each waveform is identified. These values are entered in a histogram, the so called PHS. Fig. 5.2 shows a PHS resulting of a measurement in the absence of light. The discretization of the pulse signals manifests as peaks at certain pulse height values. Those peaks denote the maximum values of pulses with a certain number of p.e.. A Gaussian fit is applied to each peak. The center of this Gaussian distribution represents the mean height of this particular number of p.e..

Some entries between the distinct peaks arise from pulses that do not seem to have a discretized height. Those entries originate from after-pulses (see sec. 3.15) and are removed in order to calculate the CT probability and the number of CT induced p.e.. Fig. 5.3 shows the maximum value within each waveform in dependence on its temporal appearance relative to the trigger time. The discrete structure arises from prompt pulses, on which the measurement was triggered.

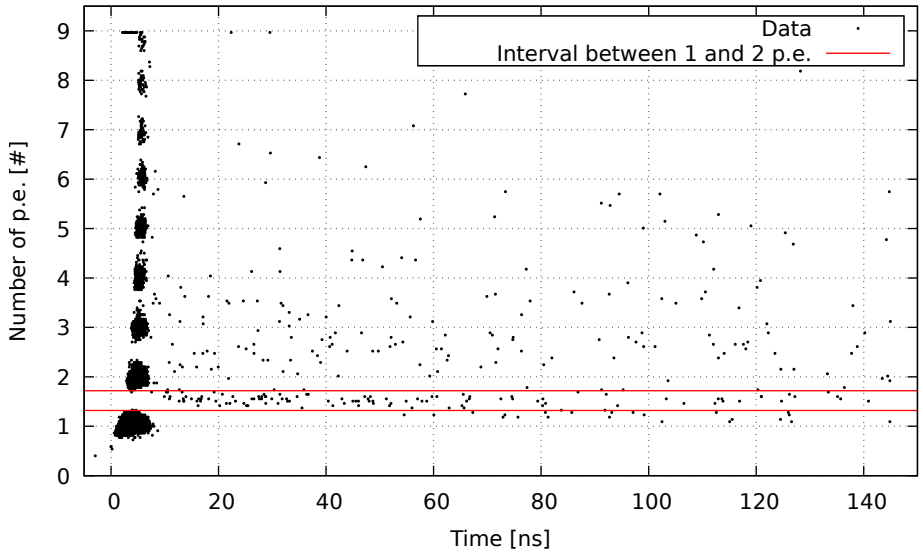

Figure 5.3: Number of p.e. of each individual waveform of a measurement in the absence of light in dependence on their temporal appearance. The discrete structure arises from pulses the measurement was triggered on. The red lines indicate the interval between the one and two p.e. peak. Several entries that arise from after-pulses appear delayed to the prompt ones.

The biggest accumulation at about 20 mV is formed by 1 p.e. pulses, the second biggest at about 40 mV from 2 p.e. pulses and so forth. The red lines indicate the pulse height interval between the 1 and 2 p.e. peak. This interval is chosen arbitrarily to outline pulse maxima that appear far later after the trigger time and do not contribute to either the 1 p.e. or the 2 p.e. peak. These entries can be removed by setting constraints on the temporal appearance of the pulse maximum. The number of measured after-pulses decreases if the observed time interval is chosen smaller. Pulse maxima from after-pulses are, therefore, less likely to appear if the maximum is identified shortly after the oscilloscope was triggered. Fig. 5.4 shows several recorded pulses. The black pulses occur with global maxima a few ns after the oscilloscope was triggered. The red waveforms contain additional delayed pulses that exceed the initial prompt maxima. The vertical blue lines indicate the limits of the time interval in which the maximum value is identified to exclude delayed pulses. This interval is chosen to be [-2 ns , 10 ns] relative to the trigger time. Therefore, these delayed maxima do not contribute to further analysis. Fig. 5.5 shows two PHS of the same measurement. The blue PHS is analyzed without temporal constraints on the maximum. The red PHS contains only maxima that occur in the time interval mentioned above. The entries between the peaks are almost completely removed while the number of entries that contribute to the peaks is nearly the same.

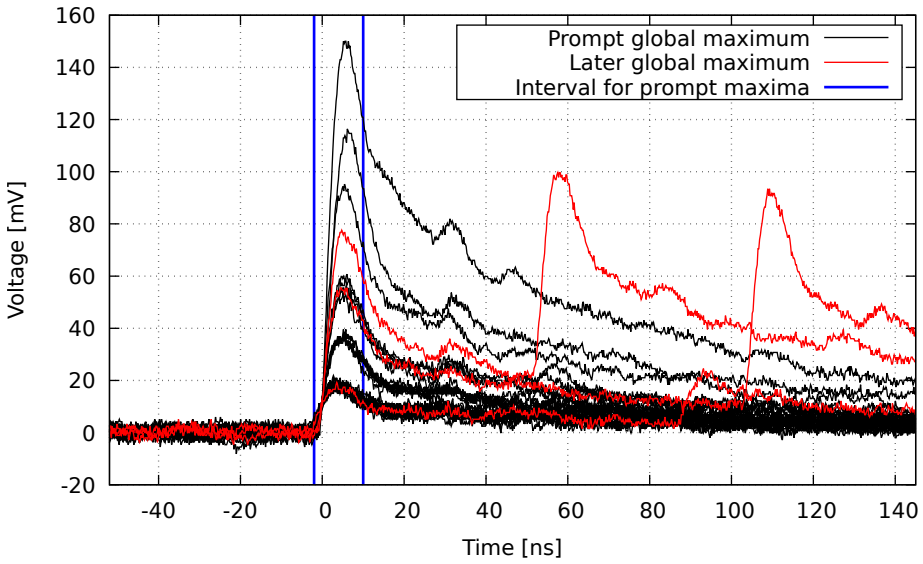

Figure 5.4: Waveforms containing pulses that reach their global maximum shortly after the oscilloscope was triggered (black) and waveforms containing several pulses that reach the global maximum later (red). In order to exclude the later pulses, the maximum value is identified in a time interval around the trigger time (vertical blue lines).

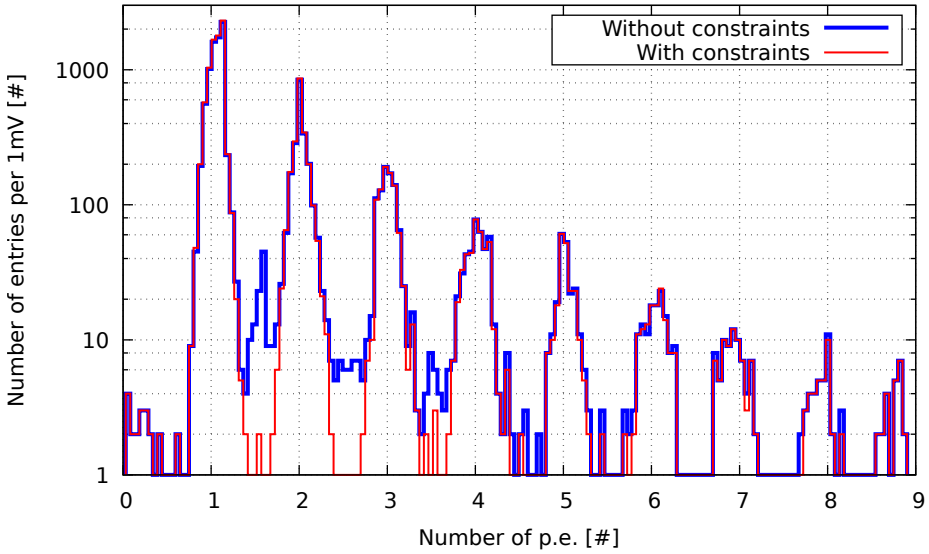

Figure 5.5: PHS of a measurement in the absence of light without constraints on the temporal appearance of the pulse maximum (blue) and with constraints (red). The entries between the distinct peaks vanish almost completely.

5.2 Charge Spectrum

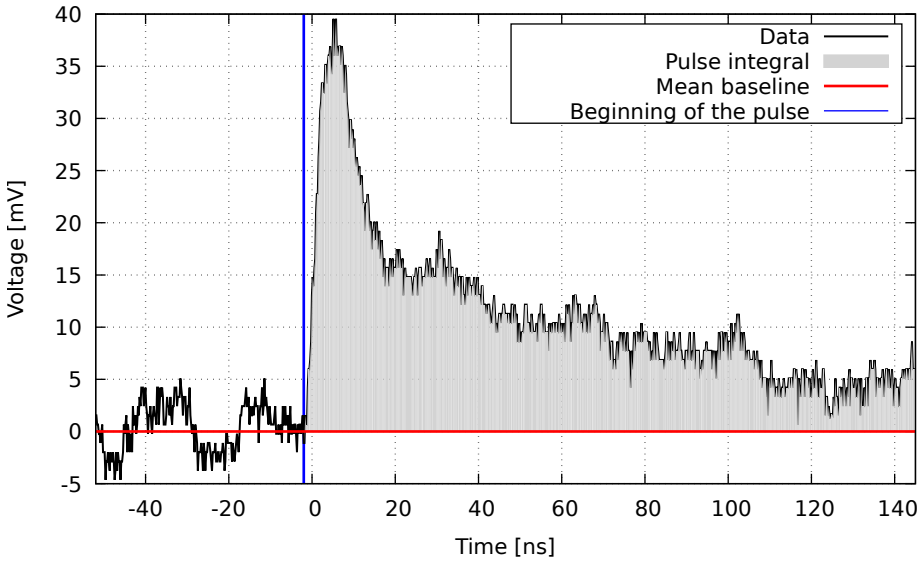

Figure 5.6: Calculation of the pulse integral. The mean value of the data until right before the pulse (vertical blue line) is calculated and corresponds to the baseline (red). This value is defined as the value of the baseline. All further values are summed with respect to the baseline and multiplied by the sampling time.

Another important tool used in the analysis is the charge spectrum (CS). The pulse integral corresponds to the number of charges in an avalanche in a pixel. The quantified charge signal from the SiPM discretizes the integral of the pulse. The integral and the CS are necessary to perform the PDE calculation. Fig. 5.6 shows an example of how the pulse integral is estimated. The baseline of each waveform is afflicted with statistical fluctuations. To exclude contributions to the integral from a possible offset of the signal, a mean value for the baseline is estimated. Therefore, the data points from the beginning of the waveform until the beginning of the pulse (vertical blue line) are used to calculate a linear fit where the slope is manually set to zero. This linear fit denotes the baseline (horizontal red line). The remaining data is summed with respect to the baseline. This sum is multiplied by the sampling time of the oscilloscope. This yields a value for the pulse integral (gray area) and is calculated for each waveform individually. The beginning of the pulse is estimated empirically to be $-2\,\mathrm{ns}$ relative to trigger time. These values for the integrals contribute to the CS. Fig. 5.7 shows the CS for the same measurement as in fig. 5.2 in a logarithmic scale.

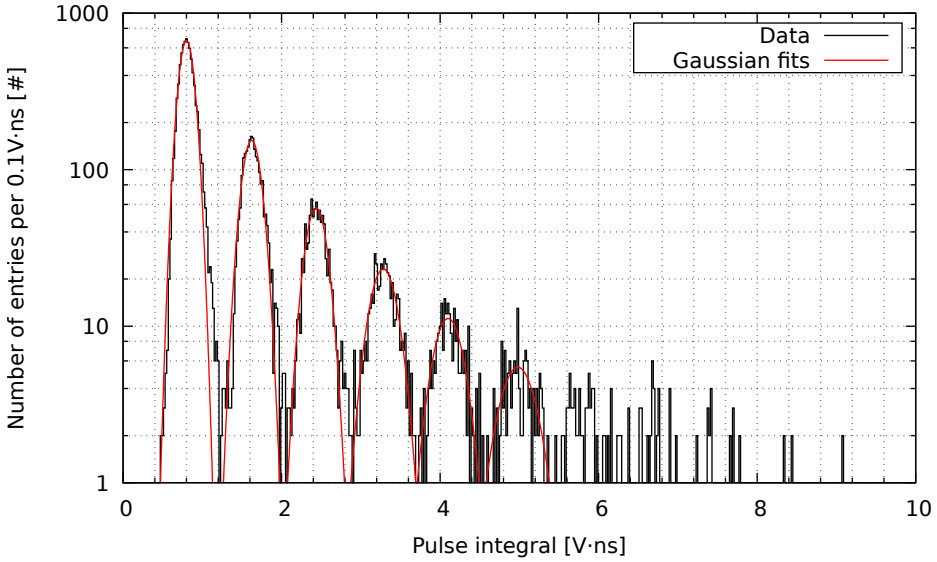

Figure 5.7: Histogram of the pulse integrals of a measurement in the absence of light (charge spectrum) resulting from 12000 waveforms. Analogously to the PHS, each peak in the CS originates from pulses with a discrete integral. Gaussian fits are applied to obtain the center position of each peak.

Due to the operation principle of the PMT (see sec. 3.1) its response is quantized as well. Although the discretization of each pulse cannot be resolved as well as the discretization of the pulses from the SiPM, it is possible to determine the mean value of signals with 1 p.e.. This value is necessary to determine the number of detected photons on the PMT during the PDE measurements.

The signals that are measured with the PMT are afflicted with a low frequency noise. The noise signals are excluded in order to determine an accurate value for the one p.e. peak. Fig. 5.8 shows several pulses from the PMT. The black curves indicate signals that are actually pulses from the PMT. The red curves are low frequency noise signals, whose exact origin is not known. The noise signals are about the same height as one p.e. pulses from the PMT. The trigger settings were chosen so that about 62 % of all recorded signals were triggered by this noise. The pulse signals induced by the PMT, however, differ in characteristics from the low frequency noise so that constraints can be find to select and exclude noise triggered waveforms from further analysis.

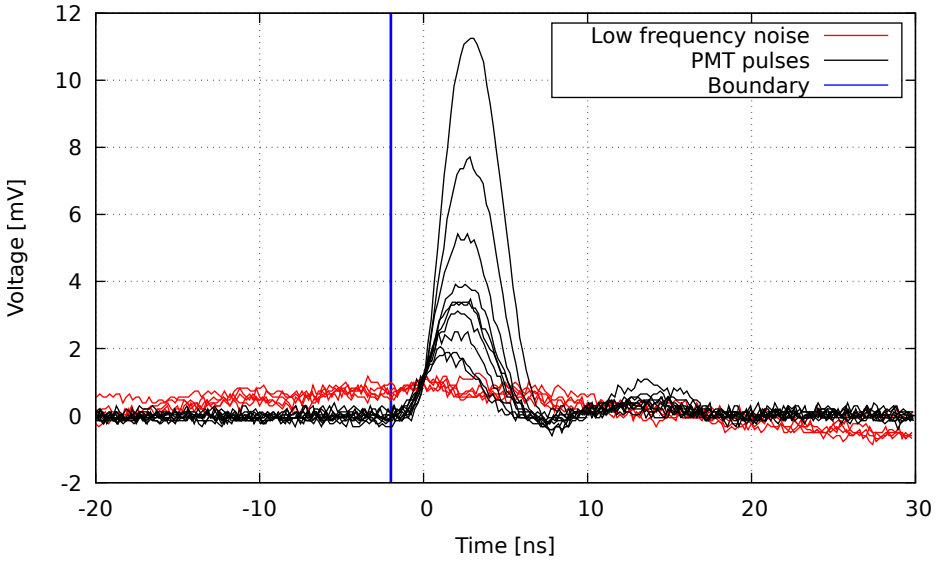

Figure 5.8: PMT pulses (black) and low frequency noise signals (red). The data from the beginning of each waveform until $-2\,\mathrm{ns}$ relative to the trigger (vertical blue line) is used to calculate the slope of the baseline. The slope is further used to discriminate between PMT pulses and low frequency noise signals.

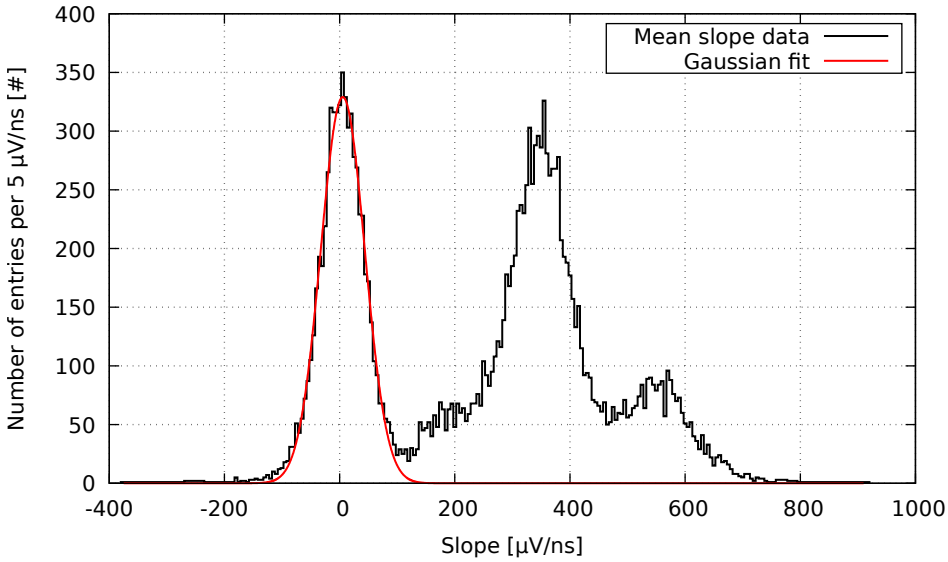

Figure 5.9: Histogram of about 53000 slopes that are extracted from a PMT measurement. The first peak around $0\,\frac{\mu\mathrm{V}}{\mathrm{ns}}$ arises mainly from waveforms containing no low frequency noise signals. Only waveforms that contribute to this peak are taken into account in the further analysis. The limit is distinguished by applying a Gaussian fit to the peak and calculating the boundary of the $3\,\sigma$-interval.

The data from a PMT signal fluctuates around zero until the beginning of the pulse. In contrast, the noise signal tends to rise from the beginning of the waveform until the oscilloscope is triggered. To distinguish PMT pulses from noise signals, a linear fit is applied to the data within each waveform until the beginning of the pulse (vertical blue line in fig. 5.8). This boundary is chosen empirically. The best result is obtained for a limit at $t = -2\,\mathrm{ns}$ relative to the trigger time. The slopes of the resulting fits are entered in a histogram (see fig. 5.9). Two dominant distributions can be recognized. The peak around $0\,\frac{\mu\mathrm{V}}{\mathrm{ns}}$ arises mainly from signals that are induced by PMT pulses. The peak around $350\,\frac{\mu\mathrm{V}}{\mathrm{ns}}$ arises mainly from signals that are induced by low frequency noise signals. To exclude the latter ones, only waveforms with a slope lower than a certain boundary are taken into account in the further analysis. To choose this boundary, a Gaussian fit is applied to the peak distributed around $0\,\frac{\mu\mathrm{V}}{\mathrm{ns}}$. This boundary is chosen so that the data that is contained in the $3\,\sigma$-interval of the Gaussian fit is still taken into account in the further analysis. Fig. 5.10 shows two CS of the PMT, both from the same measurement as in fig. 5.9. The red graph shows the CS with constraints on the slope and the black graph shows the CS without constraints. Due to these constraints on the slope, the accumulation around $0\,\mathrm{mV\,ns}$ vanishes and a broad distribution at about $8\,\mathrm{mV\,ns}$ emerges.

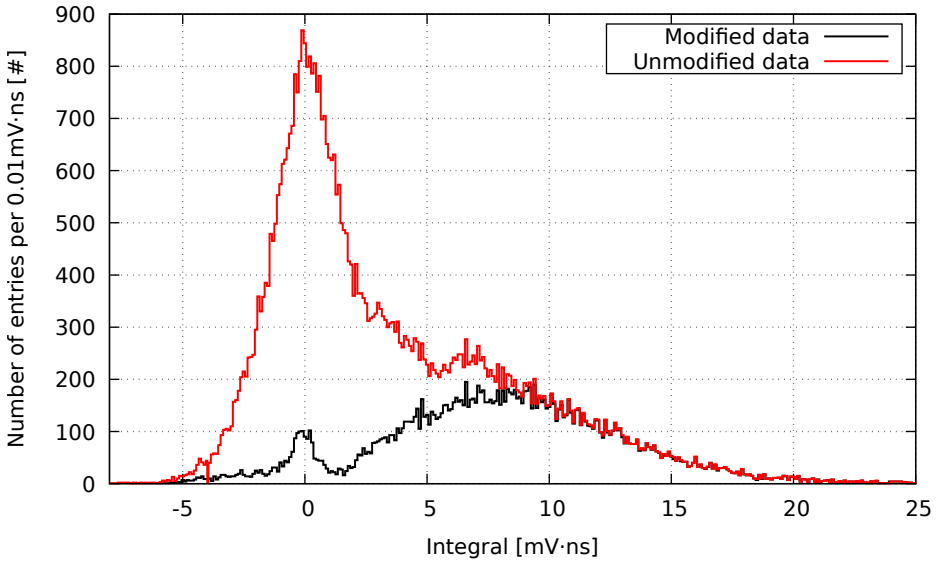

Figure 5.10: Comparison of the CS of the PMT without noise reduction (blue) and with noise reduction (black) at a temperature of $-91\,^{\circ}\mathrm{C}$. The noise peak around zero becomes subdominant compared to a broader peak that is used to distinguish the one p.e. of the PMT. The modified data contains about 20,000 and the unmodified about 53,000 waveforms.

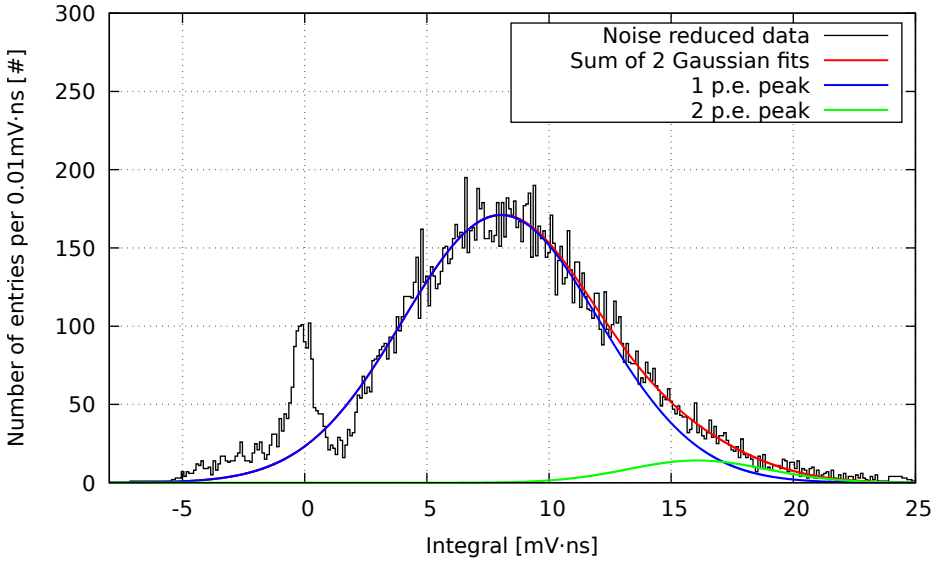

Figure 5.11: CS of the PMT with reduced noise at −91 °C. The broad peak is a super position of remaining noise signals, the one p.e. peak and p.e. peak. A sum of two Gaussian functions is fit to the data (red) yielding the one p.e. peak (blue) and the two p.e. peak (green).

Fig. 5.11 shows this distribution. It arises from a super position of the one p.e. and the two p.e. peak. The two p.e. peak is subdominant compared to the one p.e. peak and causes the distribution to be slightly shifted towards higher values. In contrast, towards lower values, the distribution seems to fall rapidly at about 2 mVns. This abrupt edge is caused by the trigger threshold. Values below this point are caused by background noise and residual entries of the low frequency noise. In order to determine the value of the one p.e. peak, the sum of two Gaussian distributions (red) is fitted to the data. The center position C_2 of the Gaussian fit that is applied the two p.e. (green) was manually set to be $2\,C_1 = C_2$, where C_1 is the center position of the Gaussian fit that is applied to the one p.e. peak (blue). The center position C_1 is used as value for the one p.e. peak in the further analysis. To measure the one p.e. peak, the inner chamber was evacuated to avoid scintillation light caused by α-particles in the xenon. Due to thermal conduction in the xenon cell, it is not possible to cool down the PMT below a temperature of -91 °C while the xenon cell was evacuated. The PDE measurements were done at a temperature of −98 °C. The impact of the temperature difference of 7° on the position of the one p.e. peak of the PMT is neglected in the further analysis.

6 Determination of Characteristic Properties

This chapter discusses, how characteristics of a SiPM are extracted from the measurements using the basic analytic methods introduced in the previous chapter. Further analysis and data processing techniques are introduced as well. The determination of the Gain, breakdown voltage, crosstalk and photon detection efficiency of the investigated SiPM are outlined. Characteristics of the xenon cell are compared to a dedicated simulation. This simulation was developed in the EXO/nEXO - work group Erlangen [72, 74]. The conversion efficiency of *Lumogen*® at VUV wavelengths is determined.

6.1 Basic Concept

To determine the PDE of a SiPM, several characteristics of a SiPM need to be analyzed beforehand. Hereinafter, the necessity to investigate those parameters is motivated.

In order to determine the PDE of a SiPM, the number of photons $N^{\gamma}_{\mathrm{SiPM}}$ that actually impinged onto the SiPM and the number of photons $N^{\gamma'}_{\mathrm{SiPM}}$ registered by the SiPM need to be investigated. $N^{\gamma}_{\mathrm{SiPM}}$ is evaluated via the photon fluence Φ_{SiPM} and the effective detection area A_{SiPM} of the SiPM. To calculate Φ_{SiPM} in return, the photon fluence Φ_{PMT} onto the reference PMT is examined. To do so, the total number of measured photons $N^{\gamma'}_{\mathrm{PMT}}$ by the PMT needs to be extracted from the sum of all pulse integrals $J^{\mathrm{PMT}}_{\mathrm{total}}$ and the average value for the one p.e. peak of the PMT. Φ_{PMT} can be obtained using the photon detection efficiency of the PMT, the xenon scintillation light spectrum and the effective detection area A_{PMT} of the PMT. Using a simulation that was done for the particular configuration of the setup, Φ_{SiPM} can be calculated from Φ_{PMT}. After that, $N^{\gamma'}_{\mathrm{SiPM}}$ is extracted from the number of p.e. N'_{SiPM} that are measured by the SiPM and the percentage number of crosstalk induced p.e. P^{*}_{CT}. N'_{SiPM} can be obtained from the sum of all pulse integrals $J^{\mathrm{SiPM}}_{\mathrm{total}}$ and the gain G of the SiPM, which is extracted from the measurements. To compare the investigated SiPM to other

devices, the characteristics are expressed in dependence on the overvoltage U_{over}. Therefore, the temperature dependent breakdown voltage $U(T)$ is investigated.

6.2 Gain

The signal voltage U_{s} of a pulse of a SiPM is linearly dependent on the number of registered p.e.. Therefore, the peaks in a PHS are located equally spaced in a distance of ΔU_{s} from each other, which is shown in fig. 6.1(a).

The gain G is a factor by which a charge carrier in a pixel is multiplied in the induced avalanche. The signal voltage is dependent on the number of charge carriers in the avalanche. Therefore, the gain determines the height of a pulse. G is linearly dependent on the bias voltage U_{bias} (see equ. 3.5). Therefore, the position of the p.e. peaks in a PHS depends on U_{bias}. Fig. 6.1(b) shows four PHS for different bias voltages. The distance ΔU_{s} between the peaks is increased for larger values of U_{bias}. In order to investigate the gain for a certain bias voltage, the center position of each p.e. peak is determined as explained in sec. 5.1 . Fig. 6.2 shows the center positions of the p.e. peaks dependent on the number of p.e.. A linear fit is applied to each set of data. The slope of the fit yields the gain.

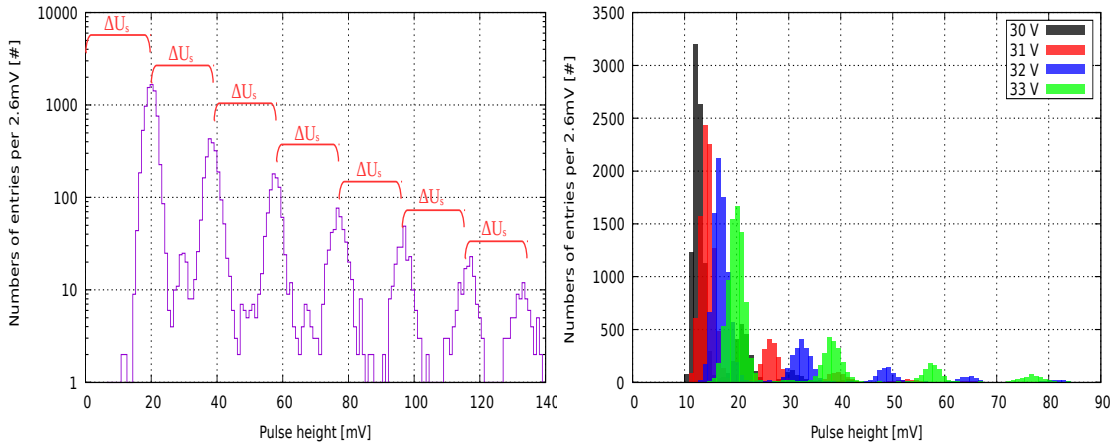

(a) (b)

Figure 6.1: (a) PHS where all p.e. peaks are located equidistantly from each other. (b) PHS with different applied bias voltages. The distance between the p.e. peaks rises with the bias voltage.

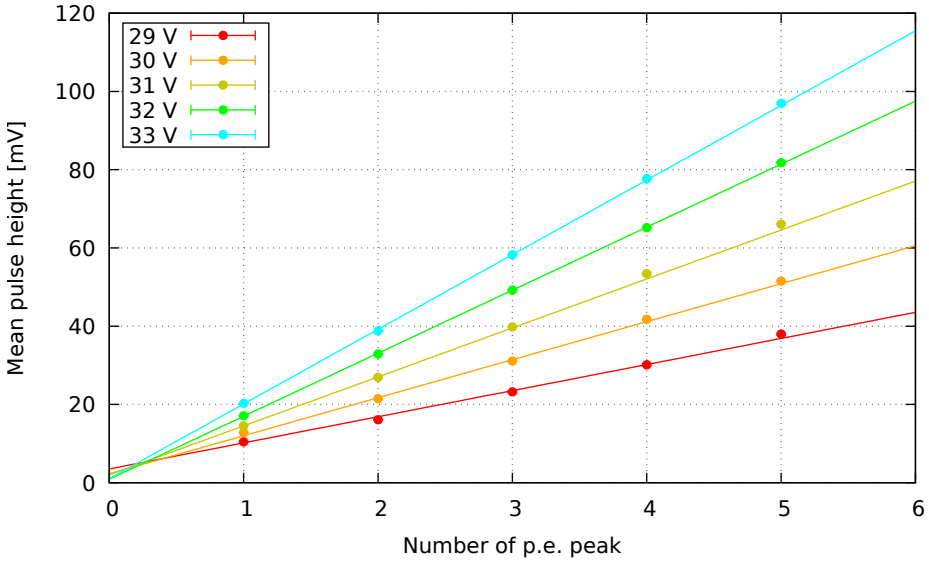

Figure 6.2: Center positions of the p.e. peaks in a PHS for different bias voltages. The gain, being the slope of the applied linear fit, rises with the bias voltage. These measurements were taken at about −21 °C.

In order to determine the PDE, the position of the one p.e. peak in the CS is calculated since it is equal to the signal of one triggered pixel in the SiPM for this particular bias voltage. But since background noise in the used electronic devices can add an offset to the measured signals, the one p.e. peak is not necessarily centered between zero and the two p.e. peak. Therefore, the gain is used for further analysis instead of the position of the one p.e. peak. To determine the PDE, the gain is extracted from a CS as well. To obtain an accurate value, the entire pulse integral is calculated until the pulse has completely subsided. This time lies in the region of a few µs. Only a time window of about 100 ns after the trigger is recorded with the used settings on the oscilloscope. Fig. 6.3 shows the sum of 99,500 waveforms for such a measurement. Every entry of every waveform is summed with respect to its temporal appearance. This representation shows the mean shape of the measured pulses. Since only the time window mentioned above was acquired, a significant part of the declining pulses is missing. Therefore, the gain that is calculated from the CS from these measurements needs to be corrected. The missing part of the pulse integrals is reconstructed. Since the pulse integral scales linearly with the gain, a correction factor can be obtained from the sum of the reconstructed pulse integrals.

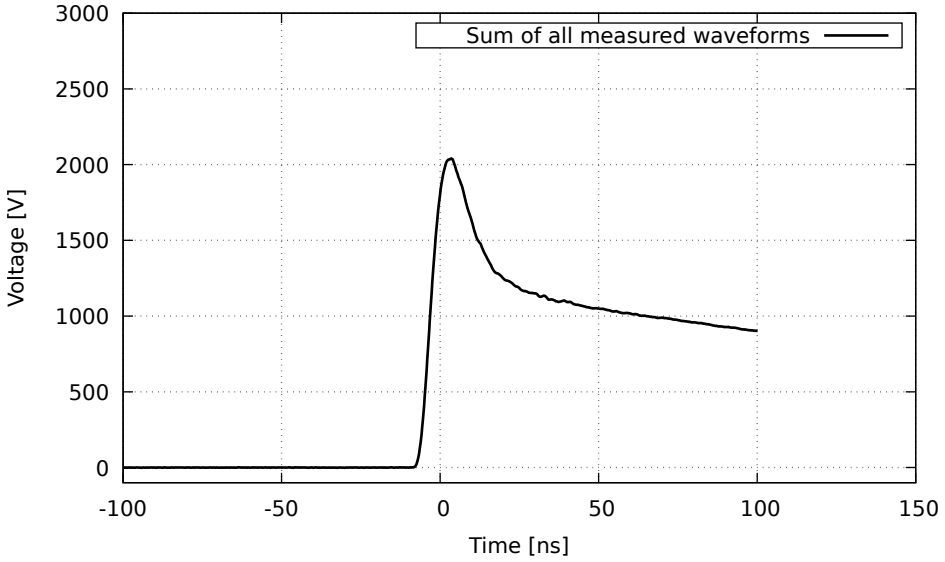

Figure 6.3: Sum of 99,500 waveforms. Every entry in every waveform is summed with respect to its temporal appearance yielding the mean shape of the recorded pulses.

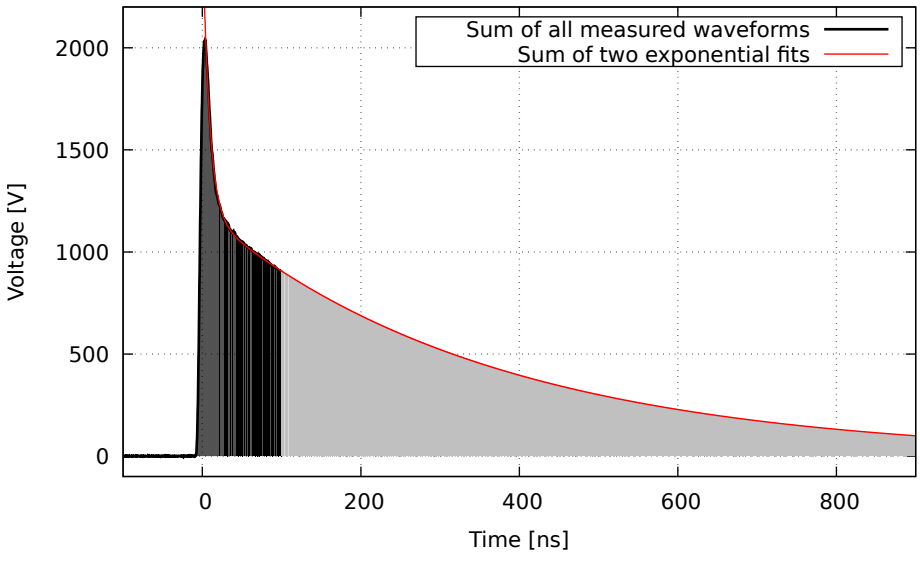

Figure 6.4: Sum of 99,500 waveforms. Every entry in every waveform is summed with respect to its temporal appearance yielding the mean shape of the recorded pulses. The sum of two exponential functions (red) with different time constants is fit to the data with respect to the baseline. The integral of this function (gray) is calculated from the time of the last entry until infinity. The sum of all entries (black) yields the pulse integral of the measured values.

The missing part is calculated by applying an exponential fit to the data. Fig. 6.4 shows the same data as in fig. 6.3 on a larger timescale. An exponential function $U(t)$ of the form:

$$U(t) = A \cdot e^{-B \cdot t} + C \cdot e^{-D \cdot t} \tag{6.1}$$

is applied, where t is the time relative to the trigger and $U(t)$ the signal voltage. A, B, C, D denote fit parameters. In order to subtract a possible offset, all values before $-2\,\mathrm{ns}$ relative to the trigger time are used to calculate the baseline by a linear fit. The integral of the exponential function is calculated from the time t^* of the last recorded entry to infinity with respect to the baseline:

$$\int_{t^*}^{+\infty} U(t)\,\mathrm{d}t = \frac{A}{B} \cdot e^{-B \cdot t^*} + \frac{C}{D} \cdot e^{-D \cdot t^*} \quad . \tag{6.2}$$

This yields the sum of all missing pulse integrals J_{reconst} of all waveforms (gray area in fig. 6.4). The black area indicates the corresponding sum of all integrals J_{measured} up to the time t^*. J_{measured} is not derived from the exponential fit, but directly from the measured values. To correct the gain, the sum of the total pulse integrals, $J_{\mathrm{total}} = J_{\mathrm{measured}} + J_{\mathrm{reconst}}$ is related to J_{measured}. Since the pulse integral scales linearly with the gain, the gain G_{c} of the corrected pulse integrals can be calculated via:

$$G_{\mathrm{c}} = G \cdot \frac{J_{\mathrm{total}}}{J_{\mathrm{measured}}} \quad , \tag{6.3}$$

where G is the gain extracted from the measured pulse integrals. G_{c} is calculated individually for each applied bias voltage. Fig. 6.5 shows the gain values that are estimated to determine the PDE in dependence on the applied bias voltage. A linear fit yields the relation:

$$G = (0.22 \pm 0.02)\,\mathrm{ns} \cdot U_{\mathrm{bias}} - (6.12 \pm 0.51)\,\mathrm{V\,ns} \quad . \tag{6.4}$$

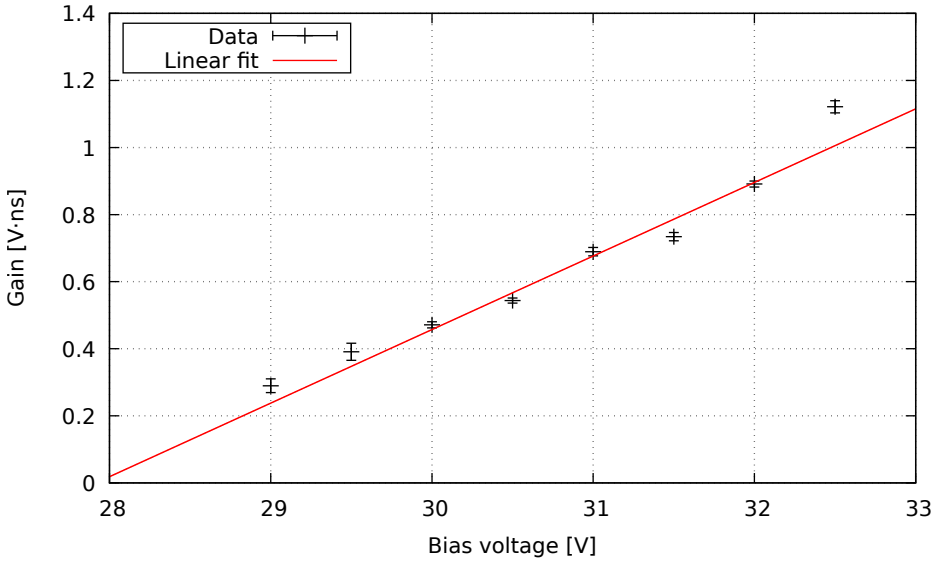

Figure 6.5: Corrected gain extracted from a CS in dependence on the applied bias voltage. A linear fit is applied.

6.3 Breakdown Voltage

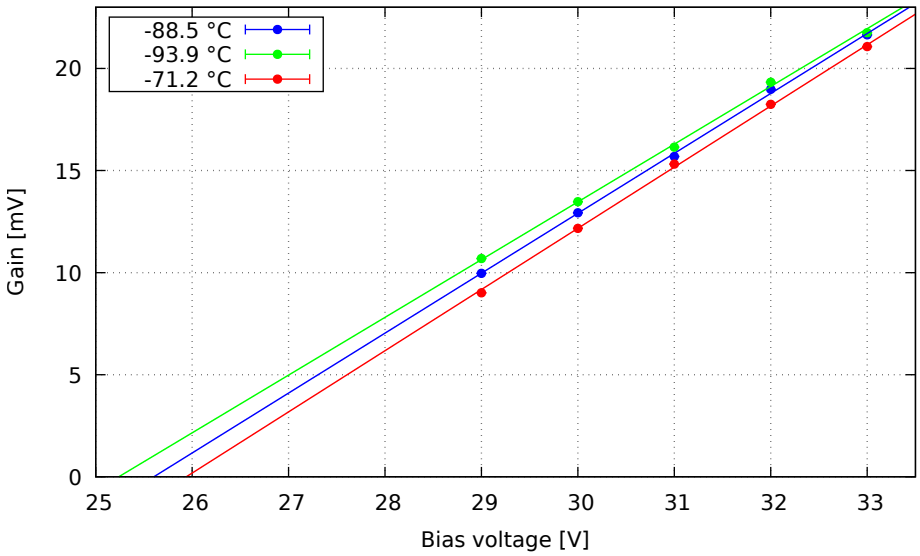

Figure 6.6: Gain extracted from a PHS in dependence on the applied bias voltage. The gain scales linearly with the applied bias voltage. The zero point equals the breakdown voltage U_{break}. The values for U_{break} increase with the temperature.

As explained in sec. 3.2.3, a certain bias voltage, the breakdown voltage U_{break}, is necessary to induce an exponential avalanche in a pixel. Therefore, the gain is assumed to be zero for an applied bias voltages below U_{break}. This voltage can be extrapolated from gain measurements of different bias voltages. Fig. 6.6 shows the gain extracted from a PHS in dependence on the bias voltage for three different temperatures. A linear fit of the form:

$$G(U_{\text{bias}}) = m \cdot (U_{\text{bias}} - U_{\text{break}}) \tag{6.5}$$

is applied, where the breakdown voltage U_{bias} denotes the voltage at which G becomes zero. The latter one tends to increase with increasing temperature T. To investigate this dependence, U_{break} is calculated for several temperatures. Fig. 6.7 shows U_{break} in dependence on the temperature. A linear fit is applied and yields the relation:

$$U_{\text{break}} = (0.013 \pm 0.002)\,\text{V}\,^{\circ}\text{K}^{-1} \cdot T + (26.91 \pm 0.12)\,\text{V} \quad . \tag{6.6}$$

The temperature cannot assumed to be constant with time, since the readout electronic of the SiPM heats up during the measurements. Therefore, T was recorded at the beginning and the end of every measurement. The errors on the temperature are due to this interval.

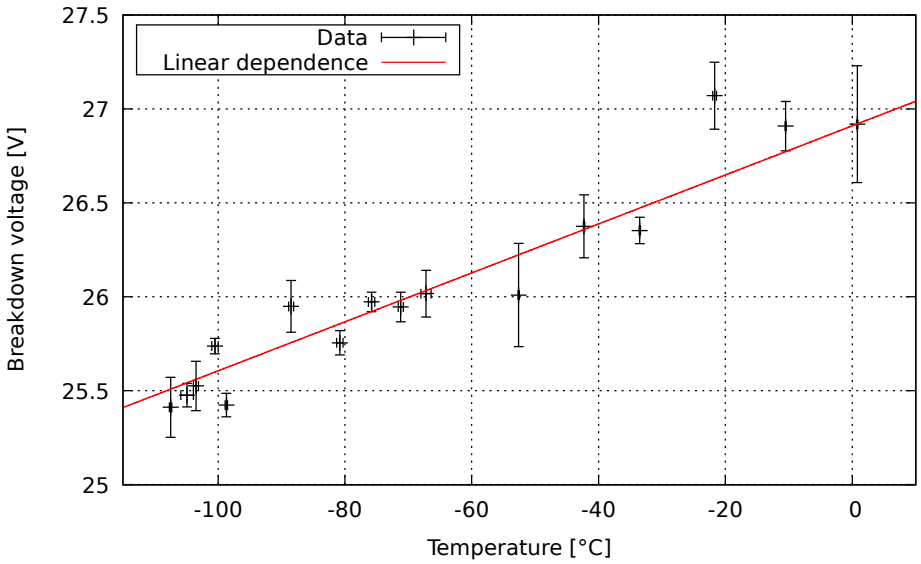

Figure 6.7: Breakdown voltage U_{break} in dependence on the temperature. A linear fit is applied to the data.

6.4 Determination of the Number of Photoelectron Equivalents

In order to calculate N_{SiPM}, two parameters are required: On the one hand, the sum of the pulse integrals $J_{\text{total}}^{\text{SiPM}}$ of every waveform of the PDE measurement and on the other hand, the corrected gain G_{c} extracted from a CS. The value of the gain equals the mean value of a single p.e. signal. Dividing the sum of the pulse integrals by the gain yields the number of registered p.e.:

$$N_{\text{SiPM}}^{'} = \frac{J_{\text{total}}^{\text{SiPM}}}{G_{\text{c}}} \quad . \tag{6.7}$$

As already mentioned, the signal was recorded for only 100 ns after the oscilloscope was triggered. Therefore, the missing part of $J_{\text{total}}^{\text{SiPM}}$ is reconstructed from the PDE measurements as explained in sec. 6.2 for the gain measurements. The pulses of the PMT subside completely within 100 ns. Therefore, the sum of the pulse integrals $J_{\text{total}}^{\text{PMT}}$ of the PMT do not have to be corrected. Since only the one p.e. peak of the PMT could be resolved, the gain cannot be estimated. Therefore, the mean integral of the one p.e. peak C_1 was used to calculate the number of registered p.e. $\text{N}_{\text{PMT}}^{\gamma'}$ on the PMT:

$$N_{\text{PMT}}^{\gamma'} = \frac{J_{\text{total}}^{PMT}}{C_1} \quad . \tag{6.8}$$

6.5 Photon Fluence

6.5.1 Photon Fluence on PMT and SiPM

In order to calculate the absolute number of photons $N^{\gamma}_{\mathrm{PMT}}$ that impinged onto the PMT from $N^{\gamma'}_{\mathrm{PMT}}$, the quantum efficiency QE on the photocathode of the PMT and the scintillation light spectrum of gaseous xenon need to be taken into account. Fig. 6.8 shows both distributions normalized to their highest value. The wavelength is binned to integer values of nm. These data sets were digitized from graphics (PMT QE [39], relative intensity Xe [56]). The relative intensity value $I_{\mathrm{Xe}}(\lambda_i)$ of each wavelength λ_i of the scintillation light spectrum is related to the sum of all intensity values $\sum_j I_{\mathrm{Xe}}(\lambda_j)$. This proportion yields the percentage amount of photons $S_{Xe}(\lambda_i)$ with one particular wavelength:

$$S_{\mathrm{Xe}}(\lambda_i) = \frac{I_{\mathrm{Xe}}(\lambda_i)}{\sum_j I_{\mathrm{Xe}}(\lambda_j)} \quad . \tag{6.9}$$

The $QE(\lambda_i)$ on the photocathode denotes the fraction of the incoming photons with a certain wavelength λ_i that produce a photoelectron. The product of $QE(\lambda_i)$ and $S_{\mathrm{Xe}}(\lambda_i)$ yields the fraction of photons with the wavelength λ_i from

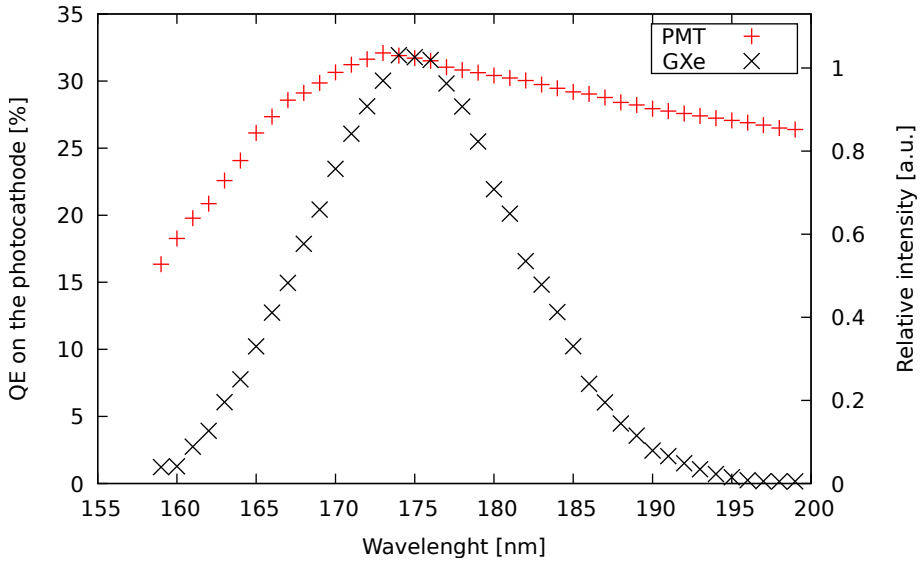

Figure 6.8: QE of the PMT on the photocathode (red, left y-axis) for $U_{\mathrm{PMT}} = 800\,\mathrm{V}$ in dependence on the wavelength. This data was extracted from [39] and rescaled to a maximum value of 32.1 % [75]. The relative intensity of the scintillation light spectrum of gaseous xenon (black, right y-axis) was extracted from [56]. A relative systematical error of 3 % results from the width of the data plot in both graphics. Both data sets are binned to integer values of nm.

the scintillation light that produce a photoelectron on the photocathode. The sum of all fractions corresponding to certain wavelengths λ_i yields the spectral response SR of the PMT to xenon scintillation light and is calculated via the formula:

$$SR = \sum_i QE(\lambda_i) \cdot S_{Xe}(\lambda_i) \quad . \tag{6.10}$$

The relation between $N^{\gamma}_{\mathrm{PMT}}$ and $N^{\gamma'}_{\mathrm{PMT}}$ can therefore be obtained via the formula:

$$N^{\gamma'}_{\mathrm{PMT}} = \varepsilon_{\mathrm{dyn}} \cdot N^{\gamma}_{\mathrm{PMT}} \cdot SR \quad , \tag{6.11}$$

where $\varepsilon_{\mathrm{dyn}} = 0.7$ [75] is the collection efficiency on the first dynode of the PMT. It describes the percentage of photoelectrons that reach the first dynode and produce secondary electrons. The spectral response is calculated to be $SR = 0.30 \pm 0.01$.

The total number of photons $N^{\gamma}_{\mathrm{PMT}}$ impinging onto the PMT during a PDE measurement yields the photon fluence Φ_{PMT} that is defined as:

$$\Phi_{\mathrm{PMT}} = \frac{N^{\gamma}_{\mathrm{PMT}}}{A_{\mathrm{PMT}}} \quad , \tag{6.12}$$

where $A_{\mathrm{PMT}} = (420.25 \pm 4.11)\,\mathrm{mm}^2$ is the effective detection area of the PMT.

Due to geometrical asymmetries in the setup, a correction factor R is needed to calculate the actual photon fluence Φ_{SiPM}:

$$\Phi_{\mathrm{SiPM}} = \frac{N^{\gamma}_{\mathrm{SiPM}}}{A_{\mathrm{SiPM}}} = \Phi_{\mathrm{PMT}} \cdot R \quad . \tag{6.13}$$

R was determined numerically in a simulation of this setup. This value is dependent on the reflectivity of the inner surfaces of the copper cup and the aluminum socket of the α-source. Since these values are not known, R was determined numerically for several combinations of those indices. After that, R was averaged yielding a value of $R = 0.78 \pm 0.03$ [72, 74]. The *Lumogen*® coated surface of the SiPM, which is assumed to be the effective detection area, was measured to be $A_{\mathrm{SiPM}} = (12.96 \pm 0.73)\,\mathrm{mm}^2$.

6.5.2 Surface Reflection of the Xenon Cell

The simulation of this setup [72] yields an average number of photons that impinge onto the PMT per α-particle that propagates through the xenon gas. This number is dependent on the reflection indices of the inner surfaces of the copper cup and the aluminum socket of the α-source. Since these values are not known, all possible combinations of reflection indices in steps of 10 % are simulated. A

diffusive reflection is assumed [72, 74]. The used α-source has a decay rate of about 3.9 kBq. Therefore, the mean time difference between the emission of two α-particles is three orders of magnitudes larger than the dead time of the used oscilloscope. It can be assumed that the light signal of each α-particle can be resolved separately. Therefore, it is expected that every signal that triggered the oscilloscope was caused by one α-particle. The average number of photons impinging onto the photocathode of the PMT during a PDE measurement can be calculated using equ. 6.11. The oscilloscope was triggered 99,500 times during each PDE measurement. Under the assumptions mentioned above, an average number of photons $\bar{N}_\alpha$ that impinged onto the PMT per emitted α-particle can be calculated via:

$$\bar{N}_\alpha = \frac{1}{k} \sum_{i=1}^{k} \frac{N_i^\gamma}{99500} = 3174 \pm 120 \quad , \tag{6.14}$$

where N_i^γ is the absolute number of photons that impinged onto the PMT during one PDE measurement and k the number of PDE measurements.

Fig. 6.9 shows a color map of the simulated reflection indices. The color indicates the number of photons that impinged onto the PMT per α-particle, the x-axis denotes the reflection index of copper and the y-axis the reflection index of aluminum. The white crosses indicate all combinations of the simulated reflection indices that are still in the error interval of $\bar{N}_\alpha$. Several combinations for either a copper reflectivity or an aluminum reflectivity of 0 % were possible as well. These combinations are not listed, since it is assumed that neither the copper nor the aluminum reflectivity is close to zero.

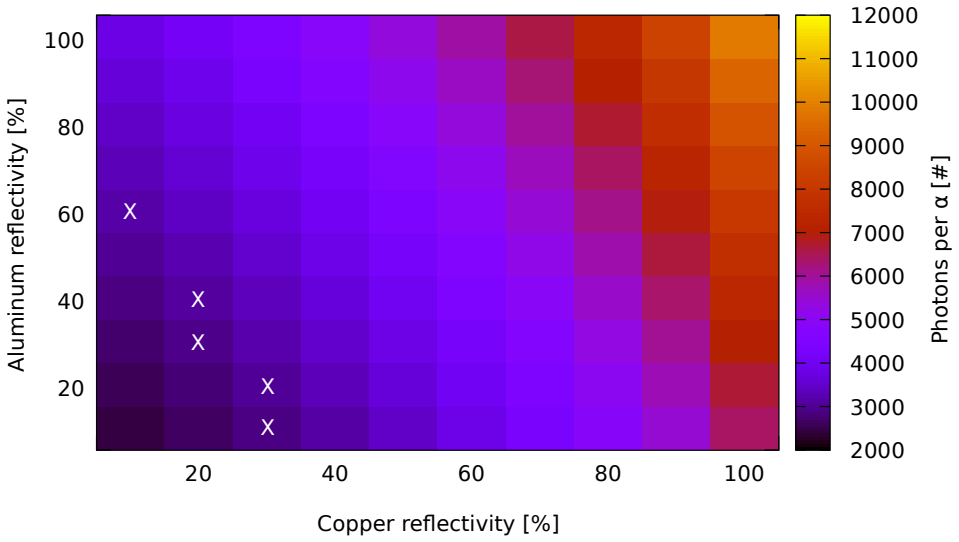

Figure 6.9: Number of photons that impinge onto the PMT per α-particle in dependence on the reflection indices of copper and aluminum. The color indicates the number of photons. The x-axis denotes the reflectivity of copper and the y-axis the reflectivity of aluminum. The white crosses mark the possible combinations for the measured value within the error interval.

6.6 Crosstalk

6.6.1 Crosstalk Probability

Some pulses do not originate from photons that impinge onto the SiPM during a PDE measurement. Since dark count events can be neglected at temperatures around $-100°C$, these signals are mainly induced by crosstalk (see sec. 3.2.4) and after-pulsing (see sec. 3.2.4). Since the measurements were recorded only in a time interval of 100 ns after the oscilloscope was triggered, a significant amount of pulses caused by after-pulsing cannot be taken into account. Therefore, the probability for correlated avalanches is calculated only for CT induced p.e.. The after-pulses that were measured in the recorded time interval, however, are excluded by using a PHS with constraints on the temporal appearance of the pulse maximum.

In order to determine the probability P_{CT} that a crosstalk induced signal appears, the PHS for a measurement in the absence of light is investigated. Fig. 6.10 shows such a PHS rescaled to the number of p.e.. Since it is very unlikely that dark count events occur in two pixels at the same time [35], it can be assumed that every signal with a p.e. higher than one was induced by CT. To identify the entries in the PHS contributing to the one p.e. peak, the center between the one and the two p.e. peak is determined (vertical blue line). To deduce the probability P_{CT}

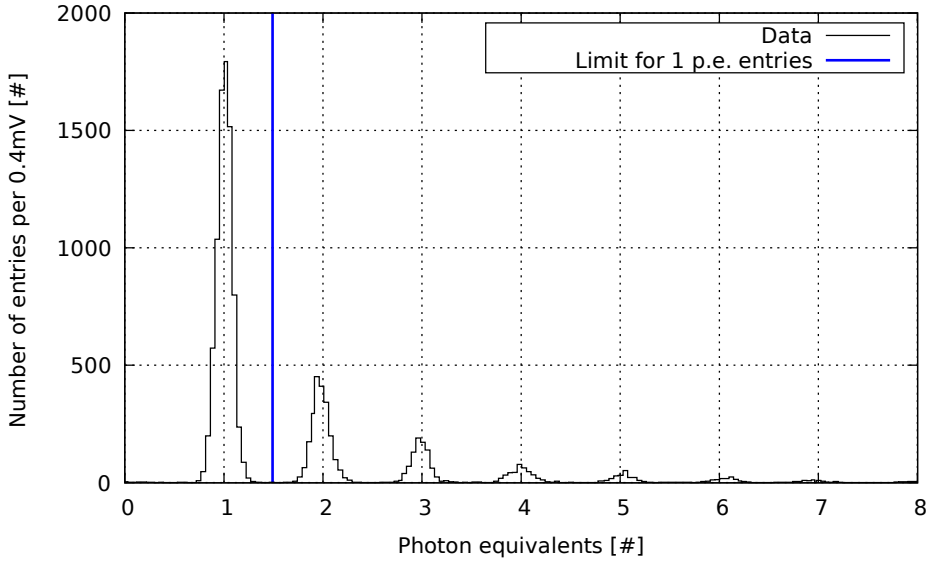

Figure 6.10: PHS of a measurement in the absence of light with constraints on the temporal appearance of the pulse maximum in dependence on the number of p.e.. The center position (vertical blue line) between the one and the two p.e. peak indicates the limit by which entries that contribute to the one p.e. peak are distinguished.

that higher pulses occur, the number of entries M_1 that contribute to the one p.e. peak is compared to the total number of entries M_{total} in the PHS:

$$P_{\text{CT}} = 1 - \frac{M_1}{M_{\text{total}}} = \frac{M_{\text{total}} - M_1}{M_{\text{total}}} \quad . \tag{6.15}$$

Small variations of the limit that determines which entries contribute to the one p.e. peak do not affect the result, since the number of entries in the proximate bins around the limit is exactly zero. The error on the position is, therefore, neglected. But since the calculation of P_{CT} is based on a counting experiment, a Possion error of $\Delta M_1 = \sqrt{M_1}$ is approximated. P_{CT} does not provide information about the actual number of CT induced p.e.. The latter one needs to be known to extract the number of p.e. that were induced by external photons.

Dividing each measured pulse maximum a_i by the gain G of the SiPM yields the number of p.e. corresponding to that pulse. The total number N_{pe} of p.e. of each measurement can be calculated via:

$$N_{\text{pe}} = \sum_i \frac{a_i}{G} \quad . \tag{6.16}$$

N_{pe} does not only include the CT induced p.e. but also the p.e. that are caused by primary dark count events. In order to obtain only the number of CT induced p.e.

N_{CT}, the ones originating from dark count events need to be subtracted. Since each CT event was initiated by a dark count event, one p.e. is be subtracted for every triggered pulse:

$$N_{\mathrm{CT}} = \sum_i \frac{a_i}{G} - M_{\mathrm{total}} \quad . \tag{6.17}$$

Dividing N_{CT} by M_{total} yields the percentage number of CT induced p.e. P^*_{CT}:

$$P^*_{\mathrm{CT}} = \frac{\sum_i \frac{a_i}{G} - M_{\mathrm{total}}}{M_{\mathrm{total}}} \quad . \tag{6.18}$$

Fig. 6.11 shows the measured CT probability and the percentage number of CT induced p.e. in dependence on the overvoltage at a temperature of −60°C. These measurements were done in a *TestEquity LLC 1007C* climate chamber [76]. The horizontal pink line denotes the upper limit for the percentage number of p.e. that are induced by correlated avalanches for the nEXO experiment. A linear fit is applied to the CT probability. It is assumed, that the total number of CT events vanishes for an overvoltage of 0 V. Therefore, the offset is set to zero. The CT probability follows the dependence:

$$P_{\mathrm{CT}}(U_{\mathrm{over}}) = (0.052 \pm 0.001)\,\frac{1}{\mathrm{V}} \cdot U_{\mathrm{over}} \quad . \tag{6.19}$$

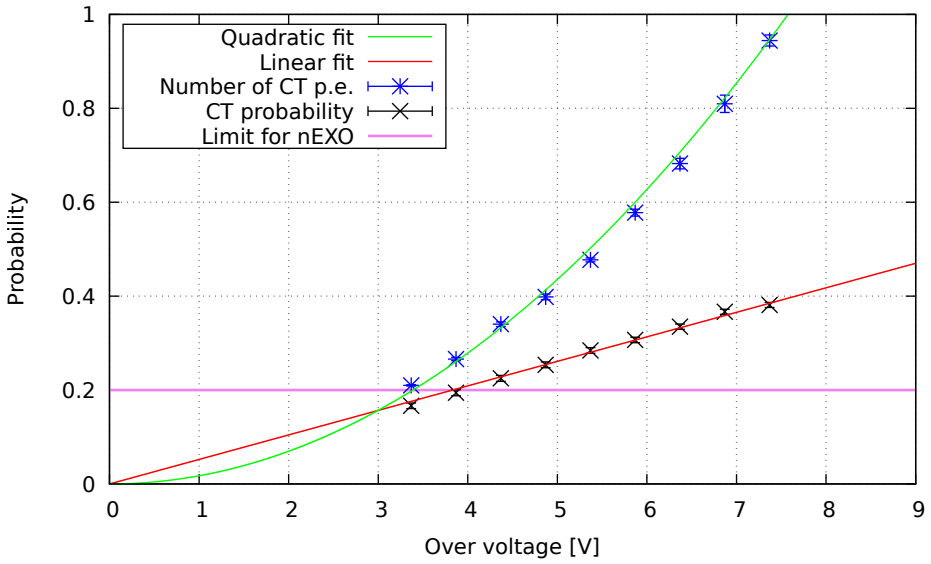

Figure 6.11: CT probability and percentage number of CT induced p.e. in dependence on the overvoltage. The CT probability is linearly dependent on the overvoltage, whereas the percentage number of CT induced p.e. follows a quadratic dependence.

The percentage number of CT induced p.e. follows a quadratic dependence. Again, the assumption is made that the number of CT induced p.e. is zero for an overvoltage of 0 V. This yields the dependence:

$$\mathrm{P}^{*}_{\mathrm{CT}}(U_{\mathrm{over}}) = (0.0174 \pm 0.0003)\ \frac{1}{\mathrm{V}^2} \cdot U^2_{\mathrm{over}} \quad . \tag{6.20}$$

6.6.2 Dependence on the Pixel Area

The CT probability scales linearly with the number of IR photons that are produced by charges in an avalanche. The number of IR photons is proportional to the number of charges in an avalanche. The number of charges scales linearly with the number of doped atoms in one pixel. Assuming an uniform pixel thickness, the number of doped atoms in one pixel is proportional to the pixel area. Therefore, it is expected that the CT probability rises linearly with the pixel area.

To investigate this proportionality, two devices differing only in the effective pixel area are examined: On the one hand, the KETEK PM3350 SiPM that was used in the experiments in this thesis and on the other hand, a KETEK PM3375 SiPM that was investigated by Judith Schneider [50]. The expected ratio of the CT probabilities is equal to the ratio of the areas:

$$\frac{\mathrm{A}_{3375}}{\mathrm{A}_{3350}} = \frac{(75\,\mu\mathrm{m})^2}{(50\,\mu\mathrm{m})^2} = 2.25 \quad . \tag{6.21}$$

A linear fit, where the offset is set to zero, is performed to the data of the CT probability in fig. 3.13. The slope is determined to be $\mathrm{m}_{3375} = (0.125 \pm 0.002)\ \frac{1}{\mathrm{V}}$. Comparing m_{3375} to the slope m_{3350} calculated in 6.19 yields:

$$\frac{\mathrm{m}_{3375}}{\mathrm{m}_{3350}} = 2.4 \pm 0.1 \quad . \tag{6.22}$$

6.7 Photon Detection Efficiency

The absolute number of registered p.e. $N^{'}_{\mathrm{SiPM}}$ is still afflicted with a certain number of CT induced p.e. N_{CT}. Together with the percentage number P^{*}_{CT} of CT induced p.e. , $N^{'}_{\mathrm{SiPM}}$ can be reduced to the number of actually measured photons $N^{\gamma^{'}}_{\mathrm{SiPM}}$:

$$\begin{aligned} N^{'}_{\mathrm{SiPM}} &= N^{\gamma^{'}}_{\mathrm{SiPM}} + N_{\mathrm{CT}} \\ &= N^{\gamma^{'}}_{\mathrm{SiPM}} + N^{\gamma^{'}}_{\mathrm{SiPM}} \cdot P^{*}_{\mathrm{CT}} \\ &= N^{\gamma^{'}}_{\mathrm{SiPM}} \cdot (1 + P^{*}_{\mathrm{CT}}) \quad . \end{aligned} \tag{6.23}$$

Equ. 6.13 yields the absolute number $N^{\gamma}_{\mathrm{SiPM}}$ of photons that impinged onto the SiPM during a PDE measurement. Together with equ. 6.23 an expression for the PDE for xenon scintillation light can be derived:

$$\varepsilon_{\mathrm{SiPM}}(\mathrm{Xe}) = \frac{N^{\gamma'}_{\mathrm{SiPM}}}{N^{\gamma}_{\mathrm{SiPM}}} = \frac{\frac{J^{\mathrm{SiPM}}_{\mathrm{total}}}{G_{\mathrm{c}}} \cdot \frac{1}{\left(1+P^{*}_{\mathrm{CT}}\right)}}{\frac{A_{\mathrm{SiPM}}}{A_{\mathrm{PMT}}} \cdot \frac{J^{\mathrm{PMT}}_{\mathrm{total}}}{C_1} \cdot \frac{R}{\varepsilon_{\mathrm{dyn}}\, SR}} \quad . \tag{6.24}$$

Fig. 6.12 shows the PDE for eight different overvoltages. The errorbars indicate the statistical errors on the measurements. A systematical error of $\Delta_{\mathrm{sys}}\mathrm{PDE} = 12.45\,\%$ (relative to each measured PDE value) arises from uncertainties on the effective detection area A_{SiPM} of the SiPM, the effective detection area A_{PMT} on the PMT, the spectral response SR on the photocathode of the PMT to xenon scintillation light and the geometry correction factor R. Table 6.1 shows the measured parameters and their statistical errors that are used to calculate the PDE.

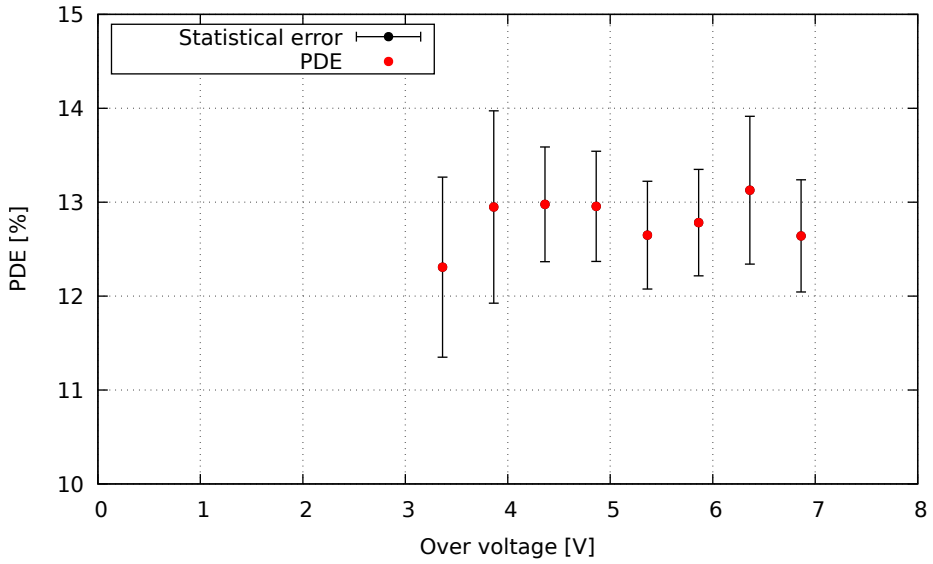

Figure 6.12: PDE of the used SiPM for xenon scintillation light in dependence on the overvoltage. The error bars denote the statistical errors. In addition, a relative systematical error of 12.45 % occurs.

Table 6.1: Measured parameters that are used to calculate the PDE and their errors. A_{SiPM} is the effective detection area on the SiPM, A_{PMT} the effective detection area on the PMT, SR the spectral response of the PMT to xenon scintillation light, R the geometry correction factor, C_1 the value for one p.e. peak of the PMT, G_{c} the gain of the SiPM, $J_{\mathrm{total}}^{\mathrm{SiPM}}$ the sum of the pulse integrals of the measured pulses of the SiPM, $J_{\mathrm{total}}^{\mathrm{PMT}}$ the sum of the pulse integrals of the measured pulses of the PMT, P_{CT}^{*} the percentage number of CT induced p.e. on the SiPM. The mean values and the errors for G_{c}, $J_{\mathrm{total}}^{\mathrm{SiPM}}$, $J_{\mathrm{total}}^{\mathrm{PMT}}$ and P_{CT}^{*} depend on the individual PDE measurement.

Variable	Mean	Stat. error	Syst. error
A_{SiPM}	$12.96\,\mathrm{mm}^2$	-	$0.73\,\mathrm{mm}^2$
A_{PMT}	$420.25\,\mathrm{mm}^2$	-	$4.11\,\mathrm{mm}^2$
SR	0.30	-	0.01
R	0.781	-	0.027
C_1	8.0 mV ns	0.3 mV ns	-
G_{c}	varying	4 % - 6 %	-
$J_{\mathrm{total}}^{\mathrm{SiPM}}$	varying	-	-
$J_{\mathrm{total}}^{\mathrm{PMT}}$	varying	-	-
P_{CT}^{*}	0.20 - 0.95	0.01 - 0.02	-

6.8 Conversion Efficiency of *Lumogen*® at VUV Wavelengths

Although there was no information about the absorption behavior at wavelengths of xenon scintillation light of *Lumogen*® available, the number of photons emitted by the *Lumogen*® N_{Lumo}^{*} can be calculated from $\mathrm{N}_{\mathrm{SiPM}}^{\gamma'}$. Together with the absolute number of photons $\mathrm{N}_{\mathrm{SiPM}}^{\gamma}$ that impinged onto the SiPM, the conversion efficiency $\varepsilon_{\mathrm{convert}}$ of *Lumogen*® at VUV wavelengths can be calculated via:

$$\varepsilon_{\mathrm{convert}} = \frac{N_{\mathrm{Lumo}}^{*}}{N_{\mathrm{SiPM}}^{\gamma}} \quad . \tag{6.25}$$

Fig. 6.13 shows the PDE spectrum of the used SiPM at $U_{\mathrm{over}} = 0.2 \cdot U_{\mathrm{break}}$ (red) and the relative intensity of the emission spectrum of *Lumogen*® (black). The wavelength is binned in steps of integer values of nm. These data sets were digitized from the spectral response of the PMT [51] and the relative emission spectrum of *Lumogen*® [42]. The relative intensity value $I_{\mathrm{Lumo}}(\lambda_i)$ of each wavelength λ_i of the *Lumogen*® spectrum can be related to the sum of all intensity values $\sum_j I_{\mathrm{Lumo}}(\lambda_j)$. This proportion yields the percentage amount of photons $S_{\mathrm{Lumo}}(\lambda_i)$

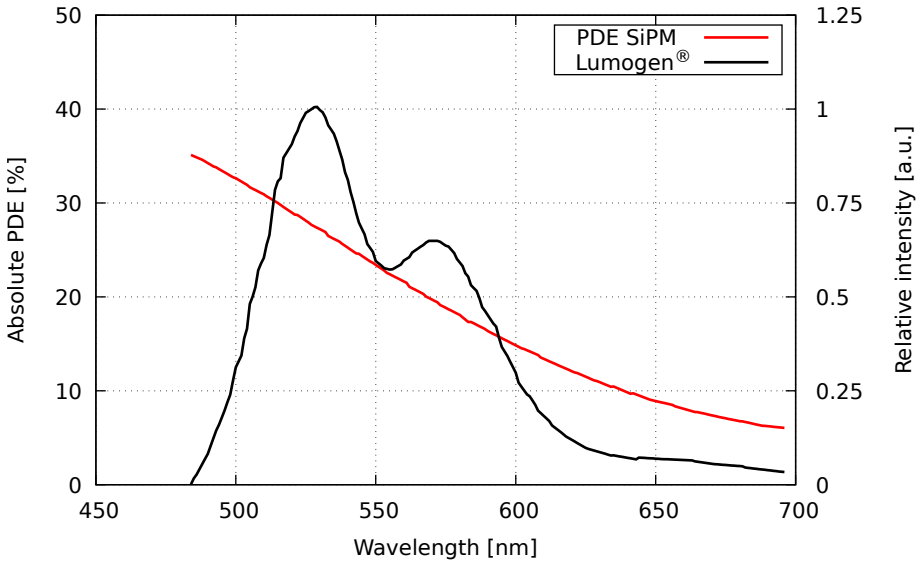

Figure 6.13: PDE of the used SiPM at $U_{\text{over}} = 0.2 \cdot U_{\text{break}}$ (red, left y-axis) in dependence on the wavelength. This data is extracted from [51]. Relative intensity of the emission spectrum of *Lumogen*® (black, right y-axis) in dependence on the wavelength. This data is obtained from [42]. A relative systematical error of 3 % results from the width of the data plot in the graphics the data is extracted from. Both data sets are binned to integer values of nm.

with one particular wavelength in the spectrum. $S_{\text{Lumo}}(\lambda_i)$ is calculated for every wavelength in the *Lumogen*® spectrum:

$$S_{\text{Lumo}}(\lambda_i) = \frac{I_{\text{Lumo}}(\lambda_i)}{\sum_j I_{\text{Lumo}}(\lambda_j)} \quad . \tag{6.26}$$

The PDE $\varepsilon_{\text{SiPM}}(\lambda_i)$ determines the number of measured photons impinging onto the SiPM with respect to their wavelength λ_i. The spectral response SR_{Lumo} of the SiPM to the spectrum emitted by the *Lumogen*® can be calculated via:

$$SR_{\text{Lumo}} = \sum_i \varepsilon_{\text{SiPM}}(\lambda_i) \cdot S_{\text{Lumo}}(\lambda_i) \quad . \tag{6.27}$$

The relation between the number of photons N^*_{Lumo} emitted by the *Lumogen*® and the number of photons $N^{\gamma'}_{\text{SiPM}}$ actually measured by the SiPM can therefore be calculated via:

$$N^{\gamma'}_{\text{SiPM}} = \frac{1}{2} \cdot N^*_{\text{Lumo}} \cdot SR_{\text{Lumo}} \quad . \tag{6.28}$$

The factor $\frac{1}{2}$ is necessary, since the direction of the light that is emitted by the *Lumogen*® is randomized and, therefore, distributed isotropically over all

solid angles. Therefore, it is assumed that only half of the photons are emitted towards the SiPM. The spectral response was calculated to be $SR_{\mathrm{Lumo}} = 0.229 \pm 0.007$. The overvoltage of the used SiPM at $-98\,^{\circ}\mathrm{C}$ and 20 % of the breakdown voltage is calculated via equ. 6.6 . $N^{\gamma'}_{\mathrm{SiPM}}$ is not determined for this particular overvoltage, but for 4.85 V and 5.35 V. To calculate $N^{\gamma'}_{\mathrm{SiPM}}(5.1\,\mathrm{V})$ the evolution of $N^{\gamma'}_{\mathrm{SiPM}}$ between 4.85 V and 5.35 V is assumed to be linear. This yields a measured photon number $N^{\gamma'}_{\mathrm{SiPM}}(5.1\,\mathrm{V})$. N^{*}_{Lumo} is calculated using equ. 6.28. The number of photons $N^{\gamma}_{\mathrm{SiPM}}(5.1\,\mathrm{V})$ impinging onto the SiPM is determined analogously to $N^{\gamma'}_{\mathrm{SiPM}}$ from $N^{\gamma}_{\mathrm{SiPM}}(4.85\,\mathrm{V})$ and $N^{\gamma}_{\mathrm{SiPM}}(5.35\,\mathrm{V})$. Using 6.25, the conversion efficiency for xenon scintillation light is calculated to be:

$$\varepsilon_{\mathrm{convert}} = 0.93 \pm 0.04^{\mathrm{stat}} \pm 0.13^{\mathrm{syst}} \quad . \tag{6.29}$$

7 Results and Discussion

The characteristic properties investigated in chap. 6 are discussed in this chapter. Exemplary comparisons to other devices are shown. Furthermore, limitations concerning the simulation with respect to parameters that were not taken into account and to variations of the photon fluence due to impurities in the xenon gas are outlined.

7.1 Results

As expected, the measured gain of the investigated SiPM follows a linear dependence. The breakdown voltage was extracted from the gain for different temperatures. U_{break} decreases linearly with the temperature. According to [48], the expected value of the breakdown voltage is $U_{\text{break}} = (25 \pm 3)\,\text{V}$ at a temperature of 20 °C. The measured values between −107.5 °C and 0.8 °C range from $U_{\text{break}}(-107.5\,^\circ\,\text{C}) = 25.4 \pm 0.2\,\text{V}$ to $U_{\text{break}}(0.8\,^\circ\,\text{C}) = 26.9 \pm 0.3\,\text{V}$. The breakdown voltage at 20 °C can be extrapolated from the measurements to be $U_{\text{break}}(20\,^\circ\text{C}) = (27.2 \pm 0.1)\,\text{V}$.

The extracted photon fluence on the PMT yields possible values for the reflection indices of copper and aluminum. There are some effects that affect the photon fluence and could not be taken into account (see sec. 7.2). These effects decrease the mean photon fluence and, therefore, the mean number of photons that impinge onto the PMT per α-particle. This affects the measured values for the reflectivity indices of coper and aluminum. It is expected that they tend to rise with a higher photon fluence on the PMT.

The calculated CT probability is compared to other devices that were investigated for the nEXO experiment. Tab. 7.1 shows P_{CT} for a FBK-2013 SiPM [35, 77] and a Hamamatsu-VIS SiPM [35]. The values for the KETEK and the FBK device are similar, whereas the Hamamatsu device exceeds the KETEK SiPM by almost a factor of 2. Additionally, the dependence of P_{CT} on the pixel area could be investigated within this thesis for one example. The limit for the percentage number of p.e. that are induced by correlated avalanches for the nEXO experiment is 20 %. The investigated SiPM was examined with respect to the CT induced

Table 7.1: CT probability of a FBK-2013 SiPM and Hamamatsu-VIS SiPM compared to the investigated KETEK PM3350. The data was taken from [35].

Device	U_{over} [V]	P_{CT}
FBK-2013	5.0	0.27
Hamamatsu-VIS	2.6	0.25
KETEK PM3350	5.0 / 2.6	0.26 / 0.14

number of p.e., excluding after-pulses. Even without correlated avalanches that originated from after-pulses, the SiPM exceeds the limit at an overvoltage of 3.3 V.

Fig. 7.1 shows the PDE of the investigated SiPM, the FBK-2013 SiPM mentioned above and a Hamamatsu SiPM that was developed in 2013 for the MEG experiment (further referred to as Hamamatsu-VUV) [35]. The red dots denote the PDE of the investigated SiPM, green dots the FBK-2013 SiPM and blue dots the Hamamatsu-VUV SiPM. The horizontal orange line indicates the required 15 % PDE limit for the nEXO experiment. In contrast to the other devices, the PDE of the investigated SiPM seems to be saturating at about 12.5 %. Fig. 7.2 shows the PDE of a KETEK PM3350 SiPM without *Lumogen*® coating in dependence on the relative overvoltage at a wavelength of 410 nm [48]. The vertical red lines indicate the voltage interval in which the measurements of this thesis were done. The *Lumogen*® shifts the xenon scintillation light in the green light regime with a maximum intensity of about 530 nm [58]. Assuming that the PDE shows a similar dependence on the overvoltage at 530 nm as it does at 410 nm, the saturation can be explained. However, none of the measured PDE values are above 15 %. There are effects on the PDE that could not be taken into account (see sec. 7.2). The PDE is increased by some of these effects and reduced by others. After-pulsing is not taken into account when the PDE is investigated. Therefore, it is expected that the actual value for the PDE is lower than the calculated one.

The conversion efficiency of *Lumogen*® at xenon scintillation light was estimated to be $\varepsilon_{\text{convert}} = 0.93 \pm 0.04^{\text{stat}} \pm 0.13^{\text{syst}}$. According to [58], the quantum yield is nearly 100 % in a wavelength interval from 100 nm to 450 nm. This seems realistic, since the quantum yield is defined as the ratio between the number of absorbed photons and the number of emitted photons. The conversion efficiency includes, unlike the quantum yield, the photons that are reflected on the surface of the *Lumogen*® layer. The conversion efficiency is, therefore, lower than the quantum yield.

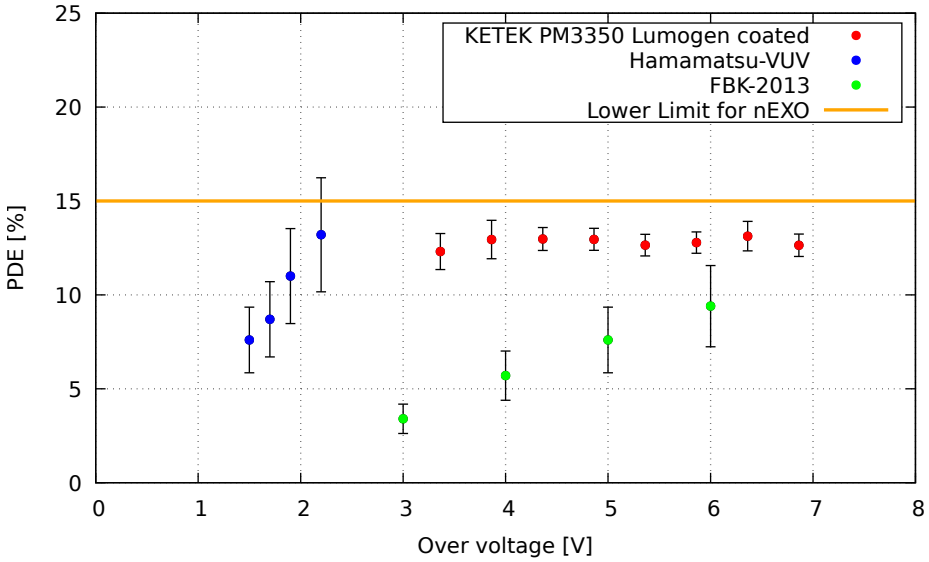

Figure 7.1: PDE in dependence on the overvoltage for different devices. Hamamatsu-VUV (green), FBK-2013 (blue) and the investigated *Lumogen*® coated KETEK PM3350 (red). The horizontal orange line indicates the required 15 % limit for the nEXO experiment. The data of the Hamamatsu and FBK device were taken from [35].

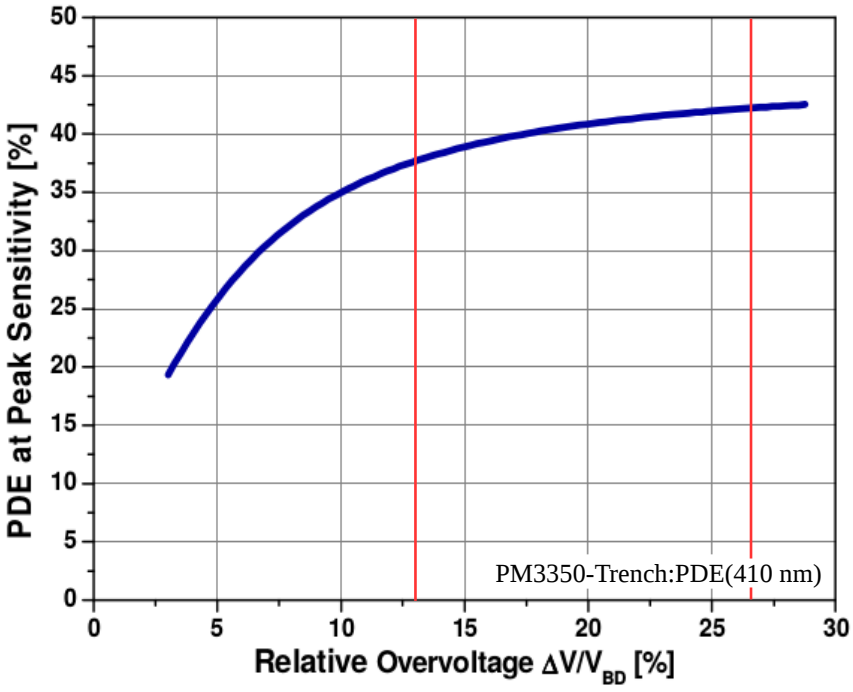

Figure 7.2: PDE in dependence on the relative overvoltage at a wavelength of 420 nm where the SiPM operates at maximum efficiency. This image was taken from [48].

7.2 Limitations

The reflection on neither the entrance window of the PMT nor the *Lumogen*® layer on the SiPM were taken into account in the simulation. These unattended parameters might have a significant effect on the predicted photon fluence on both detectors. A lower simulated fluence on the photocathode of the PMT would decrease the PDE, whereas a lower fluence on the SiPM is assumed to increase the PDE in return. Due to the asymmetric geometry of the setup and the fact that the scintillation light does not arise from a point source, the quantitative impact of reflection on the detectors cannot be approximated. Therefore, the simulation needs to be improved for future measurements so that reflection is taken into account.

Another limitation is that the xenon gas has already been in the xenon cell for several days before the PDE measurements were taken. Later measurements indicate that the xenon gas might have accumulated impurities from the surfaces in the xenon cell over time [78]. This impurification may lead to a higher absorption of the scintillation light, thus decreasing the measured photon fluence on the detectors. Due to the geometrical asymmetry in the setup, the detectors are not equally distant from the α-source. Therefore, the travel distance of the scintillation photons to the detectors is different. This may lead to a higher absorption towards the SiPM and was not taken into account in the simulation. Improvements on this effect can be achieved by cleaning and assembling the setup in a cleanroom to avoid later impurification of the xenon gas.

8 Summary and Prospects

One necessary objective in this thesis was to build and examine a cryogenic setup that is capable of controlling temperature and pressure of a gaseous xenon atmosphere. The temperature can be stabilized with a very simple control system and the temperature fluctuations in the xenon cell are negligible. The main objective, however, was the characterization of a *Lumogen*® coated SiPM in this setup at cryogenic temperatures with respect to the requirements for the nEXO experiment. The SiPM was successfully examined concerning its gain, temperature dependent breakdown voltage, crosstalk and PDE. In addition, the conversion efficiency of *Lumogen*® at xenon scintillation light was investigated. Furthermore, the results from the PDE measurements were used to investigate reflection properties of the xenon cell.

The setup and the analysis techniques were functional and proved to be suitable concerning the characterization of SiPMs at cryogenic temperatures. Yet, improvements regarding the practicability of certain aspects can still be done. For instance, the heating system can be upgraded with a PID-regulated control mechanism to avoid the temperature oscillation and, furthermore, the LN could be refilled automatically. Additionally, the *C++* based program used to analyze the data can be upgraded with a pulse finding algorithm, thus improving certain aspects of the analysis like identifying after-pulses.

Although some characteristics did not meet the required limits for the nEXO experiment, the detection of VUV light by converting it in the visible light regime is very effective. Yet, it is still to investigate whether a wavelength shifter is suitable for the nEXO experiment with respect to required radio purity and stability in liquid xenon. Regarding these uncertainties, collaborators are currently investigating SiPMs that are capable of detecting VUV photons without the application of a wavelength shifter.

A future objective concerning the characterization of SiPMs with respect to the requirements of the nEXO experiment is to extend the Erlangen setup towards the operation with liquid xenon. This improvement would allow the characterization of SiPMs for the nEXO experiment under more realistic circumstances. Further modifications regarding the recirculation of xenon will be done. In order to test modules of SiPMs arrays, which will be used in the nEXO experiment instead of single SiPMs, the xenon cell will be extended providing more space for electronics. Although the Erlangen work group has joined the nEXO collaboration only two years ago, several SiPM based techniques for the detection of VUV light were already tested in order to contribute to the nEXO experiment, which is one of the most promising candidates in the future search for the $0\nu\beta\beta$-decay.

A List of Abbreviations

APD Avalanche photodiode

CS Charge spectrum

CT Crosstalk

DAC Digital-to-analog converter

e-h Electron-hole

EC Electron capture

HFE Hydrofluoroether

IR Infra red

IV Inner vessel

LN Liquid nitrogen

OP Operational amplifier

OV Outer vessel

p.e. Photoelectron equivalent

PDE Photo detection efficiency

PHS Pulse heigth spectrum

PMT Photo multiplier tube

PTFE Polytetrafluoroethylene

QE Quantum efficiency

ROI Region of interest

SiPM Silicon photo multiplier

SM Standard model

TPC Time projection chamber

UV Ultra violet

VUV Vacuum ultra violet

B List of Figures

C List of Tables

D References

[1] https://www.nobelprize.org/nobel_prizes/physics/laureates/1903/, [accessed: 02.01.2017].

[2] http://www.neutrino.uni-hamburg.de/sites/site_neutrino/content/e45939/e48540/e48541/e48544/infoboxContent48545/material-vorlesung1-moessbauer pauli.pdf, [accessed: 02.01.2017].

[3] K. V. L. Samara. *"Nobel leptones". arXiv:hep-ph/9512420v1*, 25.12.1995.

[4] http://www.nobelprize.org/nobel_prizes/physics/laureates/2015/, [accessed: 01.06.2016].

[5] N. Schmitz. *"Neutrinophysik"*. Teubner, Stuttgart, 1997.

[6] K. A. Olive et. al. *"Review of particle physics". Chin. Phys. C, 38, 090001*, C38:090001, 2014.

[7] Zhi-zhong Xing Yifang Wang. *"Neutrino masses and flavor oscillations". arXiv:1504.06155v1 [hep-ph]*, 23.04.2015.

[8] Sergio Pastor Julien Lesgourgues. *"Neutrino mass from cosmology". arXiv: 1212.6154v1 [hep-ph]*, 26.12.2012.

[9] M. Mezzetto F. Monrabal J.J. Gómez-Cadenas, J. Martín-Albo and M. Sorel. *"The search for neutrinoless double beta decay". arXiv:1109.5515v2 [hep-ex]*, 01/16/2012.

[10] E. Andreotti et. al. *"Search for beta plus / EC double beta decay of* ^{120}*Te". arXiv:1011.4811v2 [nucl-ex]*, 11.01.2011.

[11] J. Martín-Albo J.J. Gómez-Cadenas. *"Phenomenology of neutrinoless double beta decay". arXiv:1502.00581v2 [hep-ex]*, 22.02.2014.

[12] Bogdan Povh et. al. *"Teilchen und Kerne"*. Springer-Lehrbuch Verlag, 2009.

[13] Luciano Maiani. *"Selected topics in majorana neutrino physics". arXiv:1406.5503v2 [hep-ph]*, 06.08.2014.

[14] H. Ejiri J.D Vergados and F. Simkovic. *"Theory of neutrinoless double beta decay". arXiv:1205.0649v2 [hep-ph]*, 05.06.2012.

[15] J.B. Albert et. al. *"Improved measurement of the $2\nu\beta\beta$ half-life of ^{136}Xe with the EXO-200 detector". 10.1103/PhysRevC.89.015502*, 2014.

[16] A. Gando et. al. *"Search for Majorana neutrinos near the inverted mass hierarchy region with KamLAND-Zen". arXiv:1605.02889v1 [hep-ex]*, 10.05.2016.

[17] B. Majorovits for the G ERDA collaboration. *"The search for $0\nu2\beta$ decay with the GERDA experiment status and prospects". arXiv:1506.00415v1 [hep-ex]*, 01.06.2015.

[18] R. Arnold. *"Search for neutrinoless double-beta decay of ^{100}Mo with the NEMO-3 detector". arXiv:1311.5695v3 [hep-ex]*, 20.06.2014.

[19] J.J. Gómez-Cadenas et. al. *"Sense and sensitivity of double beta decay experiments". JCAP06(2011)007*, 2011.

[20] Shinji Meadan. *"Predicted value of $0\nu\beta\beta$-decay effective Majorana mass with error of lightest neutrino mass". arXiv:1605.06871v1 [hep-ph]*, 23.05.2016.

[21] Stefano Dell'Oro et. al. *"Neutrinoless double beta decay: 2015 review". arXiv:1601.07512v2 [hep-ph]*, 19.04.2016.

[22] D. R. Austra et. al. *"Initial performance of the CUORE-0 experiment". arXiv:1402.0922v2 [physics.ins-det]*, 01.08.2014.

[23] Kai Zuber. *"Neutrinoless double beta decay". arXiv:1201.4665v1 [nucl-ex]*, 23.01.2012.

[24] J.B. Albert et. al. *"Search for $2\nu\beta\beta$ decay of ^{136}Xe to the 0_1^+ excited state of ^{136}Ba with EXO-200". arXiv: 1511.04770v1 [nucl-ex]*, 15.11.2015.

[25] K. Asakura et. al. *"Results from KamLAND-Zen". arXiv:1409.0077v1 [physics.ins-det]*, 30.08.2014.

[26] K.-H. Ackermann et. al. *"The GERDA experiment for the search of $0\nu\beta\beta$ decay in ^{76}Ge". arXiv:1212.4067v1 [physics.ins-det]*, 17.12.2012.

[27] W. Xu et. al. *"The Majorana demonstrator: A search for neutrinoless double-beta decay of ^{76}Ge". arXiv:1501.03089v2 [nucl-ex]*, 09.05.2015.

[28] S Umehara at. al. *"Search for neutrino-less double beta decay with CANDLES". Physics Procedia 61 (2015) 283 – 288 doi: 10.1016/j.phpro.2014.12.046*, 2014.

[29] Yung-Ruey Yen On behalf of the EXO-200 and nEXO collaboraBons. *"Neutrinoless double beta decay with EXO-200 and nEXO". Particle Physics and Cosmology Workshop 2015*, 30.06.2015.

[30] M. Auger et al. *"The EXO-200 detector, part i: Detector design and construction". arXiv:1202.2192v2 [physics.ins-det]*, 23.05.2012.

[31] N. Ackerman et. al. *"Observation of two-neutrino double-beta decay in ^{136}Xe with EXO-200". arXiv:1108.4193v2 [nucl-ex]*, 22.11.2011.

[32] J.B. Albert et. al. *"Search for Majorana neutrinos with the first two years of EXO-200 data". arXiv:1402.6956v2 [nucl-ex]*, 4.06.2014.

[33] Liang Yang. Talk on EXO-200 and nEXO. In *Neutrino conference 2016 - London*, 2016.

[34] Giorgo Gratta. Talk on the nEXO experiment. *nEXO Collaboration Meeting*, 09 - 11.07.2014.

[35] I. Ostrovskiy et. al. *"Characterization of silicon photomultipliers for nEXO". arXiv:1502.07837v2 [physics.ins-det]*, 06.07.2015.

[36] S. Sangiorgio. Poster: Informing nEXO R&R through simulations. In *Neutrino conference 2016 - London*, 2016.

[37] S. Kravitz *"Barium tagging in liquid xenon for nEXO"* APS Division Nuclear Physics Vancouver Meeting, 2016

[38] Dr. William R. Leo. *"Techniques for Nuclear and Particle Physics Experiments"*. Springer - Verlag, 1994.

[39] Hamamatsu Photonics Deutschland GmbH, Arzbergerstr. 10, D-82211 Herrsching am Ammersee, Germany, Telephone: (49)8152-375-0, Fax: (49)8152-2658 E-mail: info@hamamatsu.de. *"Hamamatsu Photomultiplier Tube R8520-406 Specifications"*.

[40] W. Demtröder. *"Experimentalphysik 3, Atome, Moleküle und Festkörper"*. Number ISBN 978-3-540-21473-9. Springer-Verlag Berlin Heidelberg, 3. auflage edition, 2010.

[41] N. Dinu. *"Instrumentation on silicon detectors: from properties characterization to applications"*. PhD thesis, Université Paris Sud - Paris XI, 2013. <tel-00872318>, 29.10.2013.

[42] BASF Germany Lumogen F Yellow 170, *"Technical Data sheet"*.

[43] http://www.ketek.net/ketek/ketek 33.jpg, [accessed: 01.12.2016].

[44] Fred Reinhard Uhlig. *"Charakterisierung und Anwendung von schnellen Photosensoren im Hinblick auf ihren Einsatz im PANDA-Experiment"*. PhD thesis, Firedrich-Alexander Universität Erlangen-Nürnberg, 2015.

[45] https://upload.wikimedia.org/wikipedia/commons/9/92/APD2_German.png, [accessed: 11.12.16].

[46] https://upload.wikimedia.org/wikipedia/commons/3/3a/APD3_German.png, [accessed: 11.12.16].

[47] H. Otono et. al. *"Study of the internal mechanisms of pixelized photon detectors operated in geiger-mode"*. *arXiv:0808.2541v1 [physics.ins-det]*, 19.08.2008.

[48] http://www.ketek.net/products/sipm/pm3350/, [accessed: 01.06.2015].

[49] http://www.ketek.net/, [accessed: 01.12.2016].

[50] Judith Schneider. *"Charakterisierung von Siliziumphotomultipliern"*, B.Sc. thesis, Firedrich-Alexander Universität Erlangen-Nürnberg, 10.2015.

[51] http://www.ketek.net/typo3temp/pics/a8ad0953d3.jpg, [accessed: 01.12.2016].

[52] F. Retière Y. Du. *"After-pulsing and cross-talk in multi-pixel photon counters"*. *Nuclear Instruments and Methods in Physics Research A 596 (2008) 396–401*, 2008.

[53] Joëlle Barral. *"Study of Silicon Photomultipliers"*. PhD thesis, Max Planck Institut für Physik 2, Werner-Heisenberg Institut, Münich, Germany, 2004.

[54] V. Álvarez et. al. *"Ionization and scintillation response of high-pressure xenon gas to alpha particles"*. *arXiv:1211.4508v3 [physics.ins-det]*, 21.03.2013.

[55] T. Doke E. Aprile. *"Liquid xenon detectors for particle physics and astrophysics"*. Reviews of modern physics, volume 82, DOI: 10.1103/RevModPhys.82.2053, 2010.

[56] J. Jortner et. al. *"Localized excitations in condensed Ne, Ar, Kr, and Xe"*. *The Journal of Chemical Physics 42, 4250 (1965); doi: 10.1063/1.1695927*, 1965.

[57] B.Sc. Lindsay Robert Wilson. *"Luminescent Solar Concentrators: A Study of Optical Properties, Re-absorption and Device Optimisation"*. PhD thesis, Department of Mechanical Engineering School of Engineering & Physical Sciences, Heriot-Watt University, Edinburgh EH14 4AS, United Kingdom, 05.2010.

[58] http://www.eureca.de/neu german/index.html, [accessed: 01.11.2016].

[59] https://www.edwardsvacuum.com, [accessed: 11.12.2016].

[60] https://www.pfeiffer vacuum.com/de/, [accessed: 11.12.2016].

[61] http://www.afriso.de/n2301160/i2452134.html, [accessed: 09.12.2016].

[62] https://www.vacom.de/, [accessed: 09.12.2016].

[63] http://www.elektroautomatik.de/de/unternehmen.html, [accessed: 09.12.2016].

[64] http://www.produktinfo.conrad.com/datenblaetter/500000-524999/510075-an-02-ml Power_Supply_PS_2403_Pro_de_en_fr.pdf, [accessed: 17.11.2016].

[65] http://cp.literature.agilent.com/litweb/pdf/E3631 90002.pdf, [accessed: 17.11.2016].

[66] http://iseg hv.com/de/products/detail/SHQ, [accessed: 09.12.2016].

[67] http://www.eltest.hu/pdf/WR6000A.pdf, [accessed: 09.12.2016].

[68] http://www.ni.com/download/labview-development-system 2014/4735/en/, [accessed: 14.112016].

[69] http://www.meilhaus.de/, [accessed: 11.09.2016].

[70] http://www.lakeshore.com/Pages/Home.aspx, [accessed: 11.12.2016].

[71] Christoph Berger. *"Elementarteilchenphysik"*. Springer-Verlag Berlin Heidelberg New York, 2006.

[72] Reimund Bayerlein. *"Simulation of alpha particle scintillation light in liquid and gaseous xenon with respect to surface reflections"*. Master's thesis, Friedrich - Alexander Universität Erlangen - Nürnberg, 2016.

[73] http://gnuplot.sourceforge.net/, [accessed: 14.11.2016].

[74] Personal consultation with Reymund Bayerlein

[75] www.hamamatsu.com/resources/pdf/etd/PMT_handbook_v3aE.pdf. "photomultiplier tubes - basics and applications", [accessed: 08.09.2016].

[76] http://www.testequity.com, [accessed: 13.12.2016].

[77] N. Serra et. al. *"Characterization of new FBK SiPM technology for visible light detection". JINST 8 P03019*, 2013.

[78] Tobias Ziegler. *"Characterisation of silicon photomultipliers with xenon scintillation light for the nEXO experiment"*. Master's thesis, Friedrich-Alexander Universität Erlangen-Nürnberg, 21.11.2016.

Acknowledgements

Many people supported me during my time working on this thesis. I would like to give a special thanks to the following persons without whom I would not have been able to finish my work:

Prof. Dr. Gisela Anton for the opportunity to do my Master's Thesis at the Erlangen Center for Astroparticle physics on one of the most interesting topics in the field of neutrino physics. Thank you for your always open door and constant support.

PD Dr. Thilo Michel for his excellent supervision and advise. I learned a lot from you, not only concerning physics. Your ability to solve problems of any kind helped me in many situations.

Jutta Dziwis without whom I would have gone crazy with all the paper work. Thank you for your support and your patience with me.

Henry Schott without whom modifying the setup would have taken a lot longer. Thank you for your help with all the technical details.

**Michael Wagenpfeil, Reimund Bayerlein, Judith Schneider,
Tobias Ziegler, Ako Jamil** for helping me putting this thesis on paper. And although it was a lot of work, building the setup with you guys was one of the most fun parts during my time working on this thesis.

The EXO-200/nEXO - work group Erlangen for being great colleagues and good friends. You made hard times bearable and I will always remember the fun and laughs we had together.

The EXO-200/nEXO collaboration for the enthusiasm to reach for new knowledge in particle physics. I am very happy to be part of this community.

The XENON - work group Münster for introducing us to their cryogenic setup. Thank your for all the input that we could use on our own setup.

KETEK for the Lumogen coated SiPM.

The Technician staff for supporting me with good advice and helping me with hardware problems.

Statutory Declaration

I, Patrick Hufschmidt, herewith declare that this Master's Thesis was written exclusively by myself. No other but the cited literature and resources have been used.

Erlangen, January 9, 2017 Patrick Hufschmidt